Title
Deciphering the mechanism of mitotic regulation and MAPK hyperactivation by RIT1 oncoproteins

Author
Cuevas Navarro, Antonio

Publication Date
2022

Peer reviewed|Thesis/dissertation

Deciphering the mechanism of mitotic regulation and MAPK hyperactivation by RIT1 oncoproteins

by
Antonio Cuevas Navarro

DISSERTATION
Submitted in partial satisfaction of the requirements for degree of
DOCTOR OF PHILOSOPHY

in

Biochemistry and Molecular Biology

in the

GRADUATE DIVISION
of the
UNIVERSITY OF CALIFORNIA, SAN FRANCISCO

Approved:

DocuSigned by:
David Toczyski
B39DA64A208E4CB...

David Toczyski
Chair

DocuSigned by:
Allan Balmain
[illegible]

Allan Balmain

DocuSigned by:
Natalia Jura
[illegible]

Natalia Jura

DocuSigned by:
Frank Mccormick
094D275D833840E...

Frank Mccormick

Committee Members

For my parents, Patricia and Ramiro

Acknowledgments

I would like to begin by thanking my thesis advisor, Dr. Frank McCormick, for all the guidance and support throughout my graduate school career. Thank you for cultivating a positive and collaborative learning environment and for sharing your endless wealth of knowledge. Your unending passion for science continues to be a major source of inspiration.

Thank you to all the great colleagues and friends at UCSF, and to current and former members of the McCormick lab, who were all a critical part of my growth as a scientist. I have learned so much from all of you and you've helped my graduate school career be such an enjoyable journey. A special thanks to Dr. Pau Castel, who motivated, guided, and challenged me throughout my Ph.D. work. I feel extremely fortunate to have you as a mentor.

To the members of my thesis committee, Dave Toczyski, Natalia Jura, and Allan Balmain, thank you for your guidance and scientific advice and for broadening my perspective and approach to my projects and science in general.

Lastly, I could not forget to mention the great support of family and friends who have been encouraging me every step of the way. Thank you.

Contributions

Chapter 2 is adapted from a manuscript published in *Current Biology* (**31**, 3915-3924.e9 (2021)), by the following authors: **Antonio Cuevas-Navarro**, Richard Van, Alice Cheng, Anatoly Urisman, Pau Castel, Frank McCormick.

A.C.-N., P.C. and F.M. conceived the project, supervised the research, and wrote the manuscript. A.C.-N. prepared the figures. A.C.-N. and R.V. performed the experiments. A.C. performed chromosome spread analysis. A.C. and A.U. performed MS sample preparation and analysis.

Chapter 3 is adapted from an unpublished manuscript by the following authors: **Antonio Cuevas-Navarro**, Morgan Wagner, Richard Van, Monalisa Swain, Madeline R. Allison, Alice Cheng, Simon Messing, Dhirendra K. Simanshu, Matthew J. Sale, Frank McCormick, Andrew G. Stephen, and Pau Castel.

A.C.-N., F.M, A.G.S, and P.C. conceived the project and supervised the research and wrote the manuscript. A.C.-N. prepared the figures. A.C.-N., M.W., R.V., A.C, S.M. and PC performed the experiments. M.W. conducted BRET, SPR, and ITC analyses. M.S. conducted NMR experiments. M.R.S. and M.J.S. generated the Rasless 293 cells.

Deciphering the mechanism of mitotic regulation and MAPK hyperactivation by RIT1 oncoproteins

Antonio Cuevas Navarro

Abstract

In response to extracellular stimuli, a diverse network of signaling pathways involved in cell growth, survival, and differentiation are activated and this process is prominently regulated by the Ras family of small guanosine triphosphatases (GTPases). Chapter 2 shows that RIT1, a Ras-related GTPase that regulates cell survival and stress response, can directly associate with core components of the spindle assembly checkpoint (SAC). The SAC functions as a sensor of unattached kinetochores that delays mitotic progression into anaphase until proper chromosome segregation is guaranteed. Disruptions to this safety mechanism lead to genomic instability and aneuploidy, which serve as the genetic cause of embryonic demise, congenital birth defects, intellectual disability, and cancer. However, despite the understanding of the fundamental mechanisms that control the SAC, it remains unknown how signaling pathways directly interact with and regulate the mitotic checkpoint activity. Through various biochemical and cell biological approaches, I demonstrate that RIT1 is essential for timely progression through mitosis and proper chromosome segregation. RIT1 dissociates from the plasma membrane (PM) during mitosis and interacts directly with SAC proteins MAD2 and p31^{comet} in a process that is regulated by cyclin-dependent kinase 1 (CDK1) activity. Furthermore, RIT1 oncoproteins silence the SAC and accelerate transit through mitosis by sequestering MAD2 from the mitotic checkpoint complex (MCC). Moreover, SAC suppression by pathogenic RIT1 promotes chromosome segregation errors and aneuploidy. These results highlight a unique function of RIT1 compared to other Ras GTPases and elucidate a direct link between a signaling pathway and the SAC through a novel regulatory mechanism.

RIT1 gain-of-function mutations are found in lung cancer, leukemia, and in the germline of Noonan syndrome individuals; these mutations promote RAF/MEK/ERK pathway activation, yet the mechanism by which RIT1 activates RAF remains poorly understood. Chapter 3 outlines a set of biophysical and biochemical approaches employed to characterize the association of RIT1 with plasma membrane lipids and its interaction with RAF kinases. We identify critical residues present in the RIT1 hypervariable region that facilitate interaction with negatively charged membrane lipids and show that these are necessary for association with RAF kinases. Furthermore, despite direct interaction with RAF kinases, RIT1 is unable to activate RAF/MEK/ERK signaling in the absence of classical Ras proteins. Lastly, consistent with RIT1-mediated RAF activation as a driver of disease, we show that MEK1/2 inhibition alleviates cardiac hypertrophy in a mouse model of RIT1-mutant Noonan syndrome.

Table of Contents

List of Figures

List of Tables

Chapter 1 : Introduction

RAS GTPases and the GTPase cycle

The Ras family of small guanosine triphosphatases (GTPases) control a diverse network of signaling pathways that are essential for human development and adult tissue homeostasis (*1*, *2*). The activity of Ras GTPases is dictated by their nucleotide-loading state and is subject to various regulatory mechanisms that respond to extracellular stimuli and feedback signals (*2*). Ras GTPases bound to guanosine diphosphate (GDP) are considered inactive, while their guanosine triphosphate (GTP)-bound conformation promotes the activation of downstream effector pathways. Activation of effector proteins is mediated by the formation of an effector-binding site created by two flexible loops (switch I and switch II) within the GTP-binding domain (G-domain) that contact the gamma-phosphate of GTP (*3*). GTPase activating proteins (GAPs), such as NF1 and RASA1/p120GAP, turn off Ras proteins by catalyzing GTP hydrolysis by several orders of magnitude compared to the intrinsic GTP hydrolysis rate (*4*, *5*). Conversely, guanine nucleotide exchange factors (GEFs), such as SOS1/2, promote the release of bound nucleotide (GDP or GTP), resulting in an exchange for GTP due to the ~10-fold greater concentration of GTP vs GDP in the cell (*2*). When bound to GTP, the founding members of the Ras family: HRAS, NRAS, KRAS4a, and KRAS4b (hereinafter referred to collectively as Ras) recruit RAF kinases and other effector proteins to the plasma membrane (PM) to activate various downstream signaling cascades. Indeed, translocation of RAF to the PM, mediated by its high-affinity Ras-binding domain (RBD), is a necessary step in the activation of the RAF/MEK/ERK mitogen-activated protein kinase (MAPK) pathway (*6*, *7*). Hyperactivation of this critical Ras signaling axis is a hallmark of many cancers and the cause of a group of developmental syndromes collectively called RASopathies(*8*).

RIT1, a Ras-related small GTPase

RIT1 is expressed in many tissues and, like other Ras GTPases, associates with the inner leaflet of the PM through a unique C-terminal hypervariable region (HVR). The G-domain of RIT1 shares 51% sequence identity with Ras and can potentially associate with an overlapping set of effector proteins, including the RAF kinases (**Figure 1.1**). However, regulation of the RIT1 GTPase cycle remains elusive, with cognate RIT1 GAPs and GEFs yet to be identified. Interestingly, a high fraction of cellular RIT1 is bound to GTP, even in the absence of mitogenic signals, suggesting that RIT1 activity may rely on its intrinsic nucleotide exchange and hydrolase activity and/or alternative regulatory mechanisms (*9*).

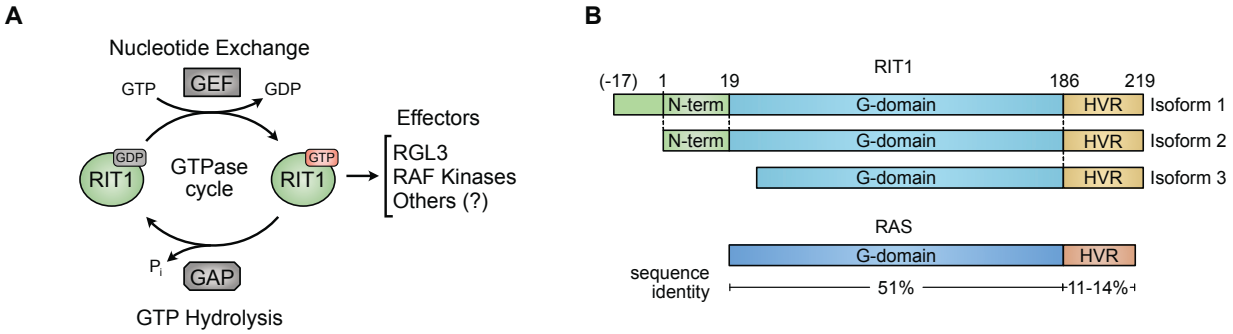

Figure 1.1: The RIT1 GTPase cycle and domain structure

(**A**) RIT1 cycles between an active GTP-bound state and an inactive GDP-bound state mediated by intrinsic nucleotide exchange and hydrolysis activity. The identity of GEF and GAP regulatory enzymes remains unknown. In the GTP-bound state, RIT1 can activate downstream effector proteins.
(**B**) RIT1 is composed of a central G-domain with high identity to the G-domain of Ras, and is flanked by an N-terminal region of unknown function and a C-terminal hypervariable region (HVR) that mediates PM association. *RIT1* gene gives rise to three different RIT1 isoforms.

Recently, gain-of-function mutations in the Ras-related GTPase RIT1 have emerged as drivers of human disease, including cancers of the lung and myeloid malignancies (*10*–*13*). Furthermore, germline *RIT1* variants cause Noonan syndrome (NS), a RASopathy characterized

by craniofacial dysmorphism, short stature, and congenital heart disease (*14*–*16*). RIT1 NS patients make up approximately 5-10% of all NS cases and exhibit congenital cardiac defects at elevated frequencies (*14*, *17*). Recent murine models of RIT1 NS present features that recapitulate clinical manifestations, including a shortened stature, craniofacial dysmorphism, and cardiac hypertrophy (*9*, *18*). Unlike activating mutations in Ras, which predominantly occur at codons 12, 13, or 61, pathogenetic RIT1 missense mutations are dispersed throughout the G-domain (**Figure 1.2**) but tend to cluster near or around switch II.

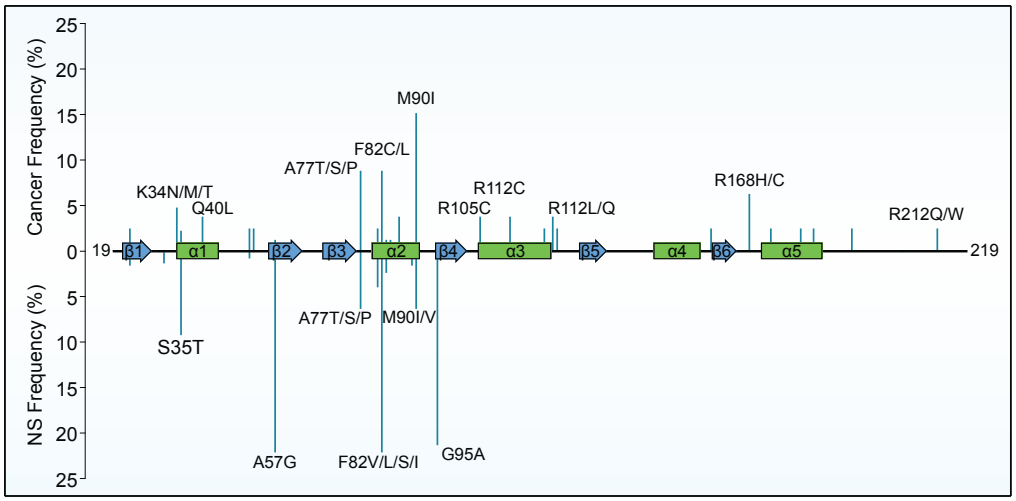

Figure 1.2: RIT1 mutations in cancer and NS
(**A**) Frequency of disease-associated RIT1 mutations identified in cancer (above) and NS (below). RIT1 single nucleotide variants represented here were obtained from the cBioPortal database for cancer (19, 20) (n = 79; only alleles found in more than one tumor) and the NSEuroNet database website, www.nseuronet.com for NS (n = 124).

Dysregulation of RIT1 degradation and associated pathogenicity

Despite the absence of proteins known to regulate the RIT1 GTPase cycle, we had previously identified an alternative regulatory mechanism of RIT1 activity involving the NS-associated protein LZTR1 (*9*). LZTR1 functions as a conserved substrate receptor for Cullin3 E3 ubiquitin ligase complexes ($CRL3^{LZTR1}$) to promote the ubiquitination and proteasomal degradation of GDP-bound RIT1 (*21*). NS pathogenic RIT1 and LZTR1 variants disrupt RIT1-

LZTR1 binding, resulting in the accumulation of RIT1 protein (*9*) and enhanced MAPK signaling; however, it remains unclear how increased RIT1 protein abundance contributes to MAPK pathway activation. We posit that the accumulation of RIT1 protein at the PM can drive mild MAPK activation, like other weakly-activating NS alleles, via the recruitment of RAF kinases to the PM, a requisite for MAPK pathway activation (*6*, *7*). Chapter 3, below, explores this hypothesis and outlines a biochemical analysis of the RIT1-RAF interaction, the intriguing dependency of RIT1-mediated MAPK activation on Ras proteins, and an evaluation of pharmacological MAPK inhibition in a pre-clinical mouse model of RIT1 NS.

Mitotic regulation by RIT1

Through an unbiased affinity purification mass spectrometry (AP-MS) screen in mammalian cells, we identified two novel RIT1-binding partners: MAD2 (also known as MAD2L1) and p31^{comet} (also known as MAD2L1 binding protein, MAD2L1BP). MAD2 and p31^{comet} are key components of the spindle assembly checkpoint (SAC), a safety mechanism that halts mitotic progression in prometaphase until all chromosomes are correctly attached to microtubule fibers at their kinetochores and are properly aligned at the metaphase plate (*22*). MAD2 plays a critical role in SAC signal amplification through its association with MAD1 at unattached kinetochores, a process that catalyzes the formation of the mitotic checkpoint complex (MCC) comprising CDC20-bound MAD2, BurbR1, and Bub3 (*23*, *24*, *24*). p31^{comet} inhibits the formation of MCC and promotes its disassembly through direct association with MAD2 (*25*–*27*). The physical interaction with components of the SAC, led us to hypothesize that RIT1 may regulate the activity of MAD2 and p31^{comet}, and in turn, modulate SAC signal transduction. Chapter 2, below, outlines an investigation of RIT1-mediated regulation of the SAC and its implications in the pathogenesis of RIT1-mediated tumor formation, previously published in Cuevas-Navarro *et al*., (2021) (*28*). Notably, SAC regulation by RIT1 appeared to be decoupled from MAPK pathway activation, suggesting the evolution of an independent function for a Ras family GTPase. During our

investigation, another group independently identified a link between the expression of RIT1 oncoproteins and SAC dysregulation via a multi-omic approach (*29*).

References

1. P. Castel, K. A. Rauen, F. McCormick, The duality of human oncoproteins: drivers of cancer and congenital disorders. *Nat Rev Cancer*. **20**, 383–397 (2020).

2. D. K. Simanshu, D. V. Nissley, F. McCormick, RAS Proteins and Their Regulators in Human Disease. *Cell*. **170**, 17–33 (2017).

3. I. R. Vetter, A. Wittinghofer, The guanine nucleotide-binding switch in three dimensions. *Science*. **294**, 1299–1304 (2001).

4. J. Cherfils, M. Zeghouf, Regulation of small GTPases by GEFs, GAPs, and GDIs. *Physiol Rev*. **93**, 269–309 (2013).

5. J. C. Hunter, A. Manandhar, M. A. Carrasco, D. Gurbani, S. Gondi, K. D. Westover, Biochemical and Structural Analysis of Common Cancer-Associated KRAS Mutations. *Mol Cancer Res*. **13**, 1325–1335 (2015).

6. S. J. Leevers, H. F. Paterson, C. J. Marshall, Requirement for Ras in Raf activation is overcome by targeting Raf to the plasma membrane. *Nature*. **369**, 411–414 (1994).

7. D. Stokoe, S. G. Macdonald, K. Cadwallader, M. Symons, J. F. Hancock, Activation of Raf as a result of recruitment to the plasma membrane. *Science*. **264**, 1463–1467 (1994).

8. K. A. Rauen, The RASopathies. *Annu Rev Genomics Hum Genet*. **14**, 355–369 (2013).

9. P. Castel, A. Cheng, A. Cuevas-Navarro, D. B. Everman, A. G. Papageorge, D. K. Simanshu, A. Tankka, J. Galeas, A. Urisman, F. McCormick, RIT1 oncoproteins escape LZTR1-mediated proteolysis. *Science*. **363**, 1226–1230 (2019).

10. A. H. Berger, M. Imielinski, F. Duke, J. Wala, N. Kaplan, G.-X. Shi, D. A. Andres, M. Meyerson, Oncogenic RIT1 mutations in lung adenocarcinoma. *Oncogene*. **33**, 4418–4423 (2014).

11. I. Gómez-Seguí, H. Makishima, A. Jerez, K. Yoshida, B. Przychodzen, S. Miyano, Y. Shiraishi, H. D. Husseinzadeh, K. Guinta, M. Clemente, N. Hosono, M. A. McDevitt, A. R. Moliterno, M. A. Sekeres, S. Ogawa, J. P. Maciejewski, Novel recurrent mutations in the RAS-like GTP-binding gene RIT1 in myeloid malignancies. *Leukemia*. **27**, 1943–1946 (2013).

12. R. Van, A. Cuevas-Navarro, P. Castel, F. McCormick, The molecular functions of RIT1 and its contribution to human disease. *Biochem J*. **477**, 2755–2770 (2020).

13. S. Chen, R. S. Vedula, A. Cuevas-Navarro, B. Lu, S. J. Hogg, E. Wang, S. Benbarche, K. Knorr, W. J. Kim, R. F. Stanley, H. Cho, C. Erickson, M. Singer, D. Cui, S. Tittley, B. H. Durham, T. S. Pavletich, E. Fiala, M. F. Walsh, D. Inoue, S. Monette, J. Taylor, N. Rosen, F. McCormick, R. C. Lindsley, P. Castel, O. Abdel-Wahab, *Cancer Discov*, in press, doi:10.1158/2159-8290.CD-21-1631.

14. M. Yaoita, T. Niihori, S. Mizuno, N. Okamoto, S. Hayashi, A. Watanabe, M. Yokozawa, H. Suzumura, A. Nakahara, Y. Nakano, T. Hokosaki, A. Ohmori, H. Sawada, O. Migita, A. Mima, P. Lapunzina, F. Santos-Simarro, S. García-Miñaúr, T. Ogata, H. Kawame, K. Kurosawa, H. Ohashi, S.-I. Inoue, Y. Matsubara, S. Kure, Y. Aoki, Spectrum of mutations and genotype-phenotype analysis in Noonan syndrome patients with RIT1 mutations. *Hum Genet*. **135**, 209–222 (2016).

15. Y. Aoki, T. Niihori, T. Banjo, N. Okamoto, S. Mizuno, K. Kurosawa, T. Ogata, F. Takada, M. Yano, T. Ando, T. Hoshika, C. Barnett, H. Ohashi, H. Kawame, T. Hasegawa, T.

Okutani, T. Nagashima, S. Hasegawa, R. Funayama, T. Nagashima, K. Nakayama, S.-I. Inoue, Y. Watanabe, T. Ogura, Y. Matsubara, Gain-of-function mutations in RIT1 cause Noonan syndrome, a RAS/MAPK pathway syndrome. *Am J Hum Genet*. **93**, 173–180 (2013).

16. M. Koenighofer, C. Y. Hung, J. L. McCauley, J. Dallman, E. J. Back, I. Mihalek, K. W. Gripp, K. Sol-Church, P. Rusconi, Z. Zhang, G.-X. Shi, D. A. Andres, O. A. Bodamer, Mutations in RIT1 cause Noonan syndrome - additional functional evidence and expanding the clinical phenotype. *Clin Genet*. **89**, 359–366 (2016).

17. A. E. Roberts, J. E. Allanson, M. Tartaglia, B. D. Gelb, Noonan syndrome. *Lancet*. **381**, 333–342 (2013).

18. S. Takahara, S.-I. Inoue, S. Miyagawa-Tomita, K. Matsuura, Y. Nakashima, T. Niihori, Y. Matsubara, Y. Saiki, Y. Aoki, New Noonan syndrome model mice with RIT1 mutation exhibit cardiac hypertrophy and susceptibility to β-adrenergic stimulation-induced cardiac fibrosis. *EBioMedicine*. **42**, 43–53 (2019).

19. J. Gao, B. A. Aksoy, U. Dogrusoz, G. Dresdner, B. Gross, S. O. Sumer, Y. Sun, A. Jacobsen, R. Sinha, E. Larsson, E. Cerami, C. Sander, N. Schultz, Integrative analysis of complex cancer genomics and clinical profiles using the cBioPortal. *Sci Signal*. **6**, pl1 (2013).

20. E. Cerami, J. Gao, U. Dogrusoz, B. E. Gross, S. O. Sumer, B. A. Aksoy, A. Jacobsen, C. J. Byrne, M. L. Heuer, E. Larsson, Y. Antipin, B. Reva, A. P. Goldberg, C. Sander, N. Schultz, The cBio Cancer Genomics Portal: An Open Platform for Exploring Multidimensional Cancer Genomics Data. *Cancer Discovery*. **2**, 401–404 (2012).

21. A. Cuevas-Navarro, L. Rodriguez-Muñoz, J. Grego-Bessa, A. Cheng, K. A. Rauen, A. Urisman, F. McCormick, G. Jimenez, P. Castel, Cross-species analysis of LZTR1 loss-of-function mutants demonstrates dependency to RIT1 orthologs. *Elife*. **11**, e76495 (2022).

22. A. Musacchio, The Molecular Biology of Spindle Assembly Checkpoint Signaling Dynamics. *Curr Biol*. **25**, R1002-1018 (2015).

23. A. De Antoni, C. G. Pearson, D. Cimini, J. C. Canman, V. Sala, L. Nezi, M. Mapelli, L. Sironi, M. Faretta, E. D. Salmon, A. Musacchio, The Mad1/Mad2 complex as a template for Mad2 activation in the spindle assembly checkpoint. *Curr Biol*. **15**, 214–225 (2005).

24. X. Luo, G. Fang, M. Coldiron, Y. Lin, H. Yu, M. W. Kirschner, G. Wagner, Structure of the Mad2 spindle assembly checkpoint protein and its interaction with Cdc20. *Nat Struct Biol*. **7**, 224–229 (2000).

25. R. S. Hagan, M. S. Manak, H. K. Buch, M. G. Meier, P. Meraldi, J. V. Shah, P. K. Sorger, p31(comet) acts to ensure timely spindle checkpoint silencing subsequent to kinetochore attachment. *Mol Biol Cell*. **22**, 4236–4246 (2011).

26. M. Yang, B. Li, D. R. Tomchick, M. Machius, J. Rizo, H. Yu, X. Luo, p31comet blocks Mad2 activation through structural mimicry. *Cell*. **131**, 744–755 (2007).

27. F. G. Westhorpe, A. Tighe, P. Lara-Gonzalez, S. S. Taylor, p31comet-mediated extraction of Mad2 from the MCC promotes efficient mitotic exit. *J Cell Sci*. **124**, 3905–3916 (2011).

28. A. Cuevas-Navarro, R. Van, A. Cheng, A. Urisman, P. Castel, F. McCormick, The RAS GTPase RIT1 compromises mitotic fidelity through spindle assembly checkpoint suppression. *Curr Biol*. **31**, 3915-3924.e9 (2021).

29. A. Vichas, A. K. Riley, N. T. Nkinsi, S. Kamlapurkar, P. C. R. Parrish, A. Lo, F. Duke, J. Chen, I. Fung, J. Watson, M. Rees, A. M. Gabel, J. D. Thomas, R. K. Bradley, J. K. Lee, E. M. Hatch, M. K. Baine, N. Rekhtman, M. Ladanyi, F. Piccioni, A. H. Berger, Integrative oncogene-dependency mapping identifies RIT1 vulnerabilities and synergies in lung cancer. *Nat Commun*. **12**, 4789 (2021).

Chapter 2 : The RAS GTPase RIT1 compromises mitotic fidelity through spindle assembly checkpoint suppression

RIT1 mutations have been identified as oncogenic drivers of lung adenocarcinoma and etiologic factors of Noonan syndrome (*1*–*3*). RIT1 has a unique set of effector proteins but shares activation of the MAPK pathway with other Ras GTPases (*4*–*6*). However, due to the lack of identified cognate GTPase activating protein or exchange factors, regulation of the RIT1 GTPase cycle remains unclear (*5*). Nonetheless, RIT1 abundance and activity is regulated at the protein level through proteasomal degradation, a mechanism mediated by the adaptor protein LZTR1 and the E3 ubiquitin ligase Cullin 3 ($CRL3^{LZTR1}$) (*7*). While the role of RIT1 in Noonan syndrome is likely mediated by hyperactivation of the MAPK pathway, a characteristic feature of the disorder, its role in normal cells and in malignancies is less clear.

To characterize the RIT1 interactome, we performed an affinity purification-mass spectrometry screen (**Figure 2.1A**) that identified MAD2 (MAD2L1) and $p31^{comet}$ (also known as MAD2L1-binding protein) as novel and selective RIT1 binding partners that do not interact with other Ras GTPases (**Figures 2.5A and 2.5B**). MAD2 participates in SAC signal amplification at unattached kinetochores which catalyze the formation of the MCC, comprised of MAD2, CDC20, BubR1, and Bub3 (*8*). In contrast, $p31^{comet}$ binds MAD2 and silences MCC catalysis at unattached kinetochores and promotes the removal of MAD2 from the MCC (*9*–*13*). MAD2 and $p31^{comet}$ dimerization prompted us to assess whether RIT1 interacts with MAD2 and $p31^{comet}$ directly (*14*). Pulldown analysis revealed both interactions to be direct and independent on MAD2 and $p31^{comet}$ dimerization (**Figure 2.1B**). Furthermore, the RIT1-MAD2 interaction is conserved in zebrafish and Drosophila (**Figure 2.1C**). To determine whether RIT1 binding to MAD2 or $p31^{comet}$ is regulated by its GTPase cycle, we assessed binding to RIT1 loaded with GDP or GTPγS, a non-hydrolyzable GTP analog. This revealed that both interactions are independent of the guanosine nucleotide-loaded state of RIT1 (**Figure 2.1D**). Consistently, binding to MAD2 and $p31^{comet}$ is not

influenced by disease-associated RIT1 mutations (**Figure 2.5C**). These results suggest that the binding interface lies outside of RIT1's switch I and II domains which are sensitive to GDP/GTP binding, and, hence, MAD2 and p31^{comet} are not typical RIT1 effector proteins.

MAD2 and p31^{comet}'s structural similarity highlighted potential binding competition for RIT1 (*15*, *16*). Thus, we used a competition binding assay in which titration of MAD2 WT or RQ, a dimerization and p31-binding deficient mutant, failed to suppress RIT1-p31^{comet} binding (**Figure 2.1E**) (*17*). These data support a non-competitive binding model. Notably, titration of MAD2 exerts a cooperativity effect on RIT1-p31^{comet} binding that relies on MAD2 and p31^{comet} dimerization. Binding cooperativity was further observed by gel filtration in which incubation of RIT1, MAD2, and p31^{comet} produced a high molecular-weight peak containing all three proteins, suggesting that they assemble into a multimeric complex *in vitro* (**Figures 2.5D-2.5I**).

Due to the similarity between the RIT1 G-domain and that of other Ras GTPases, particularly its paralog RIT2, we hypothesized that RIT1's N-terminal or C-terminal extensions may mediate interaction with MAD2 and p31^{comet} (**Figure 2.1F**) (*18*). We analyzed RIT1 N- or C-terminal deletion mutants and demonstrated that the C-terminal domain is necessary and sufficient for MAD2 and p31^{comet} binding (**Figures 2.1G,H, and 2.5J**). Consecutive C-terminal truncations allowed us to identify residues 209-211 (SPF) as critical for MAD2 and p31^{comet} binding (**Figures 2.5K and 2.5L**) and, when mutated to corresponding RIT2 residues 207-209 (GSL), the interaction was significantly reduced (**Figure 2.1I**).

During interphase, RIT1's C-terminal tail mediates PM association (*19*). However, when analyzing mitotic cells, we observed a diffuse cytoplasmic distribution of RIT1 as cells enter mitosis and as they progress through metaphase that is followed by rapid translocation to the PM during anaphase (**Figures 2.2A and 2.2B**). Consistently, a predominantly cytoplasmic distribution of endogenous RIT1 was detected in mitotic cell lysates (**Figure 2.2C**). In contrast, RIT1^{GSL} was not displaced from the PM (**Figures 2.6A and 2.6B**). These data indicate that diffusion of RIT1 between the PM and cytoplasm occurs during mitosis and may be influenced by its association

with MAD2 and/or p31^{comet}. Thus, we assessed the binding of RIT1 to phospholipid-containing liposomes and noted that pre-incubation of RIT1 with MAD2, but not p31^{comet}, inhibited binding to phospholipid membranes (**Figure 2.6C**), suggesting mutual exclusivity between PM association and MAD2 binding.

Because our mass spectrometry revealed RIT1 C-terminal domain phosphorylation at S209 (**Figure 2.6D**), we hypothesized that a dynamic regulatory mechanism may control the interaction between RIT1 and MAD2 or p31^{comet}. Indeed, phospho-mimetic (S209D/E), but not phospho-deficient (S209A), mutations disrupted RIT1-MAD2/p31^{comet} binding (**Figure 2.2D**). Additionally, an antibody that detects RIT1 S209 phosphorylation (**Figure 2.6E**), showed that RIT1 phosphorylation is most abundant during mitosis (**Figure 2.2E**). To identify the kinase mediating phosphorylation of RIT1, we tested a panel of inhibitors against proline-directed serine/threonine kinases (**Figure 2.6C**) (*20*). Inhibition of CDK activity in prometaphase-arrested cells led to a reduction of RIT1 S209 phosphorylation. Furthermore, in a cell-free assay using mitotic cell extracts, CDK1 inhibition significantly reduced phosphorylation of recombinant RIT1 (**Figure 2.2F**). To determine whether RIT1 is a direct substrate of CDK1/CyclinB1, we performed *in vitro* kinase assays using recombinant proteins. RIT1 S209 phosphorylation by CDK1/CyclinB1 was detected by immunoblotting and confirmed by mass spectrometry (**Figures 2.2G and 2.2H).** These findings suggest CyclinB1/CDK1 phosphorylates RIT1 during mitosis, which coincides with the cell cycle pattern of CyclinB1 expression and CDK1 activity (*21*). We propose that CDK1 regulates the association of RIT1 with MAD2 and p31^{comet} in a cell cycle-dependent manner. Since RIT1 S209 phosphorylation may also regulate its association with the PM, we evaluated the effect of S209A and S209D mutations on the subcellular distribution of RIT1; these had no noticeable effect on RIT1 during interphase (**Figure 2.6G**). However, in mitotic cells, RIT1^{S209A} remained at the PM throughout mitosis, while RIT1^{S209D} exhibited a diffuse cytoplasmic distribution but, unlike WT, failed to translocate to the PM during anaphase (**Figures 2.2A, 2.2B, and Figures 2.6H, 2.6I**). Notably, the constitutive PM association of RIT1^{S209A} suggests that MAD2-binding capacity

is not sufficient to extract RIT1 from the PM (**Figure 2.6C**). Together, these data suggest that CDK1 modulates both the subcellular distribution of RIT1 during mitosis and its association with MAD2/p31^{comet} (**Figure 2.6J**).

MAD2 and p31^{comet} regulate the duration of the SAC and, in turn, the duration of mitosis. This prompted us to examine whether RIT1, through its direct association with MAD2 and p31^{comet}, can influence the SAC. Depletion of RIT1 by RNAi or by CRISPR-mediated knockout resulted in prolonged mitotic progression (**Figures 2.3A, 2.7A-2.7E).** Moreover, pharmacological inhibition of the SAC rescued the effect of RIT1 depletion, indicating that RIT1 affects mitosis in a SAC-dependent manner (*22*). Furthermore, loss of RIT1 increased the rate of chromosome segregation errors (**Figure 2.3B**), suggesting that RIT1 is not only essential for timely progression through mitosis, but that dysregulation of RIT1 protein levels disrupt proper SAC function.

To further assess the effect of RIT1 on the SAC, we knocked out LZTR1 or expressed RIT1^{M90I}, a pathogenic variant that is insensitive to CRL3^{LZTR1}-mediated protein degradation, resulting in increased RIT1 expression levels (**Figures 2.7F and 2.7G**) (*7*). Loss of LZTR1 or RIT1^{M90I} expression accelerated the rate of mitotic progression in asynchronously growing cells, an effect that relied on the release of RIT1 from the PM (**Figures 2.3C, 2.7H, 2.7I).** Similarly, overexpression of RIT1 WT or M90I partially overrode the pharmacologically-induced SAC response (**Figures 2.3D and 2.7J**). Importantly, abolishing MAD2 and p31^{comet} binding using RIT1 phospho-mimetic mutants rescued suppression of the SAC mediated by RIT1^{M90I} (**Figures 2.7K and 2.7L**). Of note, the M90I/S209A mutant retained the ability to suppress the SAC despite being insensitive to CDK1/Cyclin B-mediated regulation, suggesting that at pathogenic expression levels, sufficient RIT1 molecules reside in the cytoplasm to interact with MAD2 and p31^{comet}. We did not observe a discernible difference in basal MAPK activation between these mutants, ruling out the possibility that the rescue effect exhibited by these mutants was due to altered MAPK signaling (**Figure 2.7N**). To evaluate the role of RIT1's GTPase activity on SAC suppression, we generated an inactive, GDP-bound mutant (M90I/S35N) that retained the ability to accelerate the

rate of mitotic progression (**Figures 2.3E and 2.3F**). These data suggest that the G-domain, which is dispensable for MAD2/p31^{comet} binding, may not play a direct role in SAC silencing. To further evaluate this hypothesis, we generated a chimeric EGFP-RIT1 C-terminal tail fusion protein whose overexpression was sufficient to suppress the SAC (**Figure 2.7N**).

A weakened SAC may allow precocious anaphase entry that results in chromosome instability and missegregation (*23*–*27*). Therefore, we examined whether RIT1-mediated suppression of the SAC promotes chromosome segregation errors in HCT-116, a cancer cell line with a near diploid karyotype that exhibits low chromosomal instability (*28*). Ectopic expression of RIT1^{M90I} significantly increased the rate of mitotic errors, including lagging and bridging chromosomes, in a MAD2- and p31^{comet}-binding dependent manner (**Figures 2.3G and 2.7O).** Consequently, we observed an increased rate of aneuploidy in cells expressing RIT1^{M90I}, but not in cells expressing the mutant that is unable to bind MAD2/p31^{comet} (**Figures 2.3H and 2.7P)**. These results demonstrate that increased levels of RIT1 lead to compromised mitotic fidelity as a result of direct interaction with MAD2 and p31^{comet}.

SAC signaling is tightly regulated and amplified by the catalyzed conversion of MAD2 from its open (O-MAD2) to its closed conformational state (C-MAD2) upon binding MAD1 at unattached kinetochores (*15*, *29*, *30*). The conformational change in MAD2 primes its association with CDC20 (*31*, *32*). To directly test whether RIT1 inhibits the association of MAD2 with CDC20 or MAD1, we performed competitive pulldown assays to test mutual exclusivity between RIT1-MAD2 and MAD2-CDC20/MAD1 binding (**Figures 2.4A and 2.4B**). MAD2 binding peptide 1 (MBP1), a high-affinity synthetic peptide that mimics the MAD2 interaction motifs (MIM) of CDC20 and MAD1, abolished MAD2-RIT1 binding (*32*). Conversely, titration of full-length RIT1 reduced the binding of MAD2 to CDC20 MIM beads (*33*), suggesting that RIT1 competes with CDC20 and MAD1 for MAD2 binding. However, since binding to MBP1 or CDC20$^{111\text{-}138}$ drives the conversion of O-MAD2 to C-MAD2, an alternative explanation may be that RIT1 preferentially binds to O-MAD2 (*32*). To distinguish between these two models, we assessed the binding of RIT1 with O- or C-state

stabilized MAD2 mutants (**Figure 2.4C**) (*15*). C-MAD2 mutants retained their interaction with RIT1, whereas O-MAD2 mutants failed to bind RIT1, except $MAD2^{LL}$ which can adopt a closed conformation state in the presence of MIM ligand (*31*). Furthermore, the expression of a MAD2 phospho-mimetic mutant in cells that adopts the O-MAD2 conformer fails to bind RIT1 (**Figure 2.8A**) (*34*). These results demonstrate that RIT1 exhibits preferential binding to C-MAD2 over O-MAD2, potentially stabilizing the closed conformer; moreover, RIT1 directly competes with CDC20 and MAD1 for MAD2 binding *in vitro*. We posit that RIT1 and CDC20/MAD1 may compete for the same interface on MAD2, which would predict that RIT1 binding promotes the conversion of O-MAD2 to C-MAD2 (*32*, *35*). To test this hypothesis, we incubated MAD2 protein with excess RIT1 C-terminal tail peptide and separated by gel filtration (**Figure 2.4D**). In the presence of excess RIT1 peptide, MAD2 protein fails to dimerize, similar to previous reports in which excess CDC20 peptide disrupted O-MAD2:C-MAD2 dimers by saturating all molecules into their closed conformational state (*29*, *36*). In contrast, incubation with RIT1 S209 phosphorylated peptide did not disrupt the formation of MAD2 dimers (**Figure 2.2D**). RIT1 preferential binding to C-MAD2 and dimerization of $p31^{comet}$ with C-MAD2 suggests that their oligomerization produces a RIT1-C-MAD2-$p31^{comet}$ complex and, hence, would explain the increased RIT1-$p31^{comet}$ affinity observed in the presence of MAD2 (**Figure 2.1E**).

Our biochemical analyses support a model of RIT1-mediated SAC inhibition that involves the sequestration of MAD2 away from MAD1 and/or CDC20 complexes. To test this model in a cellular context, we first analyzed MAD2 recruitment to unattached kinetochores and observed no measurable differences under RIT1 depletion or ectopic $RIT1^{M90I}$ expression (**Figures 2.8B-2.8E)**, suggesting that RIT1 may regulate the SAC downstream of kinetochores. Thus, we examined MAD2-CDC20 binding in cells by interrogating MCC integrity under nocodazole washout. RIT1 depletion did not affect MCC disassembly (**Figures 2.8F and 2.8G)**, potentially due to compensatory $p31^{comet}$ silencing (*13*, *37*). However, $RIT1^{M90I}$ significantly reduced MAD2-CDC20 and BubR1-CDC20 interactions (**Figures 4E and 4F**). These data suggest that pathogenic RIT1

protein levels hinder MCC integrity and are in line with the model that RIT1 sequesters MAD2 from CDC20 and promotes MCC disassembly.

To investigate the effect of RIT1 on MAD2 and CDC20 binding in the presence of p31^{comet}, we conducted competitive pulldown assays. Consistent with the cooperativity effect exhibited by the RIT1-MAD2-p31^{comet} complex, the addition of p31^{comet} enhanced RIT1-mediated inhibition of MAD2-CDC20 binding (**Figures 2.8H and 2.8I**). Furthermore, RIT1 and p31^{comet} cooperation was dependent on MAD2-p31^{comet} dimerization. These results suggest that RIT1 may cooperate with p31^{comet} to extract MAD2 from the MCC and promote its disassembly.

Regulation of mitotic progression by the SAC is achieved through inhibition of the anaphase-promoting complex/cyclosome (APC/C) by the MCC (*38*). We reasoned that RIT1 inhibition of MAD2-CDC20 association may promote APC/C activity. Therefore, we measured *in vitro* ubiquitination and degradation of APC/C substrates CyclinB1 and Securin in MCC active mitotic cell extracts isolated from RIT1 knockout cells (*39*). Supplementing these extracts with recombinant RIT1 increased ubiquitination and degradation of CyclinB1 and Securin, suggesting increased APC/C activity, likely due to relieved MCC inhibition (**Figures 2.4G, 2.8J-2.8K**). To evaluate APC/C activity *in vivo,* we measured the degradation of fluorescently-labeled CyclinB1 during mitosis. Consistent with delayed mitotic progression (**Figure 2.3A**), RIT1-depleted cells exhibited delayed CyclinB1 degradation (**Figure 2.4H**). Moreover, expression of RIT1^{M90I} accelerated CyclinB1 degradation under normal cell growth (**Figure 2.4I**); however, its effect on CyclinB1 degradation was abolished under pharmacologically-induced mitotic arrest (**Figure 2.8M**), suggesting that pathogenic levels of RIT1 cannot silence a hyperactive SAC response.

Discussion

Altogether, our findings demonstrate that RIT1 regulates mitotic fidelity through a direct complex formation with MAD2/p31^{comet} that results in suppression of the SAC response. CDK1/CyclinB1 regulates RIT1's dissociation from the PM during mitosis, a process necessary

for RIT1-mediated SAC suppression, and inhibits the formation of RIT1-MAD2-p31^{comet} complexes. CDK1 orchestrates mitotic progression through phosphorylation of various substrates and is most active during prometaphase (*40*). In line with this, we can deduce that CDK1/CyclinB1 modulates RIT1-mediated SAC inhibition during the early stages of mitosis when SAC signaling is essential for proper chromosome segregation (*8*). Pathogenic RIT1 levels suppress SAC signaling and we speculate that overabundant RIT1 escapes adequate CDK1 phosphorylation achieved under physiological RIT1 levels, resulting in a weakened SAC response. To fully understand the properties of RIT1 as an oncogenic driver, it will be paramount to investigate whether SAC silencing contributes to the pathogenesis of *de novo* RIT1 mutations that compromise RIT1 degradation, as this may provide an avenue for therapeutic intervention (*7*). It is tempting to speculate that RIT1 may provide a direct link between SAC regulation and RIT1 effector pathways involved in cell survival and stress response (*5*). Moreover, one can postulate that the RIT1-SAC signaling axis may have evolved as a mechanism that modulates SAC activity in response to mitogenic and stress signals. While previous reports have implicated pathogenic Ras GTPase signaling with genomic instability (*41–43*), our results show a direct link between the SAC and a member of the Ras GTPase family, providing a novel example of the evolutionary adaptation of a signaling molecule for the regulation of a unique but critical cellular pathway.

Figures

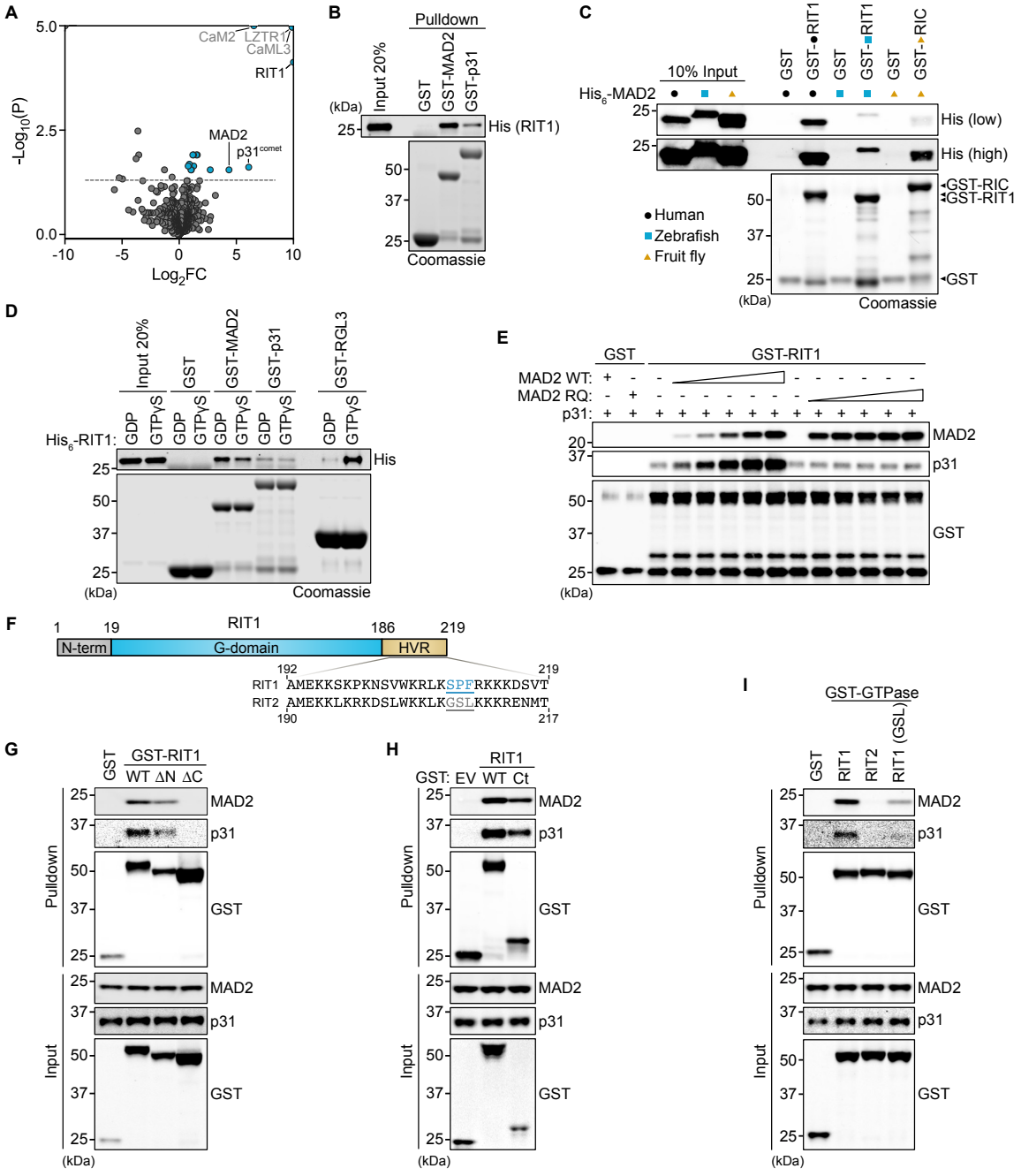

Figure 2.1: RIT1 interacts directly with the SAC proteins MAD2 and p31^{comet}

(**A**) Proteins obtained from lysates of HEK-293T cells transfected with FLAG-RIT1 or FLAG empty vector control were immunoprecipitated and analyzed by LC-MS/MS. Volcano plot shows enrichment of proteins detected in FLAG-RIT1 precipitates across three biologically independent repeats. Top hits included previously identified interactors: LZTR1, Calmodulin 2 (CaM2) and

Calmodulin-like protein 3 (CaML3). Log_2 fold change (Log_2FC) and $-Log_{10}$ adjusted p-value ($-Log_{10}(P)$) were capped at 10 and 5.0, respectively. Dashed line represents p-value of 0.05.
(**B**) GST pulldown assay with indicated recombinant purified GST-tagged proteins and His_6-RIT1.
(**C**) GST pulldown assay with 0.1 μM of the indicated recombinant purified GST-tagged RIT1 (either human or zebrafish ortholog) or RIC (Fruit fly RIT1 ortholog) proteins and 0.1 μM of the different MAD2 orthologs.
(**D**) GST pulldown assay as in (B), with His_6-RIT1 protein loaded with GDP or GTPγS. GST-RGL3 serves as a positive control for nucleotide loading due to the GTP-dependent nature of the RIT1-RGL3 interaction.
(**E)** GST pulldown assay with 0.1 μM recombinant GST or GST-RIT1 incubated with 0.5 μM $p31^{comet}$ and titration of MAD2 WT or the dimerization and $p31^{comet}$ binding deficient mutant MAD2 R133E/Q134A (RQ) (0, 0.1, 0.2, 0.4, 0.8 or 1.6 μM).
(**F**) Schematic of RIT1 domain structure with amino acid sequence alignment of RIT1 and RIT2 C-terminal tails.
(**G**, **H, I**) Proteins pulled down from extracts of HEK-293T cells transfected with GST, GST-RIT1, or GST-RIT1 mutant constructs. Immunoblots were probed for endogenous MAD2 and $p31^{comet}$. EV, empty vector. Ct, C-terminal (192-219).
(**I**) RIT1 (GSL), RIT1 construct with residues 209-211 (SPF) replaced with corresponding RIT2 residues 207-209 (GSL).
See also Figure 2.5.

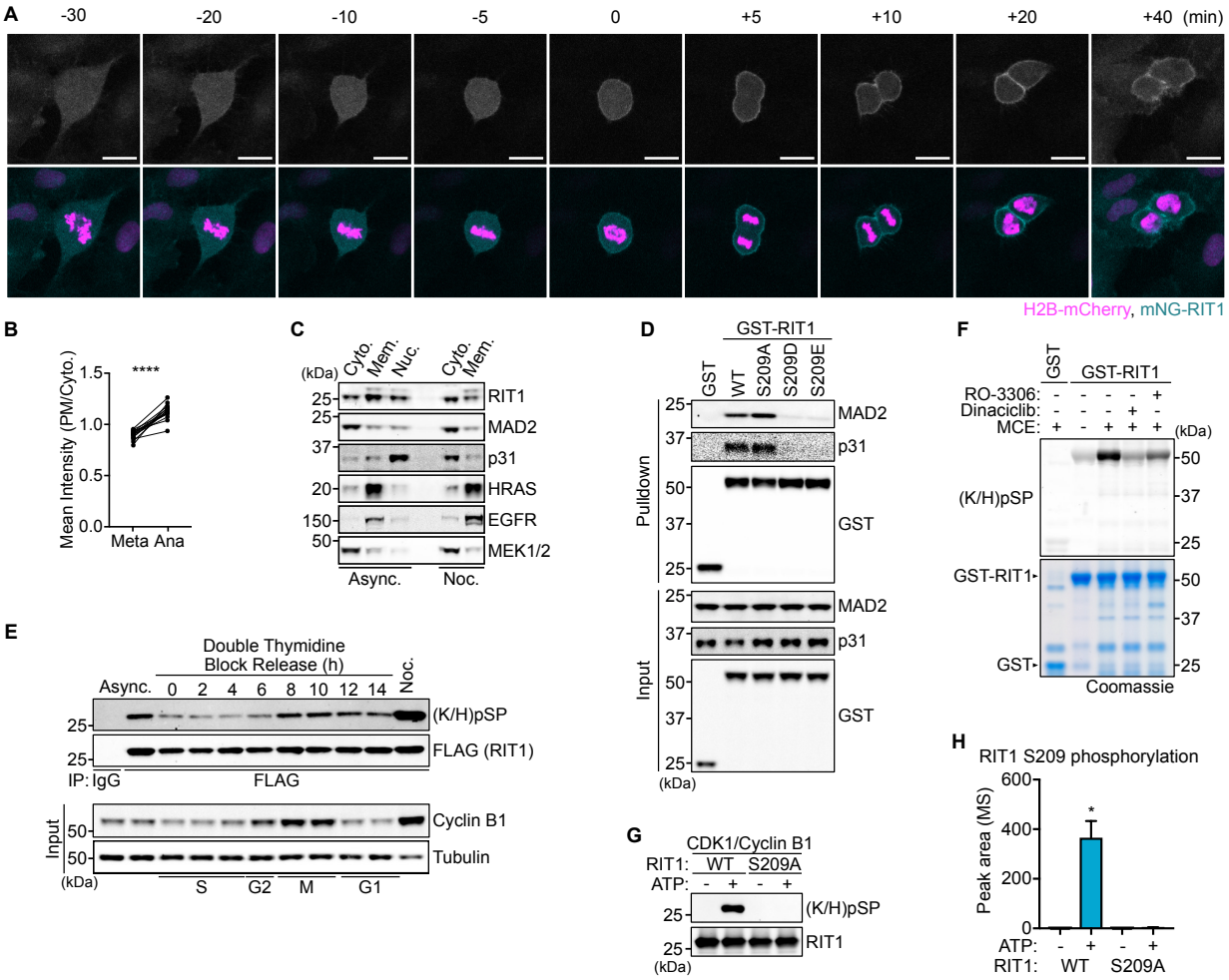

Figure 2.2: RIT1 interaction with MAD2 and p31^{comet} is regulated by CDK1 phosphorylation

(**A**) hTERT-RPE1 cell stably expressing mNeonGreen (mNG)-RIT1 and Histone H2B-mCherry undergoing mitosis imaged at 5 min intervals. Anaphase onset set to t = 0 min. Scale bar = 20 μm.

(**B**) Quantification of plasma membrane (PM) to cytoplasmic (Cyto.) ratio of mNG-RIT1 during metaphase (Meta, -5 min) and anaphase (Ana, +5 min) in cells as in (A). Two-sided Student's paired *t*-test, n = 15, ****$P \leq 0.0001$).

(**C**) Immunoblots of subcellular protein fractionation of HeLa cell lysates. Async., asynchronous growing cells. Noc., cells released from G1/S arrest for 4 hours then treated with 100 ng/ml nocodazole for 10 hours. HRAS included as a PM-bound protein control.

(**D**) Protein pulled down from extracts of HEK-293T cells transfected with GST or GST-RIT1 constructs. Immunoblots were probed for endogenous MAD2 and p31^{comet}.

(**E**) HeLa cells stably expressing FLAG-RIT1 released from a G1/S phase arrest and lysed at indicated time points. Immunoprecipitated proteins were probed for RIT1 S209 phosphorylation by immunoblotting. Async., asynchronous growing cells. Noc., cells released from G1/S arrest for 4 hours then treated with 100 ng/ml nocodazole for 10 hours.

(**F**) Detection of RIT1 S209 phosphorylation on bacterially expressed GST-RIT1 protein incubated with mitotic cell extract (MCE) treated with 1 μM Dinaciclib, 10 μM RO-3306, or DMSO control.
(**G**) Immunoblot of RIT1 S209 phosphorylation on bacterially expressed RIT1 proteins subjected to an *in vitro* kinase assay with recombinant active CDK1/Cyclin B1.
(**H**) MS quantification of phospho-S209 peptides in RIT1 protein incubated with CDK1/Cyclin B1 as in (G). (n = 2), Two-sided Student's t-test, data shown as mean, error bars indicate s.d., $^{*}P \leq 0.05$.
See also Figure 2.6.

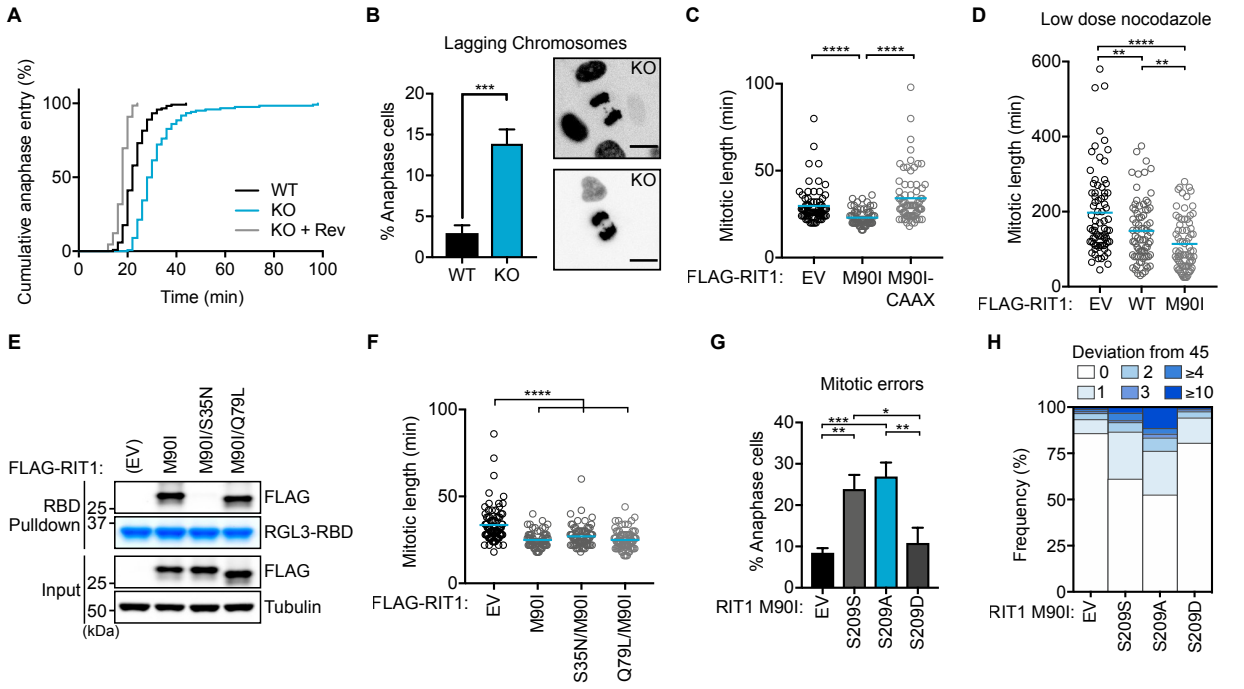

Figure 2.3: RIT1 regulates timely anaphase entry and chromosome segregation fidelity

(**A**) Comparison of mitotic transit times between WT and RIT1 KO hTERT-RPE1 cells assessed by time-lapse microscopy. Time measured from nuclear envelope breakdown (NEBD). Rev, cells treated with 1 μM Reversine. WT (*n* =119), KO (*n* = 122), KO + Rev (*n* = 66).

(**B**) Quantification of lagging chromosomes in anaphase hTERT RPE1 cells. Data represent three independent replicates with three WT clones and three KO clones. Error bars indicate s.d., ****P* ≤ 0.001.

(**C**, **D**) Duration of mitotic length (NEBD - anaphase onset) assessed by time-lapse microscopy in U2-OS cells stably expressing indicated proteins in (C) normal growth conditions [EV (*n* = 76), M90I (*n* = 66), M90I-CAAX (*n* = 72)] or (D) treated with 15 ng/ml nocodazole (*n* = 75). Two-sided Student's *t*-test, error bars indicate s.d., ***P* ≤ 0.01, ****P* ≤ 0.001, *****P* ≤ 0.0001.

(**E**) Immunoblots of GST-RGL3 RBD pulldown assay with lysates from U2OS cells stably expressing indicated RIT1 constructs. RGL3-RBD protein stained with Coomassie.

(**F**) Duration of mitotic length (NEBD - anaphase onset) assessed by time-lapse microscopy in U2-OS cells stably expressing indicated proteins in normal growth conditions, EV (*n* = 81), M90I (*n* = 68), M90I/S35N (*n* = 75), M90I/Q79L (*n* = 77). Two-sided Student's *t*-test, error bars indicate s.d., *****P* ≤ 0.0001.

(**G**) Comparison of chromosome segregation error rates (lagging and bridging chromosomes) in HCT-116 cells stably expressing indicated constructs. EV, empty vector. Data represent three biologically independent repeats. Two-sided Student's *t*-test, error bars indicate s.d., **P* ≤ 0.05, ***P* ≤ 0.01, ****P* ≤ 0.001.

(**H**) Metaphase spread assay compares frequency of aneuploidy, determined by a chromosome count other than the modal number, 45, in HCT-116 cells stably expressing EV (*n* = 92), S209S (*n* = 98), S209A (*n* = 97), or S209D (*n* = 88).

For (A, C, D, F-H), *n* indicates the number of cells or metaphase spreads counted and data shown is representative of at least two biologically independent experiments.

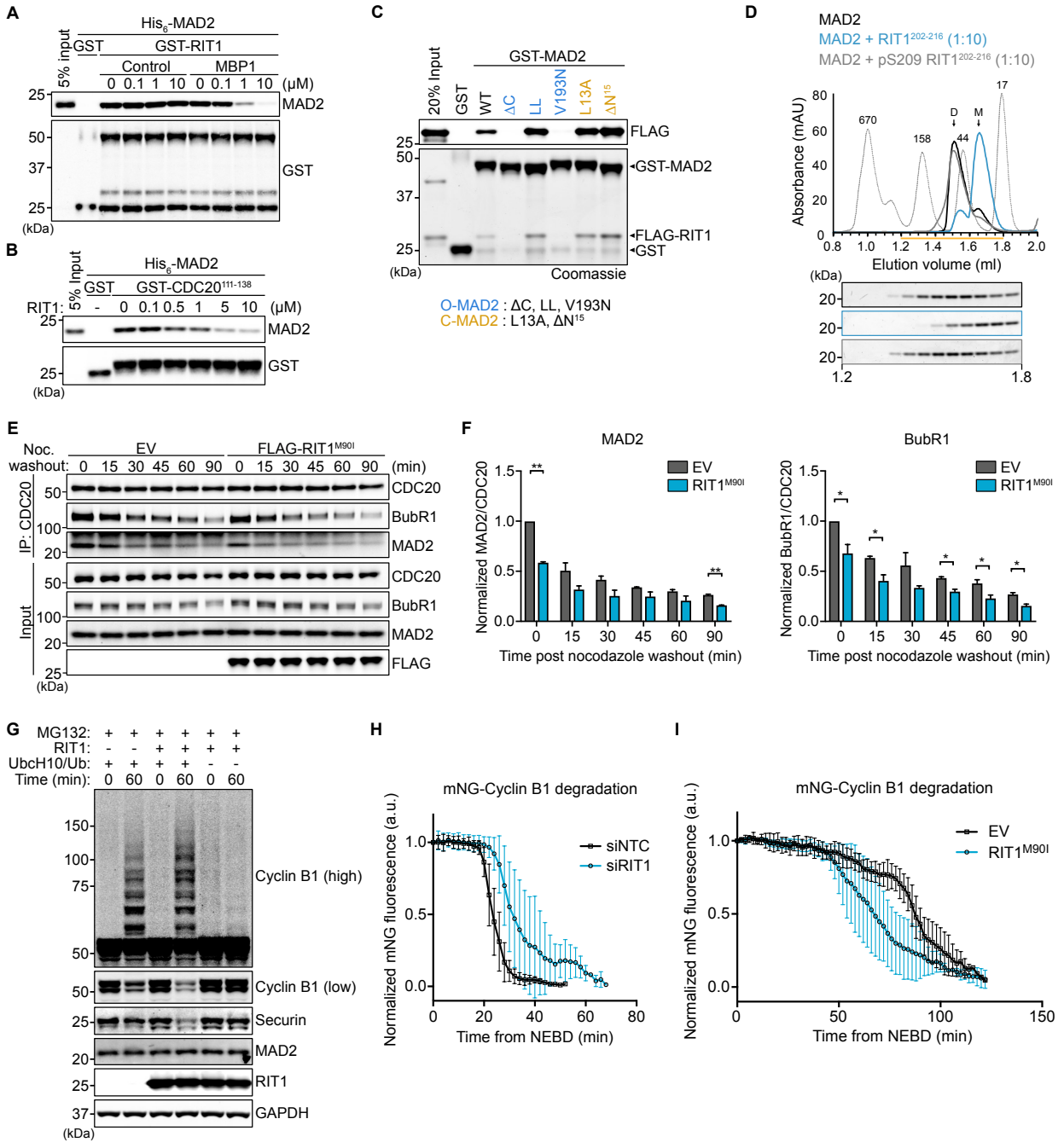

Figure 2.4: RIT1 inhibits MCC-MAD2 association and promotes degradation of APC/C substrates

(**A**, **B**) Immunoblots of precipitated proteins from an equilibrium competition pulldown assay with 0.2 μM recombinant (A) GST-RIT1 or (B) GST-CDC20 111-138 protein incubated with 0.2 μM

His_6-MAD2 and titrating amounts of (A) MAD2 binding peptide 1 (MBP1) or a control peptide or (B) full-length RIT1 protein.
(**C**) Pulldown assay with 0.5 μM recombinant GST or GST-MAD2 proteins incubated with 0.5 μM FLAG-RIT1 protein. Precipitated proteins were separated by SDS-PAGE for immunoblot or Coomassie staining.
(**D**) Elution profile of MAD2 protein incubated with or without indicated peptides at 1:10 molar ratio for 1 hour at 25°C prior to gel filtration. The contents of 12 consecutive 50 μl fractions eluting between 1.2 ml to 1.8 ml are shown.
(**E**) Immunoblots of anti-CDC20 immunoprecipitated (IP) proteins from cells expressing empty vector (EV) or $RIT1^{M90I}$ at indicated time points following nocodazole washout. IP proteins probed from the same membrane.
(F) Quantification of data in (E); CoIP MAD2 or BubR1 band intensity normalized to CDC20 band intensity. Ratios normalized to EV time = 0 min. Two-sided Student's *t*-test, error bars indicate s.d., (n = 2) *$P \leq 0.05$, **$P \leq 0.01$.
(**G**) Immunoblots of samples from APC/C ubiquitination assay with and without 10 μM RIT1. To prevent degradation of ubiquitinated proteins, mitotic cell extracts were incubated with 10 μM MG132 for 1 hour on ice, prior to supplementation with additional ubiquitination assay components.
(H, I) Quantification of mNeonGreen (mNG)-Cyclin B1 mean intensity normalized to signal intensity at NEBD (t = 0), in H2B-mCherry expressing (H) RPE1 cells treated with indicated siRNA for 72 h prior to imaging (n = 6, from two independent experiments) or (I) HeLa cells expressing indicated constructs. Cells were imaged at 2 min intervals. (n = 5, from 2 independent experiments). Data represent mean ± s.d.
See also Figure 2.8.

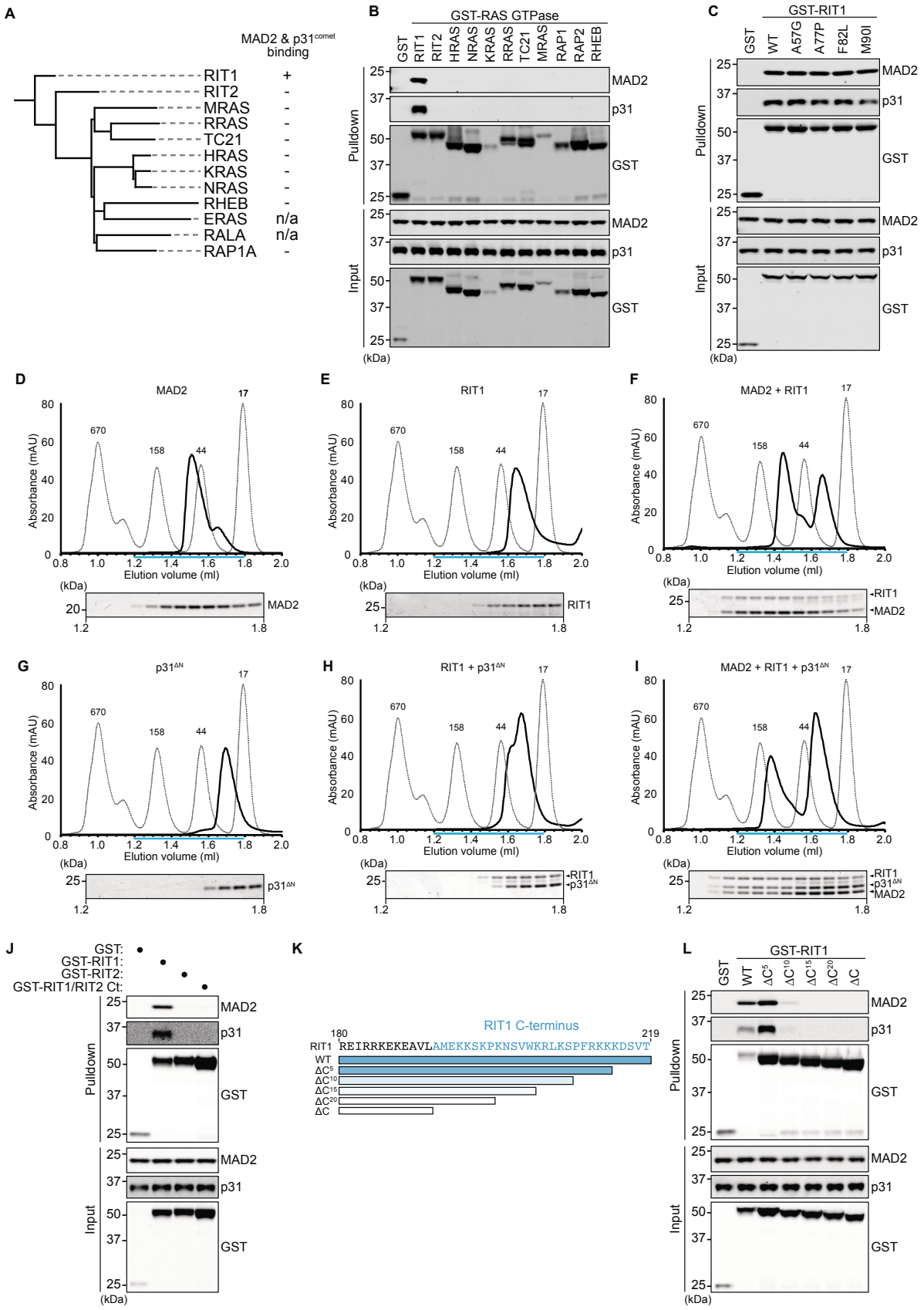
A
MAD2 & p31comet binding
RIT1 +
RIT2 -
MRAS -
RRAS -
TC21 -
HRAS -
KRAS -
NRAS -
RHEB -
ERAS n/a
RALA n/a
RAP1A -
B
GST-RAS GTPase
GST RIT1 RIT2 HRAS NRAS KRAS RRAS TC21 MRAS RAP1 RAP2 RHEB
Pulldown
Input
MAD2
p31
GST
(kDa)
C
GST-RIT1
GST WT A57G A77P F82L M90I
D
MAD2
E
RIT1
F
MAD2 + RIT1
G
p31ΔN
H
RIT1 + p31ΔN
I
MAD2 + RIT1 + p31ΔN
Absorbance (mAU)
Elution volume (ml)
670
158
44
17
J
GST:
GST-RIT1:
GST-RIT2:
GST-RIT1/RIT2 Ct:
K
RIT1 C-terminus
RIT1 REIRRKEKEAVLAMEKKSKPKNSVWKRLKSPFRKKKDSVT
WT
ΔC5
ΔC10
ΔC15
ΔC20
ΔC
L
GST-RIT1
GST WT ΔC5 ΔC10 ΔC15 ΔC20 ΔC

Figure 2.5: RIT1, but not other Ras GTPases, forms a complex with MAD2 and p31comet mediated by its C-terminal extension, related to Figure 2.1.

(**A**) Summary of MAD2 and p31^{comet} binding exhibited by closely related Ras family GTPases.
(**B**) Representative immunoblot of data summarized in (A) showing proteins precipitated from extracts of HEK-293T cells transfected with GST or a GST-Ras GTPase construct probed for endogenous MAD2 or p31^{comet}.
(**C**) Analysis of MAD2 and p31^{comet} binding to disease-associated RIT1 mutants within switch I and switch II domains. Immunoblots of proteins precipitated from extracts of HEK-293T cells transfected with GST or indicated GST-RIT1 constructs and probed for endogenous MAD2 or p31^{comet}.
(**D**-**I)** RIT1, MAD2, and p31^{comet} proteins were allowed to complex at 25°C for 1 hour prior to gel filtration. Elution profiles were compared to that of known standards (thin dashed line). For every chromatogram, the contents of 12 consecutive 50 µl fractions eluting between 1.2 ml to 1.8 ml were separated by SDS-PAGE and stained with Coomassie. (**D**) elution profile of bacterially expressed MAD2, with the minor peak corresponding to monomeric MAD2 and the major peak representing dimerization of MAD2 between O-MAD2 and C-MAD2 conformers. (**E**) Elution profile of full-length RIT1, showing a single monomeric peak. (**F**) Elution profile of MAD2 and RIT1 demonstrates complex formation between RIT1 and dimeric MAD2. (**G**) Elution of profile of p31^{comet} ΔN. (**H)** No complex formation between RIT1 and p31^{comet} ΔN can be observed by size exclusion under assay conditions. Identical results are observed with full-length p31^{comet} protein. (**I**) Elution profile RIT1, MAD2, and p31^{comet} shows that incubation of all three proteins allows for the formation of a high molecular weight complex that includes MAD2, RIT1 and p31^{comet}.
(**J, L**) Immunoblots of proteins precipitated from extracts of HEK-293T cells transfected with GST or indicated GST-RIT1 or RIT2 constructs and probed for endogenous MAD2 or p31^{comet}.
(**J**) RIT1/RIT2 Ct, a chimeric protein with RIT1 residues 194-219 replaced with RIT2 residues 192-217. (**K**) Diagram of RIT1 C-terminal truncation mutants used in (L).

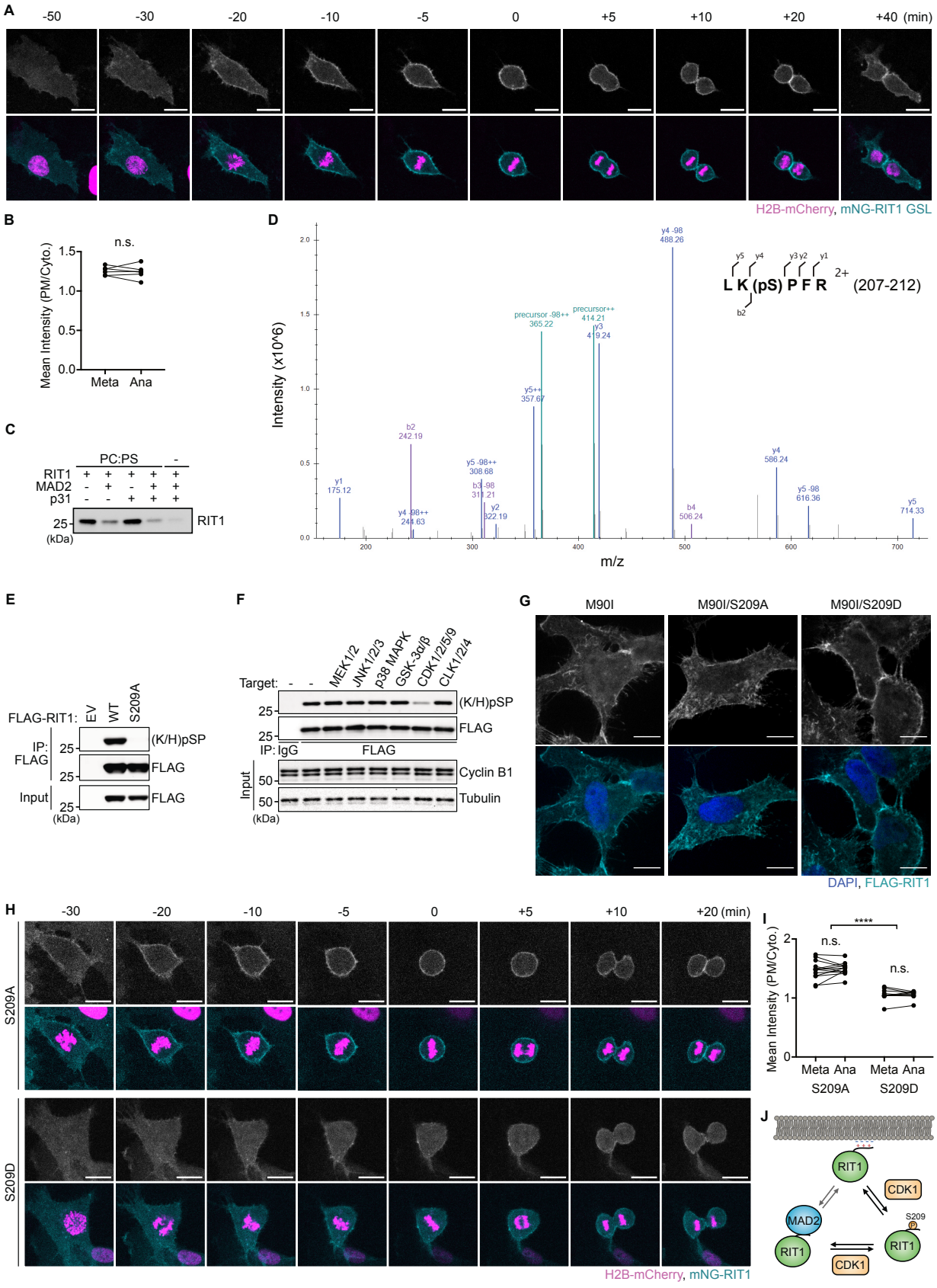
A
-50
-30
-20
-10
-5
0
+5
+10
+20
+40 (min)
H2B-mCherry, mNG-RIT1 GSL
B
n.s.
Mean Intensity (PM/Cyto.)
Meta
Ana
C
PC:PS
RIT1
MAD2
p31
25
(kDa)
RIT1
D
Intensity (x10^6)
m/z
L K (pS) P F R
2+
(207-212)
E
FLAG-RIT1:
EV
WT
S209A
IP: FLAG
(K/H)pSP
FLAG
Input
FLAG
F
Target:
MEK1/2
JNK1/2/3
p38 MAPK
GSK-3α/β
CDK1/2/5/9
CLK1/2/4
(K/H)pSP
FLAG
IP: IgG
FLAG
Input
Cyclin B1
Tubulin
G
M90I
M90I/S209A
M90I/S209D
DAPI, FLAG-RIT1
H
-30
-20
-10
-5
0
+5
+10
+20 (min)
S209A
S209D
H2B-mCherry, mNG-RIT1
I
****
n.s.
n.s.
Mean Intensity (PM/Cyto.)
Meta
Ana
Meta
Ana
S209A
S209D
J
RIT1
CDK1
MAD2
S209
P
RIT1
RIT1
CDK1

Figure 2.6: Phosphorylation of RIT1 S209 regulates its subcellular distribution during mitosis, related to Figure 2.2.

(**A**) hTERT-RPE1 cell stably expressing mNeonGreen (mNG)-RIT1 GSL and Histone H2B-mCherry undergoing mitosis imaged at 5 min intervals. Anaphase onset set to t = 0 min. Scale bar, 20 μm.
(**B**) Quantification of the ratios of plasma membrane (PM) and cytoplasmic (Cyto.) mNG-RIT1 signals of cells in (A) during metaphase (Meta, -5 min) and anaphase (Ana, +5 min). Two-sided Student's paired *t*-test, n = 6, n.s, not statistically significant.
(**D**) Immunoblot of RIT1 from liposome binding assay. RIT1 protein alone or complexed with MAD2 and/or p31^{comet} was incubated with phosphatidylcholine (PC) and phosphatidylserine (PS) liposomes (70:30) for 1hr and pelleted by ultracentrifugation.
(**D**) Representative MS2 spectrum from RIT1 phosphopeptide. The annotated peptide sequence includes b-series (˛) and y-series (˚) ions, precursor charge state, and the residues within the RIT1 protein sequence.
(**E**) Validation of phospho-serine -1(K/H)/+1P antibody for detection of RIT1 S209 phosphorylation. Immunoblot of FLAG-RIT1 immunoprecipitated from HEK-293T cells expressing RIT1 WT or S209A and probed with an antibody against (K/H)pSP. EV, empty vector.
(**F**) HeLa cells stably expressing FLAG-RIT1 were arrested in prometaphase and were kept in mitosis with MG132 (10 μM) while being treated with 1 μM of the following inhibitors for 4 hours: Trametinib (MEK1/2i), JNK-IN-8 (JNK1/2/3i), Losmapimod (p38 MAPKi), CHIR-99021 (GSK-3α/βi), Dinaciclib (CDK1/2/5/9i), TG003 (CLK1/2/4i). FLAG-RIT1 was immunoprecipitated and subjected to immunoblotting for detection of S209 phosphorylation.
(**G**) Representative immunofluorescence images of interphase HeLa cells stably expressing indicated FLAG-tagged RIT1 mutant constructs. Scale bar, 10 μm.
(**H**) hTERT-RPE1 cell stably expressing mNG-RIT1 S209A or S209D and Histone H2B-mCherry undergoing mitosis imaged at 5 min intervals. Anaphase onset set to t = 0 min. Scale bar, 20 μm.
(**I**) Quantification of the ratios of plasma membrane (PM) and cytoplasmic (Cyto.) mNG-RIT1 signals of cells in (H) during metaphase (Meta, -5 min) and anaphase (Ana, +5 min). Two-sided Student's paired *t*-test, S209A (n = 13), S209D (n = 10) , ****$P \leq 0.0001$, n.s, not statistically significant.
(**J**) Schematic model depicting distinct RIT1 populations during mitosis and their regulation by CDK1.

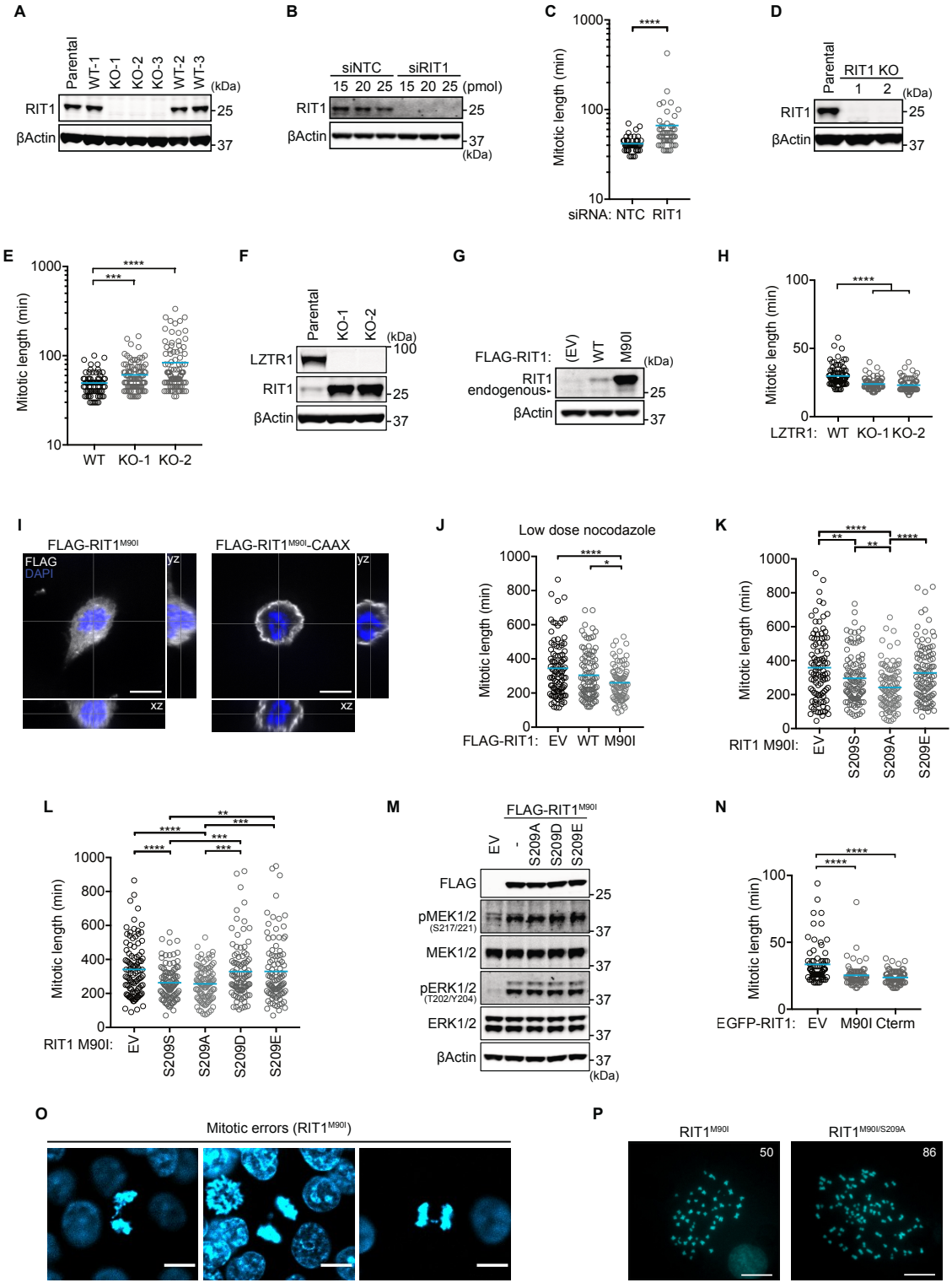

Figure 2.7: Inhibition of the SAC by RIT1 is dependent on MAD2 and p31comet binding, related to Figure 2.3.

(**A**) Immunoblots of lysates from WT and RIT1 KO hTERT-RPE1 clones.

(**B**) Immunoblots of lysates from HeLa cells harvested 72 h after transfection with RIT1 or nontargeting control (siNTC) siRNA.
(**C**) Duration of mitotic length (NEBD - anaphase onset) assessed by time-lapse microscopy in HeLa cells transfected with indicated siRNA 72 hours prior to the start of imaging. (*n* = 50).
(**D**) Immunoblots of lysates from parental HeLa cells and RIT1 KO HeLa clonal cell lines.
(**E**) Mitotic length measured as in (C) in Parental HeLa cells (*n* = 75) and in two RIT1 KO clones (*n* = 100),
(**F**) Immunoblots of lysates from parental and LZTR1 KO U2OS cells.
(**G**) Immunoblots of lysates from U2-OS stably expressing indicated constructs.
(**H**) Mitotic length measured as in (C) in Parental U2OS cells (*n* = 86) and in LZTR1 KO clones 1 (*n* = 80) and 2 (*n* = 74).
(**I**) Representative immunofluorescence images of nocodazole-treated prometaphase U2OS cells stably expressing indicated FLAG-tagged RIT1 mutant constructs. Scale bar, 10 μm.
(**J**) Duration of mitotic length as in (C) in HeLa cells stably expressing indicated proteins treated with 15 ng/ml nocodazole (EV, WT, M90I, *n* = 98, 99, 84) or DMSO control (*n* = 50).
(**K**, **L**) Duration of mitotic length as in (C) in (K) HeLa, *n* = 100, or (L) hTERT-RPE1, *n* ≥ 100, cells stably expressing indicated proteins treated with 15 ng/ml nocodazole.
(**M**) Immunoblots of cell lysates from HEK-293T cells transfected with indicated constructs and serum-starved for 16 hours. EV, empty vector.
(**O**) Representative images of mitotic errors from HCT-116 cells stably expressing RIT1 M90I and quantified in Figure 3G. Scale bar, 10 μm.
(**P**) Representative images of metaphase spreads quantified in Figure 3H. The inscribed number indicates the chromosome count. Scale bar, 10 μm. (**C, E, H, J-L, N**) *n* indicates the number of cells counted per condition. Two-sided Student's *t*-test, bars indicate mean. **P* ≤ 0.05, ***P* ≤ 0.01, ****P* ≤ 0.001, *****P* ≤ 0.0001.

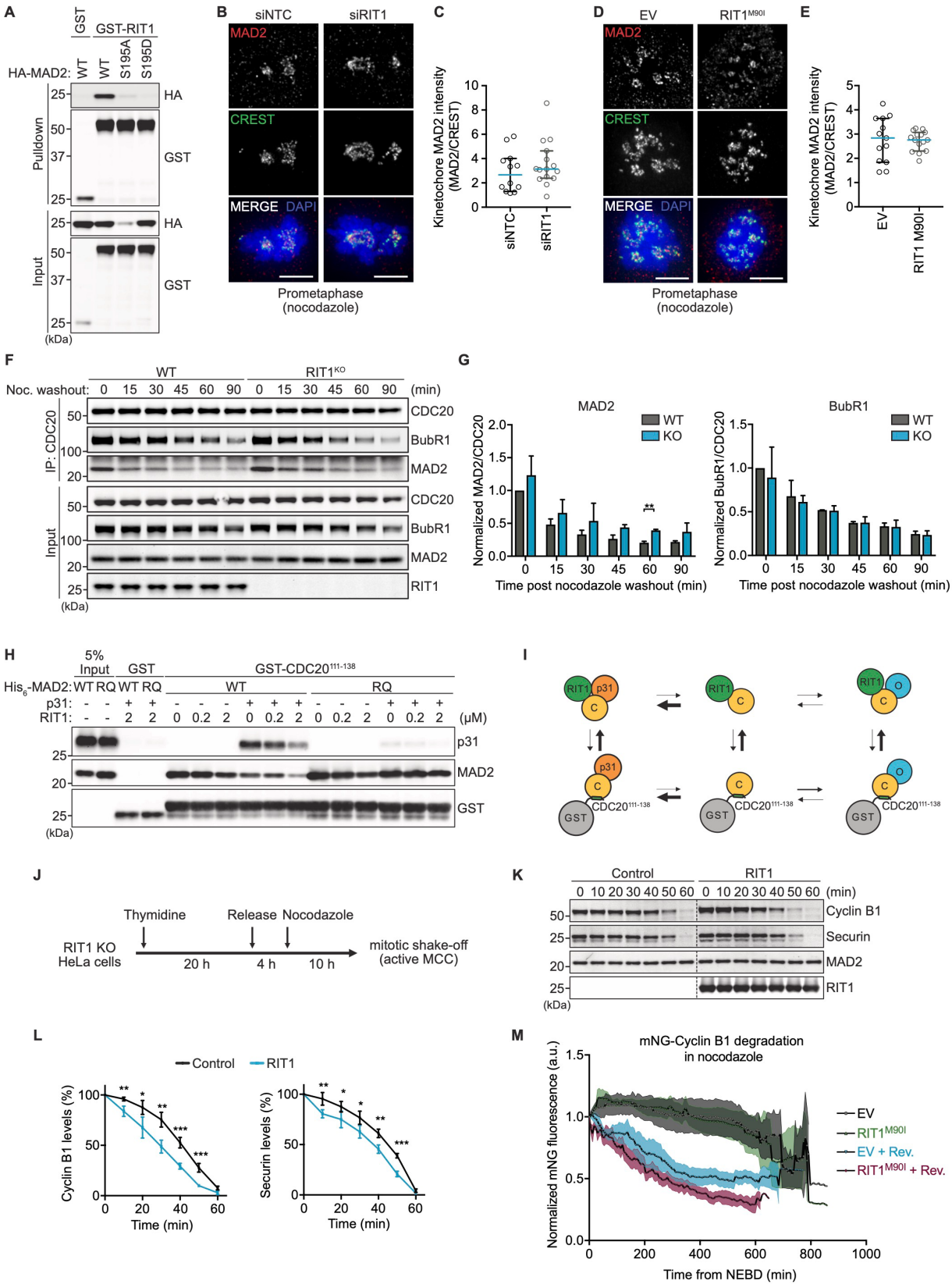
A
GST
GST-RIT1
HA-MAD2: WT WT S195A S195D
Pulldown
Input
HA
GST
(kDa)
B
siNTC
siRIT1
MAD2
CREST
MERGE DAPI
Prometaphase (nocodazole)
C
Kinetochore MAD2 intensity (MAD2/CREST)
siNTC
siRIT1
D
EV
RIT1M90I
Prometaphase (nocodazole)
E
Kinetochore MAD2 intensity (MAD2/CREST)
EV
RIT1 M90I
F
WT
RIT1KO
Noc. washout: 0 15 30 45 60 90 0 15 30 45 60 90 (min)
IP: CDC20
Input
CDC20
BubR1
MAD2
RIT1
(kDa)
G
MAD2
BubR1
WT
KO
Normalized MAD2/CDC20
Normalized BubR1/CDC20
Time post nocodazole washout (min)
H
5% Input
GST
GST-CDC20111-138
His6-MAD2: WT RQ WT RQ
WT
RQ
p31:
RIT1: (μM)
p31
MAD2
GST
(kDa)
I
RIT1
p31
C
O
GST
CDC20111-138
J
Thymidine
Release
Nocodazole
RIT1 KO HeLa cells
20 h
4 h
10 h
mitotic shake-off (active MCC)
K
Control
RIT1
0 10 20 30 40 50 60 0 10 20 30 40 50 60 (min)
Cyclin B1
Securin
MAD2
RIT1
(kDa)
L
Control
RIT1
Cyclin B1 levels (%)
Securin levels (%)
Time (min)
M
mNG-Cyclin B1 degradation in nocodazole
Normalized mNG fluorescence (a.u.)
EV
RIT1M90I
EV + Rev.
RIT1M90I + Rev.
Time from NEBD (min)

Figure 2.8: RIT1 inhibits the SAC by cooperating with p31comet downstream of kinetochores to sequester MAD2 away from CDC20, related to Figure 2.4.

(**A**) Immunoblots of proteins precipitated from extracts of HEK-293T cells transfected with GST or GST-RIT1 and hemagglutinin (HA)-tagged MAD2 S195 mutants. S209A mutation significantly reduced expression levels of MAD2, but S209A protein can still be detected in pulldown fractions.
(**B**) Representative immunofluorescence images of prometaphase RPE1 cells treated with indicated siRNA for 72 hrs and treated with nocodazole (100ng/ml) for 1 hour prior to fixing. Scale bar, 5 μm.
(**C**) Quantification of mean kinetochore MAD2 fluorescence intensity normalized to CREST signal in images represented in (B). siNTC (n = 12), siRIT1 (n = 15), from two independent experiments. Horizontal line and error bars represent the median and 95% confidence interval, respectively.
(**D**) Representative immunofluorescence images of prometaphase HeLa cells expressing empty vector (EV) or RIT1 M90I and treated with nocodazole (100ng/ml) for 1 hour prior to fixing. Scale bar, 5 μm.
(**E**) Quantification of mean kinetochore MAD2 fluorescence intensity normalized to CREST signal in images represented in (D). EV (n = 13), RIT1 M90I (n = 15), from two independent experiments. Horizontal line and error bars represent the median and 95% confidence interval, respectively.
(**F**) Immunoblots of anti-CDC20 immunoprecipitated (IP) proteins from WT HeLa or RIT1 KO cells at indicated timepoints following nocodazole washout. IP proteins probed from same membrane.
(G) Quantification of data in (E); CoIP MAD2 or BubR1 band intensity normalized to CDC20 band intensity. Ratios normalized to WT, time = 0 min. Two-sided Student's t-test, error bars indicate s.d., (n = 2) $^{**}P \leq 0.01$.
(**H**) Immunoblots of GST pulldown assay with 0.5 μM recombinant GST or GST-CDC20 111-138 incubated with or without 0.5 μM $p31^{comet}$, 0.2 μM MAD2 WT or MAD2 R133E/Q134A (RQ) protein and RIT1 protein at indicated concentrations.
(**I**) Schematic representation of results from experiment in (A).
(**J**) Diagram of cell synchronization strategy to generate mitotic cell extracts with active MCC for APC/C activity assays.

(**K**) Representative immunoblots of data quantified in (L). APC/C activity assay following degradation of Cyclin B1 and Securin at indicated time points in the absence of MG132.
(**L**) Comparison of Cyclin B1 (left panel) and Securin (right panel) degradation in APC/C activity assays supplemented with or without recombinant RIT1 protein (10 μM). Data represent four biologically independent repeats. Two-sided Student's t-test, data points are mean ± s.d., $^{*}P \leq 0.05$, $^{**}P \leq 0.01$, $^{***}P \leq 0.001$.
(M) Quantification of mNeon-Green (mNG)-Cyclin B1 mean intensity normalized to signal intensity at NEBD (t = 0), in HeLa cells expressing Histone H2B-mCherry and EV or RIT1 M90I. Cells were treated with 100ng/ml nocodazole and with or without 0.5 μM Reversine for 1 hour prior to imaging. Cells were imaged at 6 min intervals ($n \geq 7$, from 2 independent experiments). Data represent mean ± s.e.m.

EXPERIMENTAL MODEL AND SUBJECT DETAILS

Cells and culture conditions

HEK-293T, HeLa, U2-OS, HCT-116, and hTERT RPE-1 cells were obtained from the American Type Culture Collection (ATCC). HEK-293T, HeLa and U2-OS cells were cultured in Dulbecco's modified Eagle's medium (DMEM) supplemented with 10% Fetal Bovine Serum (FBS). hTERT RPE-1 cells were cultured in DMEM/F12 medium supplemented with 10% FBS. Cells were grown in a humidified incubator with 5% CO2 at 37 °C. Validation procedures are as described by the manufacturer. Cell lines were regularly tested and verified to be mycoplasma negative using MycoAlert PLUS Mycoplasma Detection Kit (Lonza).

METHOD DETAILS

Reagents, antibodies, and immunoblotting

Nocodazole, Reversine, Dinaciclib, RO-3306, JNK-IN-8, CHIR-99021, TG003, Losmapimod, and Trametinib were purchased from Selleckchem. MG132, Thymidine, ATP, phospho-creatine, GDP and GTPγS were purchased from Sigma-Aldrich. RIT1 (202-216), pS209 RIT1 (202-216), MBP1 (SWYSYPPPQRAV) and control (SYWPQRAPPSVY) peptides were obtained from GenScript. Antibodies against p-ERK (4370; 1:1000), ERK1/2 (4696; 1:2000), p-MEK (9154; 1:1000), MEK1/2 (4694; 1:1000), Cyclin B1 (4135, 1:1000), HA (3724, 1:1000), FLAG (14793; 1:1000), GST (2625; 1:1000), and (K/H)pSP (9477, 1:1000) were obtained from Cell Signal Technology. Antibodies recognizing Securin (PTTG) (sc-56207; 1:250), MAD2 (sc-47747; 1:250) and GST (sc-138; 1:1000) were obtained from Santa Cruz Biotechnology. RIT1 antibody (ab53720; 1:1000) was from Abcam. $p31^{comet}$ antibody (MABE451; 1:500) was from EMD Millipore. MAD2 antibody (A300-301A; 1:1000) was from Bethyl Laboratories. βActin (A2228; 1:10000), α-Tubulin (T6199; 1:5000), FLAG (F1804; 1:2000) and His_6 (05-949; 1:1000) antibodies were purchased from Sigma-Aldrich. Whole cell lysates were prepared using RIPA Buffer (50 mM Tris-HCl (pH 8.0),

150 mM NaCl, 0.5% Deoxycholate, 0.1% SDS, 1% IGEPAL CA-630) supplemented with protease and phosphatase inhibitor cocktails (Sigma-Aldrich). 20-30 µg of total protein was loaded per well of pre-casted NuPAGE gels (Life Technologies). For immunoblot detection, samples were separated by SDS-PAGE and transferred onto nitrocellulose membranes. Membranes were blocked using 5% skimmed milk in TBST buffer for 1 hour and incubated with appropriate primary antibodies overnight. Detection was performed using secondary antibodies conjugated to DyLight680 (611-144-002; 1:10,000) or DyLight800 (610-145-002; 1:10,000) (Rockland), and visualized with a LI-COR Odyssey infrared scanner.

Plasmids, cloning and transfection

All RIT1 mutations used in this paper were generated by standard PCR-based mutagenesis in the pDONR223-RIT1 template. These included ΔN, ΔC (and all C-terminal truncations), GSL, S209A, S209D, S209E, A57G, A77P, F82L, M90I, S35N,(*44*) and Q79L.(*45*) Mutagenesis primer sequences are available upon request. RIT2 (Isoform 1, NM_002930.4), RIT1 (RIT2 Ct) chimera, and mNeonGreen-RIT1 were synthesized as a gene block and cloned into pDONR221 (Invitrogen) using BP reaction. LR Gateway cloning yielded mammalian expression vectors with indicated tags. For N-terminal GST-tagged proteins, entry clones were cloned into pDEST27 destination vector (Invitrogen). For FLAG-tagged proteins, entry clones were cloned by multisite gateway cloning into pDEST302, pDEST663 or pDEST686 (a gift from Dominic Esposito, Frederick National Lab), and designed to express N-terminal 3xFLAG tag fusion proteins driven by an EF1a promoter.(*46*) Empty vector (EV) plasmid controls were generated using a gateway recombination cassette containing a stop codon followed by an untranslated stuffer sequence. The GST-tagged Ras Family GTPases panel was cloned in the pDEST27 vector and was previously described.(*6*) MAD2 cDNA (NM_002358.3) was purchased from GeneCopoeia as a Gateway entry clone and was recombined into pcDNA3-HA destination vector to be expressed an N-terminal HA-tagged fusion protein. MAD2 S195A and S195D were generated by PCR-based

mutagenesis. All plasmid transfections in this study were performed using JetPRIME transfection reagent (Polyplus Transfection) according to manufacturer's instructions.

Constructs used for bacterial expression were generated from as follows: a gene block containing *E. coli* codon-optimized human RIT1 (a.a.1-219), with an N-terminal TEV cleavage site followed by a FLAG-tag, was cloned into pDONR221 (Invitrogen). Similarly, gene blocks encoding *E. coli* codon-optimized human MAD2 (1-205) and $p31^{comet}$ (1-274), both with an N-terminal TEV cleavage site, were synthesized and cloned into pDONR221. MAD2 R133E/Q134A (RQ); ΔC (1-195); Loop-less (LL), in which residues 109-117 are replaced with a Gly-Ser-Gly linker; V193N; L13A; and ΔN15 (16-195); and $p31^{comet}$ΔN were generated by standard PCR-based mutagenesis.(*15*) $p31^{comet}$ΔN (50-274) was generated to enhance protein stability through deletion of its non-conserved and disordered N-terminal fragment.(*16*) Zebrafish (*Danio rerio*) and Fruit fly (*Drosophila melanogaster*) MAD2 and RIT1 orthologs were synthesized as *E. coli* codon-optimized gene blocks and cloned into pDONR221. RGL3-RBD (604-703) was synthesized as an *E. coli* codon-optimized gene block and subcloned into pGEX-6P-3 at EcoRI and XhoI restriction sites. All plasmids were verified by Sanger sequencing.

RNA interference

The short interfering RNAs (siRNAs) used in this study are siRIT1 (SMARTpool: ON-TARGETplus RIT1, Horizon) and siNTC (ON-TARGETplus Non-targeting Control Pool, D-001810-10-05, Horizon). Cells were transfected with siRNAs using Lipofectamine RNAi Max Transfection Reagent (Life Technologies) according to manufacturer's instructions.

Generation of CRISPR/Cas9-mediated knockout cells

RIT1 knockout (KO) clones were generated using two sgRNA targeting exon 2 of RIT1: sgRIT1-1: GATTCTGGAACTCGCCCAGT and sgRIT1-2: GGAGTACAAACTAGTGATGC. LZTR1 KO

clones were generated sgRNA previously described; sgLZTR1-1: AGTCTTTCACATCGAACCGC and sgLZTR1-2: CTTTACTCAGGGGGTTACAC. Briefly, Parental cells were transiently transfected with plasmid encoding an individual sgRNA, SpCas9, and EGFP (PX458, Addgene, plasmid #48138). 48 h post-transfection, GFP+ cells were single-cell sorted into 96-well plates using a SONY SH800 FACS. Clones were expanded and KO clones were validated by Sanger sequencing and Western blot analysis.

Lentiviral transduction

Lentivirus was produced by co-transfection of HEK-293T cells with a lentiviral vector and the packaging plasmids psPAX2 (Addgene, plasmid #12260) and pMD.2G (Addgene, plasmid #12259) at a ratio of 1.25:1.0:0.25. The supernatant was collected 72 hours post-transfection and filtered through a 0.45 µm filter. Cells were transduced with lentiviral-containing supernatant supplemented with 0.8 µg/ml polybrene (Sigma-Aldrich). Stably transduced cells were selected with appropriate antibiotic and maintained in media containing 50% antibiotic used during selection.

Bacterial protein expression and purification

Full-length recombinant RIT1 protein was obtained by gateway cloning pDONR-TEV-FLAG-RIT1 WT or S209A into pDEST566 (Addgene, plasmid #11517) containing an N-terminal hexahistidine-maltose binding protein (His_6-MBP) tag. Expression constructs were transformed into the *E. coli* strain BL21(DE3) (New England Biolabs). Protein expression was induced in cultures at OD_{600} between 0.4-0.6 with 200 µM Isopropyl β-D-1-thiogalactopyranoside (IPTG) (Sigma-Aldrich) for 14-16 h at 18°C. Cells were lysed by sonication in 100 mM Sodium phosphate (pH 6.0), 300 mM NaCl, 10 mM $MgCl_2$, 5% glycerol, 2 mM DTT, 1 mg/ml DNAse I, 0.2 mg/ml lysozyme, 30 mM imidazole and protease inhibitor cocktail (Sigma-Aldrich, P8849). After clearing, the lysate was loaded on a HisTrap FF metal chelating column (Cytiva Life Sciences) equilibrated in 100 mM

Sodium phosphate (pH 6.0), 300 mM NaCl, 10 mM $MgCl_2$, 5% glycerol, 30 mM imidazole. Bound proteins were eluted with 300 mM imidazole. Fractions containing RIT1 were pooled and dialyzed overnight in the presence of TEV-protease (Sigma-Aldrich). Cleaved protein was recovered by subtractive purification, concentrated by ultrafiltration, and further separated by size exclusion chromatography (SEC) on a Superdex-75 column (Cytiva Life Sciences) equilibrated in 100 mM Sodium phosphate (pH 6.0), 300 mM NaCl, 10 mM $MgCl_2$, 5% glycerol, 0.5 mM TCEP. RIT1 containing fractions were pooled, concentrated and frozen in liquid nitrogen. The entire purification scheme was carried out at 4°C. Recombinant $p31^{comet}$ WT and ΔN protein were expressed and purified analogously but with the use of 50 mM Tris-HCl (pH 8.0) buffer without $MgCl_2$.

Recombinant MAD2 WT and RQ were expressed from pDEST527 (Addgene, plasmid #11518) containing an N-terminal hexahistidine-tag in BL21(DE3) following the same conditions described above in 50 mM Tris-HCl (pH 8.0) buffer without $MgCl_2$. After subtractive purification, TEV-cleaved MAD2 protein was dialyzed overnight in anion-exchange (AE) buffer (10 mM Tris-HCl (pH 8.0), 30 mM NaCl, 5% glycerol and 1 mM DTT). MAD2 was loaded onto an AE Resource-Q column (Cytiva Life Sciences) equilibrated in AE Buffer. The protein was eluted using a NaCl gradient, concentrated and flash-frozen in liquid nitrogen.

Recombinant GST-tagged proteins were expressed from a pGEX-6 plasmid transformed into BL21 (DE3) cells. Expression was induced with 0.2 mM IPTG for 14-16 h at 18°C. Cells were lysed by sonication in 50 mM Tris-HCl (pH 8.0), 300 mM NaCl, 5% glycerol, 1 mM DTT. Proteins were immobilized on Glutathione sepharose 4B beads (Cytiva Life Sciences), washed extensively, and stored as a 50% glycerol bead suspension at -20°C.

Immunoprecipitation and GST pulldown assays

GST pulldown assays with recombinant proteins were performed by diluting indicated proteins in 500 µl of pulldown buffer (10 mM Tris-HCl (pH 8.0), 150 mM NaCl, 0.1% IGEPAL CA-630, 10%

glycerol) and 20 µl of Glutathione sepharose 4B beads (Cytiva Life Sciences) for 1 h at 4°C with end over end rotation. Beads were rinsed three times with pulldown buffer and resuspended in LDS sample buffer (Life Science Technologies) for immunoblot or Coomassie staining of SDS-PAGE gels. For nucleotide loading, RIT1 was incubated in 100 µl GTPase loading buffer (20 mM Tris 7.5, 25 mM NaCl, 5 mM EDTA) containing 2 mM GTP or GTPγS, for 30 min at 30°C. Samples were chilled on ice and $MgCl_2$ was added to a final concentration of 10 mM. RGL3-RBD was used as a positive control for nucleotide loading due to the GTP-dependent interaction between RIT1 and RGL3.(*47*)

For GST pulldown of proteins from cell lysates, 3 x 10^6 HEK-293T cells were transfected with 4 µg total DNA of indicated plasmids. 24 hours after transfection, cells were rinsed with ice-cold PBS and lysed with 1 ml of Lysis buffer (50 mM Tris-HCl (pH 8.0), 150 mM NaCl, 1% IGEPAL CA-630, 10% glycerol) supplemented with protease and phosphatase inhibitor cocktails (Sigma-Aldrich). Lysates were cleared by centrifugation and incubated with 20 µl of Glutathione Sepharose 4B beads for 4 h at 4°C with end-over-end rotation. Beads were rinsed three times with Lysis buffer and resuspended in LDS sample buffer.

For immunoprecipitation of FLAG-RIT1 from cell cycle synchronized HeLa cells, approximately 10^6 cells were rinsed with PBS and harvested using a cell scraper at indicated time points, spun down and frozen. Cells were then lysed with RIPA Buffer (50 mM Tris-HCl (pH 8.0), 150 mM NaCl, 0.5% Deoxycholate, 0.1% SDS, 1% IGEPAL CA-630) supplemented with protease and phosphatase inhibitor cocktails (Sigma-Aldrich), cleared by centrifugation, and incubated with 20 µl anti-FLAG M2 agarose beads (EMD Millipore) for 4 hours at 4°C with end over end rotation. Beads were rinsed three times with RIPA buffer and resuspended in LDS sample buffer.

Cell cycle synchronization

Synchronization of cells at G1/S boundary was performed with a double thymidine block. Briefly, ~50% confluent cells were treated with 2 mM thymidine (Sigma-Aldrich) for 20 h, rinsed twice and

released into drug-free media for 9 h, then treated again with 2 mM thymidine for 18 h. Synchronization of cells in prometaphase was done by addition of 100 ng/ml nocodazole (Selleckchem) 4 h after release from a single-thymidine block and incubated for 10 h. Mitotic cells were collected by mechanical shake off.

Subcellular protein fractionation

For subcellular fractionation of endogenous RIT1, Asynchronous cells were harvested with trypsin-EDTA and then centrifuged at 500 x *g* for 5 min. Nocodazole-arrested mitotic cells were harvested by mitotic shake-off and centrifuged at 500 x *g* for 5 min. Cell pellets were rinsed with ice-cold PBS and transferred to 1.5 ml tubes and pelleted by centrifugation at 500 x *g* for 5 min. Cell pellets were then lysed and proteins were fractionated using the Subcellular Protein Fractionation Kit for Cultured Cells (Thermo Scientific) according to manufacturer's instructions.

Liposome Binding Assay

Liposomes were prepared by mixing chloroform solutions of POPC and POPS (70:30) (Avanti Polar Lipids), desiccated under nitrogen gas, and stored in a vacuum overnight. Lipids were then redissolved in TBS (20 mM Tris HCl pH 7.5, 100mM NaCl, 0.02% sodium azide) to a final 1 mM phospholipid concentration and subjected to five freeze-thaw cycles. Lipid suspension was then filtered through a 0.1 µm pore size membrane in a mini-extruder (Avanti Polar Lipids) ten times to generate uniform unilamellar vesicles. For liposome binding assay, 100 µl reactions containing 0.1 µM RIT1 with or without 0.1 µM MAD2 and/or $p31^{comet}$ protein in TBS were incubated on ice for 1 h. Liposomes were then added to each reaction at a final lipid concentration of 100 µM and incubated on ice for an additional 1 h. Liposomes were pelleted by ultracentrifugation (100,000 x *g*) for 30 min. Pellets were dissolved in 1x LDS and analyzed by Western blot.

Size Exclusion Chromatography

Equal molar ratios of indicated proteins were incubated at 10 μM final concentration in PBS (pH 7.4), 0.5 mM TCEP for 1 hour at 25°C. Samples were chilled on ice and centrifuged (15,000 rpm) to remove any precipitates before loading onto a Superdex 200 3.2/300 column equilibrated in PBS (pH 7.4), 0.5 mM TCEP. All samples were eluted under isocratic conditions at 4°C with a flow rate of 0.035 ml min^{-1}. Elution profiles were monitored at 280nm. Elution fractions were separated by SDS-PAGE and stained with Coomassie. Consistent with previous reports, we observed spontaneous dimerization of bacterially expressed MAD2 (see figure 2.5D).(*36*, *48*)

Immunofluorescence and Metaphase spreads

For immunofluorescence microscopy, cells were grown of #1.5 coverslips, rinsed with PBS, and fixed with 4% paraformaldehyde in PBS for 10 min at room temperature. Permeabilization was performed with 0.1% Triton X-100 for 10 min at room temperature (RT) and blocked with blocking buffer (3% BSA in 0.1 % PBS-Tween 20) for 1 h or overnight at 4C. Primary and secondary antibodies were diluted in blocking buffer. Cells were incubated with primary antibody for 1 h at RT, rinsed 3x with PBS-T, then incubated with secondary antibody for 1 h at RT. Cells were counterstained with DAPI (Sigma Aldrich) and mounted with Fluoromount-G (Invitrogen). The following antibodies were used: FLAG (F1804; 1:1000) and Closed-MAD2 (Jakob Nilsson, University of Copenhagen; 1:50), Alexa Fluor 488, and Alexa Fluor 647 (Life Technologies, 1:2,000), CREST-FITC (Antibodies Inc.; 1:50). For subcellular localization of FLAG-RIT1, images were acquired on an inverted Nikon Ti microscope equipped with a CSU-22 spinning disk confocal, EMCCD camera. Images were processed in Fiji.(*49*) For MAD2 kinetochore intensity experiments, images were acquired on a GE OMX-SR microscope (inverted) equipped with three PCO 15bit CMOS cameras and a Plan ApoN 60X/1.42 oil objective. Deconvolved z-stack images were processed and quantified in Fiji. MAD2 mean fluorescence at kinetochores was normalized to CREST mean fluorescence signal.

For analysis of mitotic errors (chromosome segregation errors), HCT-116 cells were grown on #1.5 coverslips, rinsed with PBS, and fixed with 100% methanol. Coverslips were quickly hydrated and mounted with Prolong Gold Antifade mounting media with DAPI (Invitrogen). Cells were imaged on a Zeiss AxioImager M1 fluorescent microscope equipped with a 40x/0.75 Plan-Neofluar objective (Zeiss) and controlled with ZEN imaging software (Zeiss). For each biological replicate, at least 60 anaphase cells were analyzed per condition.

For metaphase chromosome spread analysis, cells were treated with 0.1 µg/ml Colcemid (Thermo Fisher Scientific) for 2 h, trypsinized and spun down. Cell pellets were gently resuspended in 2 ml hypotonic solution (75 mM KCl) added dropwise while mixing cell suspension, followed by 15 min incubation at 37°C. Cells were spun down again and resuspended in 5 ml of Carnoy's fixative (3:1, methanol:glacial acetic acid, made fresh) added dropwise to cells. Cells were allowed to fix at room temperature for 20 min, then centrifuged and rinsed twice with Carnoy's fixative. Cells were dropped onto clean coverslips and rinsed with fixative to remove debris. Coverslips were placed in a humidity chamber for 10 min, then allowed to air dry for 24-72 h. Chromosome spreads were mounted with ProLong Gold Antifade mounting medium with DAPI (Thermo Fisher Scientific) and imaged on a Zeiss AxioImager M1 fluorescent microscope equipped with a 63x/1.25 Plan-Neofluar oil objective (Zeiss). Images of at least 75 chromosome spreads were captured per condition and experimenter blinded before being quantified using Fiji.(*49*)

Live cell imaging

For mitotic duration experiments, cells were engineered to stably express Histone H2B-mCherry (pLenti6-H2B-mCherry, Addgene, plasmid #89766), and seeded onto 12-well #1.5 glass bottom plates (Cellvis). Drug treatments were performed 1 h before imaging. Time-lapse images were captured on a Nikon Ti-E inverted wide-field fluorescent microscope equipped with a 20x/0.75 Plan Apo air objective (Nikon). Cells treated with nocodazole were imaged at 5 min intervals, otherwise cells were imaged at 2 min, for 20 hours. The microscope was equipped with an

incubation chamber (Okolab), providing a humidified atmosphere at 37 °C with 5% CO2. Mitotic length was quantified as the duration between nuclear disassembly and anaphase onset. Mitotic error rates in hTERT-RPE1 cells were determined from live-cell images used to assess mitotic length. Images were analyzed using Fiji.

For RIT1 subcellular localization experiments, hTERT-RPE1 cells stably expressing Histone H2B-mCherry and mNeonGreen (mNG)-RIT1 were seeded on seeded onto 12-well #1.5 glass bottom plates and allowed to adhere for 24-48 h. Prior to imaging, cells were exchanged into imaging media: FluoroBrite DMEM (Thermo Fisher Scientific) supplemented with 10% FBS and 4 mM GlutaMAX (Thermo Fisher Scientific). Images were acquired as a series of 0.9 µm z-stacks with a Plan Apo 40x/0.95 Corr (DIC N2 / 40X I) 227.5 nm/pixel objective (Nikon) at 5 min intervals on a Nikon Ti-E inverted CSU-22 spinning disk confocal microscope equipped with an incubation chamber (Okolab), providing a humidified atmosphere at 37 °C with 5% CO2. Images were analyzed using Fiji. For quantitative analysis, a single central plane along the z-axis was used. For PM/Cyto. ratio calculations, semi-automated recognition of the cell boundary within the Fiji program was used to create regions of interests designating the plasma membrane and cytoplasm, and mean fluorescence intensity was calculated within each region.

For Cyclin B1 degradation assays, hTERT-RPE1 and HeLa cells stably expressing low levels of mNG-Cyclin B1 under the transcriptional control of a Ubiquitin C promoter and Histone H2B-mCherry were seeded onto chambered coverslips (Ibidi) and imaged similarly to the RIT1 subcellular localization experiments described above with the following exceptions: images of unperturbed mitosis were captured at 2 min intervals and images of cells treated with nocodazole at 6 min intervals. For quantitative analysis, a single central plane along the z-axis was used. mNG mean fluorescence intensity was normalized to NEBD.

Kinase Assays

For phosphorylation of RIT1 using mitotic cell extract, metaphase arrested HEK-293T cells were harvested, rinsed with PBS, and lysed with 4x pellet volume of Lysis buffer (50 mM Tris-HCl (pH 8.0), 150 mM NaCl, 1% IGEPAL CA-630, 10% glycerol) supplemented with 10 μM MG132 (Sigma-Aldrich) protease and phosphatase inhibitor cocktails (Sigma-Aldrich). The lysate was cleared by centrifugation for 10 min at 15,000 rpm. 1 ml of cleared lysate was incubated with indicated drugs (10 μM final concentration) or DMSO for 30 min at 4°C. No lysate control consisted of 1 ml Lysis buffer. Bacteria purified GST-RIT1 or GST protein bound to sepharose beads was added to lysates at 0.5 μM final concentration, together with 10 mM $MgCl_2$ and 0.1 mM ATP. Reactions were incubated at 30°C for 1 h with end over end rotation. Tubes were chilled on ice for 5 min, beads were then centrifuged and rinsed three times with RIPA buffer and resuspended in LDS sample buffer.

CDK1/Cyclin B1 kinase assays were conducted using recombinant active CDK1/Cyclin B1 purchased from SignalChem (C22-10G). 20 μl reactions containing 200 ng CDK1/Cyclin B1 protein and 3 μg of RIT1 protein diluted in Kinase assay buffer (5 mM MOPS, pH7.2, 2.5 mM β-glycerol-phosphate, 10 mM $MgCl_2$, 1 mM EGTA, 0.4 mM EDTA, 50 ng/μl BSA) with or without 3mM ATP were incubated at 30°C for 1 h. Reactions were stopped by addition of LDS sample buffer for SDS-PAGE or flash-frozen in liquid nitrogen for mass spectrometry analysis.

Mass Spectrometry

For identification of RIT1 binding partners, approximately 2 x 10^7 HEK-293T cells were transiently transfected with 8 μg of plasmid (FLAG-RIT1 or EV control) and immunoprecipitated as described above with buffer containing 50 mM Tris-HCl (pH 8.0), 150 mM NaCl, 1% IGEPAL CA-630, 10% glycerol and supplemented with protease and phosphatase inhibitor cocktails (Sigma-Aldrich). Magnetized beads were washed with ice-cold 20 mM Tris-HCl (pH 8.0), 2 mM $CaCl_2$ buffer and frozen prior to trypsin digest.

Protein pulldown samples were on-bead digested with trypsin as previously described.(*7*) Briefly, the beads were resuspended in 9 µL of 20 mM Tris-HCl pH 8.0. The proteins were reduced with DTT, 5 mM final concentration, at room temperature for 30 min; alkylated with iodoacetamide, 15 mM final concentration, at room temperature for 10 min; and digested with 500 ng of trypsin (Sigma Trypsin Singles, T7575) at 37°C overnight. In vitro kinase assay samples, 20 µL each, were digested using the same protocol. All samples were desalted with ZipTip u-C18 pipette tips (Millipore), vacuum dried, and reconstituted in 15 µL of 0.1% formic acid for analysis by LC-MS/MS.

LC-MS/MS was carried out on Acquity UPLC M-Class system (Waters) online with Orbitrap Fusion Lumos Tribrid Mass Spectrometer (Thermo Fisher Scientific). Reversed-phase chromatography was performed on a 15 cm silica-C18 EasySpray column (Thermo Fisher Scientific) at 45°C with a binary buffer system (Buffer A = 0.1% formic acid in water; Buffer B = 0.1% formic acid in acetonitrile) and a flow rate of 400 nL/min. The sample was loaded at 2% B for 20 min followed by a 2-60% B gradient over 60 min, followed by a brief wash at 80% B and equilibration at 2% B. The mass spectrometer was operated in Full-MS/ddMS2 mode with one survey scan (375-1500 m/z, R=120,000, AGC target of 4e5), followed by a series of data-dependent HCD MS2 scans not to exceed a 3 sec cycle (AGC target of 5e4, max IT 100 ms, R=30,000, isolation window 1.6 m/z, NCE 30%, stepped collision 5%, and 30 s dynamic exclusion).

MS raw data files were converted to peak list files using Proteome Discoverer v. 1.4 (Thermo Fisher Scientific) and searched using Protein Prospector(*50*, *51*) (version 6.0.0) against human SwissProt database(*52*) downloaded on 01/08/2018 (or a subset of this database with RIT1, CDK1 and CCNB1 entries only when searching in vitro kinase assay samples) and a corresponding random concatenated decoy database. Other settings included the default “ESI-Q-high-res” parameters with trypsin as the protease, up to two allowed missed cleavage sites, Carbamidomethyl-C as a constant modification, default variable modifications for pulldown

samples (or default variable modifications plus phosphorylation at STY for in vitro kinase assay samples), up to 3 modifications per peptide, and 5 ppm precursor mass and 15 ppm fragment mass tolerance. False discovery rate of <1% was used as the cutoff for peptide expectation values. Protein Prospector search results were exported in BiblioSpec format compatible with downstream analysis in Skyline.(*53*) Quantitation of peptide and protein abundances was carried out in Skyline v20 by quantifying MS1 precursor peak areas with normalization by median centering.(*54*) Peptides shared by multiple proteins in the database were excluded.

APC/C Ubiquitination Assay

Detection of APC/C activity using mitotic checkpoint active cell extracts was previously described.(*55*) HeLa RIT1 KO cells arrested in prometaphase were harvested, rinsed with ice-cold PBS, and resuspended in 75% pellet volume of hypotonic buffer (20 mM HEPES, pH 7.6, 5 mM KCl, 1 mM DTT) containing protease inhibitor cocktail (Roche). Cells were lysed with multiple rounds of freeze-thawing and were cleared by centrifugation at 13,000 rpm for 1 h at 4°C. Cleared lysate was supplemented with glycerol to 10% (v/v), aliquoted and frozen in liquid nitrogen. The protein concentration of cell extract was ~20 mg/ml. APC/C activity reactions were carried in samples containing 50% (v/v) mitotic cell extract diluted in buffer with final concentrations of the following: 10 mM Tris-HCl, pH 7.6, 5 mM $MgCl_2$, 1 mM DTT, 1 mg/ml Ubiquitin (Boston Biochem; U-100H), 10 mM phosphocreatine, 0.5 mM ATP, 10 µg/ml UbcH10 (Boston Biochem; E2-650), and 50 µg/ml Creatine phosphokinase (Sigma-Aldrich). Recombinant RIT1 protein was buffer exchanged into assay buffer containing 20 mM HEPES pH 7.4, 300 mM NaCl, 1 mM TCEP, 5% glycerol before being added to samples. Control conditions received equal volumes of assay buffer. Samples were incubated on ice for 1 h, then transferred to 30°C. 4 µl samples were withdrawn at indicated times and rapidly quenched with LDS sample buffer. Degradation of Cyclin B1 and Securin was followed by immunoblotting and was normalized to MAD2 protein levels. Densitometry analysis was performed using Fiji.

Quantification and statistical analysis

Statistical analysis was performed using GraphPad Prism 7.0 (GraphPad). Results are expressed as mean ± s.d. For each mitotic length scatterplot, the horizontal line represents the mean. For kinetochore MAD2 fluorescence intensity scatterplots, the horizontal line and error bars represents the median and 95% confidence interval, respectively. No statistical methods were used to predetermine the sample size. Experiments analyzed by immunoblotting were repeated 2-4 times with similar results. For chromosome spread analysis, investigators were blinded to sample allocation.

Acknowledgements

We thank Dom Esposito and Vanessa Wall (Frederick National Lab) for the multisite gateway plasmid toolkit and members of the McCormick lab for their input. We thank Alice Berger and Athea Vichas (Fred Hutch Cancer Center) for kindly sharing unpublished data and Jakob Nilsson (University of Copenhagen) for C-MAD2 antibody. Data for this study were acquired at the Nikon Imaging Center at UCSF. This work was supported by a grant from the NCI (R35CA197709 to F.M.). ACN is a fellow of the NSF Graduate Research Fellowship Program (1650113). P.C. work is supported by the NCI (K99CA245122). We thank the UCSF Mass Spectrometry Facility and A. L. Burlingame for providing MS instrumentation support for this project (funded by the NIH grants P41GM103481 and S10OD016229).

References

1. A. H. Berger, M. Imielinski, F. Duke, J. Wala, N. Kaplan, G.-X. Shi, D. A. Andres, M. Meyerson, Oncogenic RIT1 mutations in lung adenocarcinoma. *Oncogene*. **33**, 4418–4423 (2014).

2. Y. Aoki, T. Niihori, T. Banjo, N. Okamoto, S. Mizuno, K. Kurosawa, T. Ogata, F. Takada, M. Yano, T. Ando, T. Hoshika, C. Barnett, H. Ohashi, H. Kawame, T. Hasegawa, T. Okutani, T. Nagashima, S. Hasegawa, R. Funayama, T. Nagashima, K. Nakayama, S.-I. Inoue, Y. Watanabe, T. Ogura, Y. Matsubara, Gain-of-function mutations in RIT1 cause Noonan syndrome, a RAS/MAPK pathway syndrome. *Am. J. Hum. Genet.* **93**, 173–180 (2013).

3. M. Yaoita, T. Niihori, S. Mizuno, N. Okamoto, S. Hayashi, A. Watanabe, M. Yokozawa, H. Suzumura, A. Nakahara, Y. Nakano, T. Hokosaki, A. Ohmori, H. Sawada, O. Migita, A. Mima, P. Lapunzina, F. Santos-Simarro, S. García-Miñaúr, T. Ogata, H. Kawame, K. Kurosawa, H. Ohashi, S.-I. Inoue, Y. Matsubara, S. Kure, Y. Aoki, Spectrum of mutations and genotype-phenotype analysis in Noonan syndrome patients with RIT1 mutations. *Hum. Genet.* **135**, 209–222 (2016).

4. D. K. Simanshu, D. V. Nissley, F. McCormick, RAS Proteins and Their Regulators in Human Disease. *Cell*. **170**, 17–33 (2017).

5. R. Van, A. Cuevas-Navarro, P. Castel, F. McCormick, The molecular functions of RIT1 and its contribution to human disease. *Biochemical Journal*. **477**, 2755–2770 (2020).

6. P. Rodriguez-Viciana, C. Sabatier, F. McCormick, Signaling specificity by Ras family GTPases is determined by the full spectrum of effectors they regulate. *Mol. Cell. Biol.* **24**, 4943–4954 (2004).

7. P. Castel, A. Cheng, A. Cuevas-Navarro, D. B. Everman, A. G. Papageorge, D. K. Simanshu, A. Tankka, J. Galeas, A. Urisman, F. McCormick, RIT1 oncoproteins escape LZTR1-mediated proteolysis. *Science*. **363**, 1226–1230 (2019).

8. A. Musacchio, The Molecular Biology of Spindle Assembly Checkpoint Signaling Dynamics. *Curr. Biol.* **25**, R1002-1018 (2015).

9. R. S. Hagan, M. S. Manak, H. K. Buch, M. G. Meier, P. Meraldi, J. V. Shah, P. K. Sorger, p31(comet) acts to ensure timely spindle checkpoint silencing subsequent to kinetochore attachment. *Mol. Biol. Cell*. **22**, 4236–4246 (2011).

10. G. Xia, X. Luo, T. Habu, J. Rizo, T. Matsumoto, H. Yu, Conformation-specific binding of p31(comet) antagonizes the function of Mad2 in the spindle checkpoint. *EMBO J.* **23**, 3133–3143 (2004).

11. L. Wang, J. Zhang, L. Wan, X. Zhou, Z. Wang, W. Wei, Targeting Cdc20 as a novel cancer therapeutic strategy. *Pharmacol Ther*. **151**, 141–151 (2015).

12. F. G. Westhorpe, A. Tighe, P. Lara-Gonzalez, S. S. Taylor, p31comet-mediated extraction of Mad2 from the MCC promotes efficient mitotic exit. *J. Cell. Sci.* **124**, 3905–3916 (2011).

13. E. Eytan, K. Wang, S. Miniowitz-Shemtov, D. Sitry-Shevah, S. Kaisari, T. J. Yen, S.-T. Liu, A. Hershko, Disassembly of mitotic checkpoint complexes by the joint action of the AAA-ATPase TRIP13 and p31comet. *Proceedings of the National Academy of Sciences*. **111**, 12019–12024 (2014).

14. T. Habu, S. H. Kim, J. Weinstein, T. Matsumoto, Identification of a MAD2-binding protein, CMT2, and its role in mitosis. *EMBO J.* **21**, 6419–6428 (2002).

15. M. Mapelli, L. Massimiliano, S. Santaguida, A. Musacchio, The Mad2 conformational dimer: structure and implications for the spindle assembly checkpoint. *Cell*. **131**, 730–743 (2007).

16. M. Yang, B. Li, D. R. Tomchick, M. Machius, J. Rizo, H. Yu, X. Luo, p31comet blocks Mad2 activation through structural mimicry. *Cell*. **131**, 744–755 (2007).

17. M. Mapelli, F. V. Filipp, G. Rancati, L. Massimiliano, L. Nezi, G. Stier, R. S. Hagan, S. Confalonieri, S. Piatti, M. Sattler, A. Musacchio, Determinants of conformational dimerization of Mad2 and its inhibition by p31comet. *EMBO J.* **25**, 1273–1284 (2006).

18. C. H. Lee, N. G. Della, C. E. Chew, D. J. Zack, Rin, a neuron-specific and calmodulin-binding small G-protein, and Rit define a novel subfamily of ras proteins. *J. Neurosci.* **16**, 6784–6794 (1996).

19. W. D. Heo, T. Inoue, W. S. Park, M. L. Kim, B. O. Park, T. J. Wandless, T. Meyer, PI(3,4,5)P3 and PI(4,5)P2 lipids target proteins with polybasic clusters to the plasma membrane. *Science*. **314**, 1458–1461 (2006).

20. F. L. Hall, P. R. Vulliet, Proline-directed protein phosphorylation and cell cycle regulation. *Curr. Opin. Cell Biol.* **3**, 176–184 (1991).

21. A. Lindqvist, V. Rodríguez-Bravo, R. H. Medema, The decision to enter mitosis: feedback and redundancy in the mitotic entry network. *J. Cell Biol.* **185**, 193–202 (2009).

22. S. Santaguida, A. Tighe, A. M. D'Alise, S. S. Taylor, A. Musacchio, Dissecting the role of MPS1 in chromosome biorientation and the spindle checkpoint through the small molecule inhibitor reversine. *J. Cell Biol.* **190**, 73–87 (2010).

23. M. Dobles, V. Liberal, M. L. Scott, R. Benezra, P. K. Sorger, Chromosome missegregation and apoptosis in mice lacking the mitotic checkpoint protein Mad2. *Cell*. **101**, 635–645 (2000).

24. S. Hanks, K. Coleman, S. Reid, A. Plaja, H. Firth, D. Fitzpatrick, A. Kidd, K. Méhes, R. Nash, N. Robin, N. Shannon, J. Tolmie, J. Swansbury, A. Irrthum, J. Douglas, N. Rahman, Constitutional aneuploidy and cancer predisposition caused by biallelic mutations in BUB1B. *Nat. Genet.* **36**, 1159–1161 (2004).

25. Y. Iwanaga, Y.-H. Chi, A. Miyazato, S. Sheleg, K. Haller, J.-M. Peloponese, Y. Li, J. M. Ward, R. Benezra, K.-T. Jeang, Heterozygous deletion of mitotic arrest-deficient protein 1 (MAD1) increases the incidence of tumors in mice. *Cancer Res.* **67**, 160–166 (2007).

26. M. Li, X. Fang, Z. Wei, J. P. York, P. Zhang, Loss of spindle assembly checkpoint-mediated inhibition of Cdc20 promotes tumorigenesis in mice. *J. Cell Biol.* **185**, 983–994 (2009).

27. L. S. Michel, V. Liberal, A. Chatterjee, R. Kirchwegger, B. Pasche, W. Gerald, M. Dobles, P. K. Sorger, V. V. Murty, R. Benezra, MAD2 haplo-insufficiency causes premature anaphase and chromosome instability in mammalian cells. *Nature*. **409**, 355–359 (2001).

28. C. Lengauer, K. W. Kinzler, B. Vogelstein, Genetic instability in colorectal cancers. *Nature*. **386**, 623–627 (1997).

29. A. DeAntoni, V. Sala, A. Musacchio, Explaining the oligomerization properties of the spindle assembly checkpoint protein Mad2. *Philos. Trans. R. Soc. Lond., B, Biol. Sci.* **360**, 637–647, discussion 447-448 (2005).

30. L. Sironi, M. Mapelli, S. Knapp, A. De Antoni, K.-T. Jeang, A. Musacchio, Crystal structure of the tetrameric Mad1-Mad2 core complex: implications of a “safety belt” binding mechanism for the spindle checkpoint. *EMBO J.* **21**, 2496–2506 (2002).

31. M. Hara, E. Özkan, H. Sun, H. Yu, X. Luo, Structure of an intermediate conformer of the spindle checkpoint protein Mad2. *Proc. Natl. Acad. Sci. U.S.A.* **112**, 11252–11257 (2015).

32. X. Luo, Z. Tang, J. Rizo, H. Yu, The Mad2 spindle checkpoint protein undergoes similar major conformational changes upon binding to either Mad1 or Cdc20. *Mol. Cell*. **9**, 59–71 (2002).

33. G. Mondal, R. N. Baral, S. Roychoudhury, A new Mad2-interacting domain of Cdc20 is critical for the function of Mad2-Cdc20 complex in the spindle assembly checkpoint. *Biochem. J.* **396**, 243–253 (2006).

34. S. Kim, H. Sun, H. L. Ball, K. Wassmann, X. Luo, H. Yu, Phosphorylation of the spindle checkpoint protein Mad2 regulates its conformational transition. *Proc. Natl. Acad. Sci. U.S.A.* **107**, 19772–19777 (2010).

35. X. Luo, G. Fang, M. Coldiron, Y. Lin, H. Yu, M. W. Kirschner, G. Wagner, Structure of the Mad2 spindle assembly checkpoint protein and its interaction with Cdc20. *Nat. Struct. Biol.* **7**, 224–229 (2000).

36. L. Sironi, M. Melixetian, M. Faretta, E. Prosperini, K. Helin, A. Musacchio, Mad2 binding to Mad1 and Cdc20, rather than oligomerization, is required for the spindle checkpoint. *EMBO J.* **20**, 6371–6382 (2001).

37. K. Wang, B. Sturt-Gillespie, J. C. Hittle, D. Macdonald, G. K. Chan, T. J. Yen, S.-T. Liu, Thyroid Hormone Receptor Interacting Protein 13 (TRIP13) AAA-ATPase Is a Novel Mitotic Checkpoint-silencing Protein. *J. Biol. Chem.* **289**, 23928–23937 (2014).

38. I. Primorac, A. Musacchio, Panta rhei: the APC/C at steady state. *J. Cell Biol.* **201**, 177–189 (2013).

39. L. Chang, D. Barford, Insights into the anaphase-promoting complex: a molecular machine that regulates mitosis. *Curr. Opin. Struct. Biol.* **29**, 1–9 (2014).

40. H. Hochegger, S. Takeda, T. Hunt, Cyclin-dependent kinases and cell-cycle transitions: does one fit all? *Nat Rev Mol Cell Biol*. **9**, 910–916 (2008).

41. S. R. Hingorani, L. Wang, A. S. Multani, C. Combs, T. B. Deramaudt, R. H. Hruban, A. K. Rustgi, S. Chang, D. A. Tuveson, Trp53R172H and KrasG12D cooperate to promote chromosomal instability and widely metastatic pancreatic ductal adenocarcinoma in mice. *Cancer Cell*. **7**, 469–483 (2005).

42. T. Kamata, C. Pritchard, Mechanisms of aneuploidy induction by RAS and RAF oncogenes. *Am J Cancer Res*. **1**, 955–971 (2011).

43. G. Yang, I. Mercado-Uribe, A. S. Multani, S. Sen, I.-M. Shih, K.-K. Wong, D. M. Gershenson, J. Liu, RAS promotes tumorigenesis through genomic instability induced by imbalanced expression of Aurora-A and BRCA2 in midbody during cytokinesis. *Int. J. Cancer*. **133**, 275–285 (2013).

44. C. L. Farnsworth, L. A. Feig, Dominant inhibitory mutations in the Mg(2+)-binding site of RasH prevent its activation by GTP. *Mol. Cell. Biol.* **11**, 4822 (1991).

45. M. Frech, T. A. Darden, L. G. Pedersen, C. K. Foley, P. S. Charifson, M. W. Anderson, A. Wittinghofer, Role of glutamine-61 in the hydrolysis of GTP by p21H-ras: an experimental and theoretical study. *Biochemistry*. **33**, 3237–3244 (1994).

46. V. E. Wall, L. A. Garvey, J. L. Mehalko, L. V. Procter, D. Esposito, Combinatorial assembly of clone libraries using site-specific recombination. *Methods Mol. Biol.* **1116**, 193–208 (2014).

47. H. Shao, D. A. Andres, A novel RalGEF-like protein, RGL3, as a candidate effector for rit and Ras. *J. Biol. Chem.* **275**, 26914–26924 (2000).

48. G. Fang, H. Yu, M. W. Kirschner, The checkpoint protein MAD2 and the mitotic regulator CDC20 form a ternary complex with the anaphase-promoting complex to control anaphase initiation. *Genes Dev.* **12**, 1871–1883 (1998).

49. J. Schindelin, I. Arganda-Carreras, E. Frise, V. Kaynig, M. Longair, T. Pietzsch, S. Preibisch, C. Rueden, S. Saalfeld, B. Schmid, J.-Y. Tinevez, D. J. White, V. Hartenstein, K. Eliceiri, P. Tomancak, A. Cardona, Fiji: an open-source platform for biological-image analysis. *Nat. Methods*. **9**, 676–682 (2012).

50. P. R. Baker, J. C. Trinidad, R. J. Chalkley, *Mol. Cell Proteomics*, in press, doi:10.1074/mcp.M111.008078.

51. R. J. Chalkley, P. R. Baker, Use of a glycosylation site database to improve glycopeptide identification from complex mixtures. *Anal Bioanal Chem*. **409**, 571–577 (2017).

52. UniProt Consortium, UniProt: a worldwide hub of protein knowledge. *Nucleic Acids Res.* **47**, D506–D515 (2019).

53. L. K. Pino, B. C. Searle, J. G. Bollinger, B. Nunn, B. MacLean, M. J. MacCoss, The Skyline ecosystem: Informatics for quantitative mass spectrometry proteomics. *Mass Spectrom Rev*. **39**, 229–244 (2020).

54. B. Schilling, M. J. Rardin, B. X. MacLean, A. M. Zawadzka, B. E. Frewen, M. P. Cusack, D. J. Sorensen, M. S. Bereman, E. Jing, C. C. Wu, E. Verdin, C. R. Kahn, M. J. Maccoss, B. W. Gibson, Platform-independent and label-free quantitation of proteomic data using MS1 extracted ion chromatograms in skyline: application to protein acetylation and phosphorylation. *Mol. Cell Proteomics*. **11**, 202–214 (2012).

55. I. Braunstein, S. Miniowitz, Y. Moshe, A. Hershko, Inhibitory factors associated with anaphase-promoting complex/cylosome in mitotic checkpoint. *Proc. Natl. Acad. Sci. U.S.A.* **104**, 4870–4875 (2007).

Chapter 3 : Ras-dependent MAPK hyperactivation by pathogenic RIT1 is a therapeutic target in myocardial hypertrophy

Over the past decade, gain-of-function mutations in *RIT1* have emerged as a common genetic driver of Noonan syndrome (NS), a genetic disorder characterized by craniofacial dysmorphism, shortened stature, and congenital heart defects (*1–4*). Like other RASopathies, NS is driven by mutations that hyperactivate the RAF-MEK-ERK mitogen-activated protein kinase (MAPK) cascade. Pathogenic RIT1 mutations evade proteasomal degradation and accumulate in the cell, resulting in an upregulation of MAPK signaling (*5*). However, the mechanism by which RIT1 activates the MAPK pathway is not well understood. Here, we employed biophysical, biochemical, and cell biological approaches to interrogate RIT1 activation of RAF kinases. We show that different biochemical properties of the RIT1 HVR contribute to its association with the PM and enable RAF binding. RIT1 exhibits preferential binding to RAF1 (also known as CRAF) and engages with an overlapping set of RBD residues associated with Ras-binding, albeit with a weaker affinity. Furthermore, the absence of Ras limits the ability of RIT1 oncoproteins to hyperactivate the MAPK pathway and pharmacological MAPK inhibition ameliorates cardiac tissue overgrowth associated with aberrant RIT1 signaling.

RIT1 association with the PM requires charge complementarity

Unlike classical Ras proteins, the RIT1 HVR lacks prenylation motifs, indicating that the protein engages with the PM in a unique way. To investigate this interaction, we used surface plasmon resonance (SPR) to measure the association of RIT1 with liposomes of various charge ratios (**Fig 3.1A**). RIT1 showed no binding response to neutral liposomes, however as the negative charge in the liposome was increased via the inclusion of 16:0-18:1 phosphatidylserine (POPS), the binding response increased (**Fig 3.1B**). We confirmed this interaction was strictly mediated by the HVR because upon its removal we did not observe interaction with liposomes

containing 30% POPS (**Fig 3.7A**). The association of RIT1 with anionic lipid-containing liposomes was quantitated by calculating the partition coefficient (*6*)(**Fig 3.7B**). Increasing the concentration of POPS in the liposomes from 10 to 30% increased the partition coefficient by 40-fold. Consistent with our data, molecular dynamic simulations have found that the RIT1 HVR experiences a significantly longer residence time on POPS-containing bilayers compared to uncharged bilayers (*7*).

The RIT1 HVR has an isoelectric point of 10.6 and contains three polybasic regions (PBR) separated by non-charged amino acids (**Fig 3.1C**). To better characterize the contribution of these PBRs, we assessed the PM association of fluorescently labeled RIT1 with individual PBRs that had their charge neutralized (R/K→A) or reversed (R/K→E) (**Fig 3.1D**). As expected, charge reversal and neutralization of PBR1, PBR3, and to a lesser degree PBR2, disrupted the typical distribution of RIT1 at the cellular periphery, suggesting that all three PBRs are essential for membrane association in cells. PBR2 contains fewer basic residues than PBR1 and PBR3 and, thus, the contribution to membrane association provided by each PBR may be directly correlated to their overall charge contribution. In addition, charge neutralization of a single basic residue within PBR2 or PBR3 (R206 and R212, respectively) was insufficient to disrupt membrane association (**Fig 3.7C**). Using a GFP-RIT1 C-terminal peptide fusion construct, Heo *et al.,* (2006) demonstrated that hydrophobic sidechains of the RIT1 HVR may also regulate RIT1-PM association (*8*). Therefore, we individually mutated five hydrophobic HVR residues in a full-length RIT1 construct. Of these, alanine substitution of the three largest side chains disrupted PM targeting (**Fig 3.1E, 3.1F, and Fig 3.7C**). Collectively, these data indicate that charge complementarity plays a significant role in the association of RIT1 with the inner leaflet of the PM and that this interaction receives a contribution from the hydrophobic residues interspersed between the PBRs.

Characterization of RIT1-RAF interactions

The HVRs of classical Ras proteins contribute to distinct binding preferences with the different RAF family members: RAF1, ARAF, and BRAF (*9*). Given RIT1's unique HVR, we sought to determine whether RIT1 also exhibits preferential RAF isoform binding. Notably, binding of the three RAF isoforms to wild-type (WT) RIT1 was nearly undetectable in pulldown assays and was markedly weaker than their affinity to KRAS4B (**Fig 3.2A**). However, in contrast to prior observations (*10*), a significant preference for RAF1 was observed when using the pathogenic RIT1 A57G variant. Thus, to better assess these interactions, we developed a quantitative bioluminescence resonance energy transfer (BRET) assay to quantitate the association of RIT1 with RAF kinases in cells (**Fig 3.8A, B**). WT RIT1 had higher $BRET_{max}$ and lower $BRET_{50}$ values for RAF1 compared to BRAF and ARAF, indicating a preference for the RAF1 paralog in intact cells (**Fig 3.2B and 3.8C)**. Based on the calculated $BRET_{50}$ values, RIT1 binds preferentially to RAF1 over BRAF and ARAF. Remarkably, RIT1 A57G bound to RAF1 around 10-fold tighter than WT RIT1 and showed the same binding preferences as the WT protein: RAF1>BRAF>ARAF. To investigate this interaction further we used isothermal titration calorimetry (ITC) to measure the binding affinity between recombinant RAF1- or BRAF-RBD and WT RIT1 or A57G RIT1 bound to GMPPNP, a non-hydrolyzable GTP analog (**Fig 3.2C**). In these experiments, RIT1 A57G (K_D = 2.96 μM) bound approximately 5-times more tightly to RAF1-RBD compared with WT (K_D = 14.55 μM). Consistent with our BRET measurements, RIT1 A57G interaction with BRAF-RBD was weaker than RAF1. However, no measurable binding was observed between WT RIT1 and BRAF, presumably because the binding interaction was below the detection limit for ITC. Cumulatively, these data suggest that RIT1 preferentially interacts with RAF1 over the other RAF isoforms.

To understand how RAF binding differs between RIT1 and RAS, we used solution nuclear magnetic resonance (NMR) spectroscopy to identify broadened and induced chemical shifts upon RBD binding (**Table 3.1**). An overlay of the RAF1 RBD chemical shift perturbation (CSP)

histograms produced by binding to WT RIT1, RIT1 A57G, or KRAS revealed an overlapping set of perturbed residues with minor variations (**Fig 3.3A**). Of note, differences in binding affinities were evident by CSP analysis and were congruent with affinities measured *in vitro* and in cells (**Fig 3.2**); specifically, WT RIT1 induced the smallest perturbation of resonances, followed by RIT1 A57G, then KRAS which induced the largest perturbations. Perturbed residues were then mapped onto modeled structures of WT and A57G mutants of RIT1 in the active state and were compared with the previously solved crystal structure of the KRAS-RAF1(RBD) complex (*11*)(**Fig 3.3B**). This identified the putative RIT1-RBD interface and confirmed a shared binding site on RAF1 RBD. CSP analysis of RIT1 revealed residues (M37, S43, and H44) at the N-terminal end of the switch-I flexible loop, respectively, that were considerably perturbed in the A57G mutant but not in the WT form (**Fig 3.3C, D, Table 3.1**). These data suggest that the switch-I of RIT1 A57G differentially engages RAF1 RBD, potentially providing the enhanced stability exhibited by the pathogenic variant.

To further interrogate how the A57G mutation in RIT1 enhances its interaction with RAF1, we undertook a comparative analysis of the modeled RIT1-RAF1(RBD) structures with that of the solved KRAS-RAF1(RBD) structure (**Fig 3.3E**). The RIT1 A57 residue located at the end of the switch-I region is equivalent to the S39 residue in KRAS (**Fig 3.3F**). In the KRAS-RAF1(RBD) complex structure, sidechain and main-chain atoms of S39 form hydrogen (H-) bonds with R67 and R89 residues of RAF1. KRAS residues D38 and Y40, which surround amino acid S39, form key interactions with RAF1-RBD by forming salt-bridge, H-bond, and van der Waals interaction with RAF1 R89 and T68 residues (*11*). R89L mutation in RAF1 and mutations of S39 neighboring residues (E37G, D38A, and Y40C mutations) in Ras proteins have been shown to result in either complete or significant loss of binding between KRAS and RAF1-RBD (*6*, *11–13*), suggesting the interactions formed by S39 and residues around it in KRAS and R89 in RAF1 play a critical role in KRAS-RAF interaction. Unlike the KRAS S39 residue, the A57 or G57 (A57G) residues in RIT1

cannot form an H-bond with R67 as they lack a side chain hydroxyl group (**Fig 3.3F, G**). Glycine is fundamentally different from Ala and all other amino acids in that it lacks a sidechain, which allows a much larger rotational freedom of its main-chain torsion angles (*14*). In the beta-strand, glycine is often present at N-cap and C-cap positions, and the presence of glycine in the middle of the beta-strand has been shown to have a strong tendency to block β-sheet continuation (*15*). Thus, unlike A57 in WT RIT1, the G57 residue in RIT1 possesses increased rotational space of main-chain torsion angles, imparting flexibility to the local peptide structure. This allows G57 and neighboring residues in switch-I of RIT1 to undergo minor conformational changes that permit higher-affinity interactions with RAF1-RBD, as suggested by the additional perturbation and broadening of RAF1 interface residues R67 and V70, respectively, similar to the conformational changes observed upon KRAS-RAF1(RBD) complex formation (**Fig 3.3F-H, Table 3.1**). Thus, the A57G mutation likely enhances the RIT1-RAF1 interaction through increased flexibility in its main-chain torsion angles, which impact not only G57 but also neighboring residues, including switch-I and flanking residues (S43 and H44) (**Fig 3.3C**). Together, these play a crucial role in forming an enhanced interaction with RAF1-RBD.

RIT1 membrane localization is required for RAF interaction

Ras-RAF(RBD) binding is insufficient for RAF activation in the absence of vicinal PM phospholipids and thus PM anchoring is a requisite for Ras-driven MAPK activation (*16*). Therefore, we reasoned that RIT1-RAF binding and activation may exhibit similar dependency on PM association. To assess the role of RIT1 membrane trafficking on RAF activation, we expressed N-terminal and C-terminal RIT1 deletion mutants and assessed binding by pulldown. As predicted, deletion of the RIT1 C-terminus (192-219), but not its N-terminus (1-18), disrupted membrane association, RAF1 binding, and MAPK activation (**Fig 3.4A and Fig 3.9A**). Importantly, rescuing membrane association of the RIT1 mutant lacking HVR by introducing a CAAX box motif, restored RIT1-RAF1 binding and activation of MAPK, indicating that PM localization is required

for productive RAF interaction. Given the critical function of the HVR in membrane localization, we sought to quantitatively assess how its biochemical properties contribute to RIT1-RAF1 binding *in vivo*. Point mutations that had no impact on membrane localization (**Fig 3.1F and 3.7B**), such as V203, R206A, and R212A, bound RAF1 with a comparable $BRET_{50}$ as WT RIT1 (**Fig 3.4B and 3.4C)**. However, mutations that significantly decreased membrane localization produced much larger $BRET_{50}$ values, indicating a weaker association with RAF1. Interestingly, charge neutralizing mutations in PBR 1 and 3 had the largest impact on RAF1 binding, consistent with their effect on RIT1 PM localization (**Fig 3.1F**). Together, these findings suggest that while the RIT1 HVR does not directly participate in the activation of RAF, it is necessary for RIT1 localization to the PM where it can interact with RAF and activate the MAPK cascade.

Mutant RIT1 activates RAF in a Ras-dependent manner

Although expression of pathogenic RIT1 variants has been widely demonstrated to promote MAPK pathway activation, the mechanism by which RIT1 activates this pathway remains unclear (*3*–*5*, *17*). Given that RIT1 binds RAF directly, one can posit that RIT1, like Ras, may promote MAPK signaling via direct recruitment and activation of RAF at the PM and that the limited degree of activation may be the result of weak RAF binding compared to active RAS (*5*). Intriguingly, despite the increased affinity towards RAF, RIT1 A57G exhibits comparable MAPK activation relative to pathogenic variants with an affinity towards RAF that is indistinguishable from WT RIT1, including the oncogenic M90I allele. This suggests that the activation mechanism may be subject to limiting factors independent of RIT1-RAF binding. Given that other non-classical Ras GTPases, such as MRAS (*18*, *19*), promote MAPK activation in a Ras-dependent manner, we hypothesized that pathogenic RIT1 may also rely on classical Ras for RAF activation. Therefore, to evaluate Ras dependency, we knocked down HRAS, NRAS, and KRAS in WT or $RIT1^{M90I}$ expressing primary mouse embryonic fibroblasts (MEFs). As expected, Ras knockdown attenuated growth-factor induced MAPK activation (**Fig. 3.10A**). Moreover, $RIT1^{M90I}$ enhanced

the ERK signaling response compared to WT and its effect was attenuated by Ras knockdown. However, despite our best efforts to deplete cells of Ras using RNAi, the inefficiency of this approach did not allow for a proper evaluation of Ras dependency. Therefore, we generated HEK293 cells devoid of classical Ras proteins via CRISPR/Cas9-mediated triple knockout (TKO) of *HRAS*, *NRAS*, and *KRAS*, which rendered them insensitive to RTK-mediated MAPK pathway activation (**Fig. 3.10B, C**). The "Rasless" 293 system was then used to evaluate the role of Ras proteins in mutant RIT1-MAPK signaling. Ectopic expression of two pathogenic RIT1 alleles (A57G and M90I) and RIT1 Q79L activated MAPK signaling in control cells but not in Rasless 293 TKO cells (**Fig. 3.5A**). Ectopic rescue of Ras expression in TKO cells reinstated RIT1-mediated MAPK signaling (**Fig. 3.5A)**, suggesting that in this cell system, RIT1 relies on Ras proteins to activate the MAPK pathway. Furthermore, the addition of a dominant-negative S35N mutation (*20*) or a C-terminal deletion mutant confirmed that MAPK activation in control cells was dependent on effector binding and proper localization of RIT1 to the PM, respectively (**Fig. 3.10D**).

As an additional method to assess Ras dependency, we used MEFs that can be rendered "Rasless" upon treatment with 4-hydroxytamoxifen (4OHT) (*19*). Upon genetic deletion of all three Ras genes, pathogenic RIT1 expression failed to restore MAPK pathway activation in response to FBS stimulation compared to ectopically expressed WT KRAS4A or KRAS4B (**Fig. 3.11C**). Since Rasless MEF proliferation is MAPK-dependent (*19*), we assessed cell growth as an additional readout of MAPK activity (**Fig. 3.5B**). Ectopic expression of mutant RIT1 failed to rescue Rasless cell growth; however, we note that a trend towards a partial rescue, most noticeable with RIT1 A57G, was observed (**Fig. 3.5C**). Moreover, mutant RIT1 expression enhanced the proliferation rate of control MEFs, consistent with RIT1-mediated MAPK pathway activation observed here and in other cell models with endogenous Ras expression (*4*, *5*, *17*, *21*). These data suggest that although mutant RIT1 is capable of direct RAF binding, its ability to activate the MAPK pathway is potentiated by the presence of classical Ras proteins. To rule out

indirect MAPK activation upstream of Ras (e.g., through the regulation of positive RAS regulators, such as SHP2 or SOS1/2), we measured Ras-GTP levels from cells expressing pathogenic RIT1 and observed no increase in GTP-loaded Ras that correlated with MAPK pathway activation (**Fig. 5D**).

MEK inhibition attenuates pathological RIT1 MAPK activation and hypertrophy in cardiac tissues

Mutations in pathway components upstream (SHP2 and SOS1) and downstream (RAF1, SHOC2) of Ras that promote MAPK activation define the NS pathogenic landscape (*22*). Intriguingly, the development of NS-associated congenital heart defects, a primary cause of morbidity and mortality, varies depending on the genetic driver. This is particularly notable in certain NS genotypes that are more likely associated with hypertrophic cardiomyopathy (HCM), such as RAF1 and RIT1 NS (*2*, *22*). The high incidence of HCM (50-70%) and related heart defects (pulmonary stenosis and atrial septal defects) (*2*) in RIT1 NS patients prompted us to establish an *in vitro* model system to investigate the impact of mutant RIT1 expression in cardiac cells. To this end, we isolated neonatal cardiomyocytes from mice harboring an engineered *Rit1* locus with Cre recombinase-inducible expression of the pathogenic variant *Rit1*^{M90I} (*5*). Upon isolation, cardiomyocytes were treated with adenoviruses encoding for Cre recombinase to induce expression of the *Rit1*^{M90I} variant. RNA sequencing analysis on day 6 post adenoviral delivery revealed that RIT1^{M90I} expression had elicited broad alterations in the transcriptomic landscape of cardiac myocytes (**Fig 3.6A**). These changes included the upregulation of several well-established MAPK target genes (*Ccnd1*, *Etv4*, *Egr2*, *Dusp2*, and *Ereg*), confirming that pathogenic RIT1 regulates MAPK signaling in this cell type (**Fig 3.11A**)(*23*). In addition, GO and KEGG analyses revealed an enrichment of genes critical for proper cardiac function (**Fig 3.6B and 3.6C**) and whose dysregulation may contribute to the cardiomyopathy-like phenotype exhibited by RIT1 NS murine models (*5*, *24*). Further, these data suggest that upregulation of

MAPK signaling by mutant RIT1 may drive the dysregulation of cardiomyopathy-associated genes, such as *Mybpc3* (Myosin-binding protein C), a causal gene representing approximately 20% of HCM patients (*25*), and *Actc1* (cardiac α-actin), among others (**Fig 3.11B**) (*25*, *26*).

Given the data above, we hypothesized that pharmacological inhibition of the MAPK pathway may ameliorate RIT1^{M90I}-driven cardiac tissue hypertrophy. Therefore, we treated a cohort of 4-week-old mice harboring a germline *Rit1*^{M90I} variant with the allosteric MEK1/2 inhibitor trametinib (MEKi) or vehicle control (**Fig 3.6D**). After 20 weeks of daily treatment, we observed a significant decrease in heart weight of MEKi-treated mice (**Fig 3.6E**), but no difference in spleen weight (**Fig 3.6F**), suggesting that MEK inhibition may reduce aberrant cardiac tissue growth associated with mutant RIT1 expression. Indeed, when the size (cross-sectional area) and proliferative state (Ki67 staining) of myocytes from MEKi and control hearts were compared, MEKi-treated hearts exhibited a marked reduction in both parameters, indicating reduced cell growth (**Fig 3.6G and 3.6H**). Transcriptomic profiling by RNA-seq confirmed that systemic MEKi treatment effectively inhibited MAPK signaling and suggests that the observed reduction in cardiac cell growth was a direct consequence of MEK inhibition within *Rit1*$^{M90I/+}$ hearts (**Fig 3.11C**). Together, these data suggest that pharmacological inhibition of aberrant RIT1-mediated MAPK signaling may represent a viable therapeutic strategy to ameliorate the cardiac defects presented by RIT1 NS patients. Further analysis of our differential gene expression datasets identified two genes, *Ace* (Angiotensin 1 converting enzyme) and *Errfi1* (ERBB Receptor Feedback Inhibitor 1), which were transcriptionally upregulated upon RIT1^{M90I} expression in primary cardiomyocytes, see Fig. 6A, and downregulated in *Rit1*$^{M90I/+}$hearts following MEKi treatment (**Fig 3.6I**). These patterns of expression mark *Ace* and *Errfi1* as potential biomarkers for RIT1 NS individuals with associated HCM.

DISCUSSION

Activation of the MAPK pathway occurs at the inner leaflet of the PM wherein lipid-anchored Ras GTPases recruit RAF kinases and facilitate a multi-step activation process resulting in active RAF dimers (*16*). Since the discovery of RIT1, and its paralog RIT2, the absence of HVR prenylation motifs prompted early speculation into their unique HVR-dependent PM association (*27*). Here, we show that RIT1, like the classical Ras GTPases, requires membrane binding for pathological MAPK activation. An extended polybasic HVR, containing three PBRs, mediates electrostatic interaction with negatively charged phospholipids, a property akin to the polybasic KRAS4B HVR; however, the absence of a RIT1 HVR lipid anchor may allow for transitory and dynamic association with the PM. We have shown that RIT1 diffuses between PM and cytoplasm during mitosis to interact with spindle assembly checkpoint proteins MAD2 and $p31^{comet}$, a process that is regulated through HVR phosphorylation by CDK1 (*20*). Furthermore, appending a C-terminal prenylation motif prevents dissociation from the PM resulting in inactive RIT1 mitotic regulation. Intriguingly, we and others (*8*) have identified non-charged residues (W204, L207, F211) interspersed between the PBRs critical for membrane association. Molecular dynamics simulations have revealed that the hydrophobic side chains of these residues burry deeply into the lipid bilayer (*7*); however, further investigation is needed to determine whether these residues help coordinate the association of PBRs with phospholipid head groups. Furthermore, the uniquely electrostatic association with the PM may enable RIT1 to sense the composition of inner leaflet lipids.

To best interrogate the contribution of membrane association with RAF binding, we developed a BRET assay to quantitate RIT1-RAF association in the context of a native PM environment. We found that perturbations of the RIT1 HVR that abrogated membrane association strongly correlated with decreased RAF binding. Although anticipated, these data exemplify the critical nature of the RIT1 HVR in mediating RIT1's diverse functions. In contrast with previous

reports suggesting that RIT1 associates preferentially with BRAF (*10*), we found through biochemical and biophysical techniques that RIT1 binds most strongly with RAF1. Interestingly, preferential RAF1 binding is a property also shared by the classical Ras family members in intact cells (*9*).

Approximately one-fifth of individuals with RIT1 NS harbor an A57G allele, making it the most common RIT1 variant in this condition (*1*). RIT1 A57G is of particular interest, biochemically, due to its neomorphic enhanced binding to RAF kinases shown here while exhibiting comparable rates of intrinsic GTP hydrolysis, nucleotide exchange, and cellular fraction bound to GTP as other gain-of-function alleles (*5*, *28*). Intriguingly, RIT1 A57G activates MAPK signaling to a similar extent as other pathogenic variants despite an increased affinity to RAF. Thus, RIT1 activation of RAF is not solely correlated to the strength of their interaction, suggesting this is not the limiting factor associated with the modest degree of MAPK pathway activation exhibited by pathogenic RIT1 variants. The cysteine-rich domain (CRD) of RAF1 makes critical contacts with the inter-switch region of KRAS that are essential for RAF activation (*11*). We speculate that the inter-switch region of RIT1, which shares low homology with the Ras inter-switch region, likely fails to engage productively with the CRD of RAF.

Accumulation of RIT1 through the loss of LZTR1-mediated proteasomal degradation increases MAPK signaling, a defining feature of RASopathies (*5*, *29*, *30*). However, as with other NS germline mutants, pathologic RIT1 signaling is mild and thus compatible with embryonic development (*31*). Intriguingly, we have found that activation of MAPK still requires classical RAS proteins, consistent with the fact that deletion of these proteins in mouse cells results in a complete growth arrest (*19*). Further, mutant RIT1 expression did not influence the proportion of GTP-loaded Ras, suggesting that RIT1 promotes MAPK pathway activation downstream of Ras. We posit that despite the low RIT1-RAF affinity, the overabundance of mutant RIT1 protein may facilitate Ras-RAF activation by increasing the local concentration of RAF at the PM, thereby “priming” Ras-RAF activation in response to upstream RTK signaling. However, further

investigation is needed to shed light on the exact mechanism. Nevertheless, our findings suggest that RIT1-driven disease may be treated not only with inhibitors of the MAPK pathway but also with upstream inhibitors that limit Ras activation.

Compared to patients with other genetic variants, RIT1 NS individuals exhibit an elevated frequency of HCM (*2*, *22*). In a prior study, we described a RIT1 M90I mouse model that recapitulated clinical manifestations of NS disease, including cardiac hypertrophy (*5*). Here, we demonstrate that treatment of RIT1 M90I mice with the FDA-approved MEK1/2 inhibitor trametinib (GSK1120212) ameliorated cardiac tissue overgrowth, suggesting that targeting the MAPK pathway may be an effective therapeutic strategy in NS patients with mutant RIT1. Indeed, off-label trametinib treatment was recently shown to reverse myocardial hypertrophy in two children with RIT1 NS (*32*). However, trametinib has been reported to induce significant levels of toxicity in other disease contexts (*33*, *34*), highlighting the need for further pre-clinical work to address optimal dosing and treatment windows, response to different MEK inhibitors, and efficacy of upstream Ras inhibition to alleviate the cardiac and extracardiac RIT1 phenotype. Altogether, these findings aid our mechanistic understanding of RIT1 disease and support the evaluation of broader therapeutic strategies.

Lastly, we must consider the implications of a Ras-dependent RIT1-MAPK activation mechanism in the context of RIT1-driven tumors. Cells expressing RIT1 M90I, but not those expressing KRAS G12V, depend on RTK and adaptor proteins upstream of Ras, including EGFR, GRB2, SHP2, and SOS1 for growth (*35*). Conversely, loss of NF1 and SPRED1, two negative regulators of Ras activity, promote mutant RIT1 cell growth, consistent with our model in which RIT1 relies on active Ras to promote MAPK signaling. Intriguingly, in the same system, Vichas et al. (2021), show that loss of LZTR1 similarly promotes the growth of cells expressing ectopic RIT1 M90I, a variant that is insensitive to LZTR1-mediated degradation, suggesting that stabilization of endogenous RIT1 may provide an additional growth advantage (*5*). Moreover, LZTR1 also promotes MRAS degradation (*5*), and its loss may enhance MRAS-mediated RAF activation in

synergy with mutant RIT1 expression. In support of this hypothesis, mutant RIT1 cells exhibited a strong growth dependency on SHOC2, a scaffolding protein that associates with MRAS to promote Ras-dependent activation of RAF (*36*). Additionally, RIT1 moonlights as a mitotic checkpoint regulator (*20*, *35*), among other functions (*1*, *37*), imparting mutant RIT1 cancer cells with unique therapeutic vulnerabilities (*35*). While our work sheds some light on RIT1's dependency on RTK-MAPK components, further studies are needed to define the contribution of RIT1's various functions to its oncogenic potential.

Figures

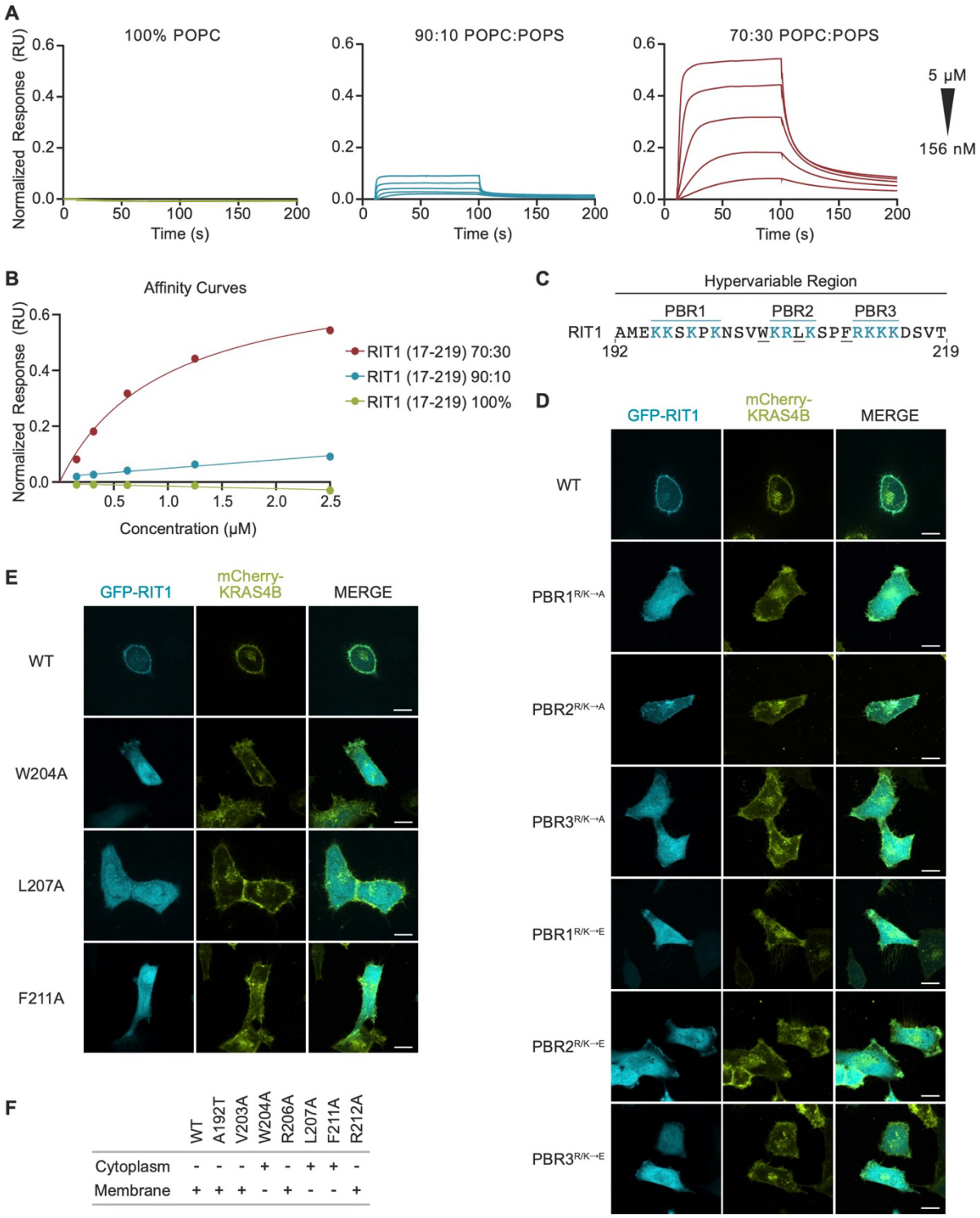

Figure 3.1: RIT1 associates with the plasma membrane through its HVR

(**A**) SPR analysis with increasing concentrations of POPS-containing liposomes showing RIT1 association with negatively charged lipids.

(**B**) SPR affinity curves showing relative binding affinity of RIT1 to lipid constructs.
(**C**) RIT1 C-terminal amino acid sequence. Polybasic regions (PBR) are colored blue.
(**D, F**) Live-cell confocal images of HeLa cells transiently transfected with indicated GFP-RIT1 constructs. Stable expression of mCherry-KRAS4B was used as a plasma membrane marker.
(**F**) Table summarizing the subcellular distribution of indicated GFP-RIT1 C-terminal mutants as in (E) and Fig 3.7.

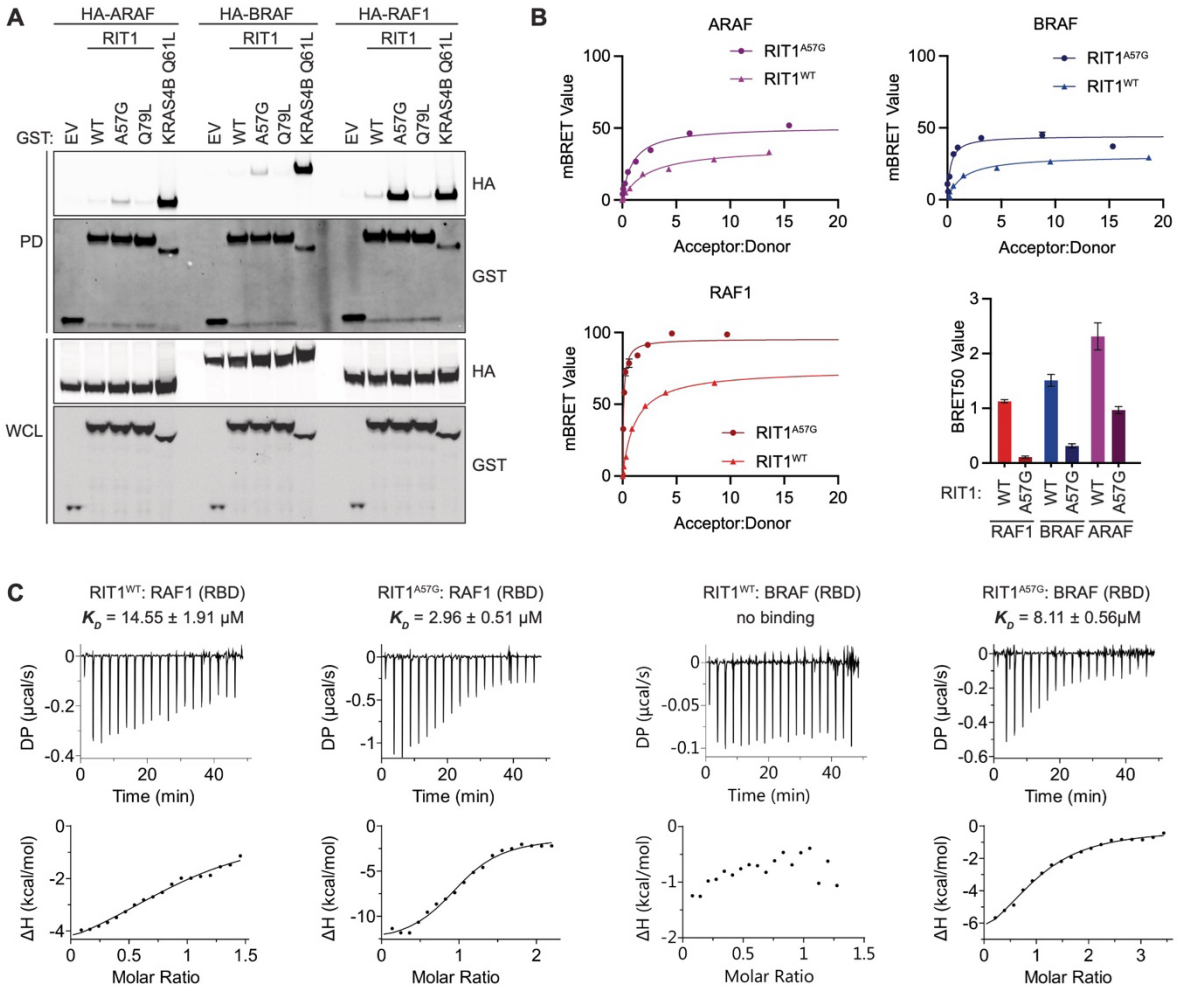

Figure 3.2: RIT1 exhibits preferential binding to RAF1

(**A**) Immunoblot analysis of indicated proteins precipitated by GST pulldown assay from HEK-293T cell lysates expressing indicated constructs. DNA amounts for WT and mutant RIT1 were adjusted to normalize for protein expression. EV, empty vector; WCL, whole-cell lysate. RIT1 Q79L is the corresponding mutation of RAS Q61L.

(**B**) BRET assays showing the relative binding affinities of mVenus-RIT1 (acceptor) and RAF-nanoLuc (donor) proteins. Representative BRET curves from three independent experiments are shown. The histogram demonstrates the mean $BRET_{50}$ values ± SD of three independent experiments.

(**C**) ITC measurements of recombinant RIT1:RAF binding affinities. K_D values represent an average of three independent experiments.

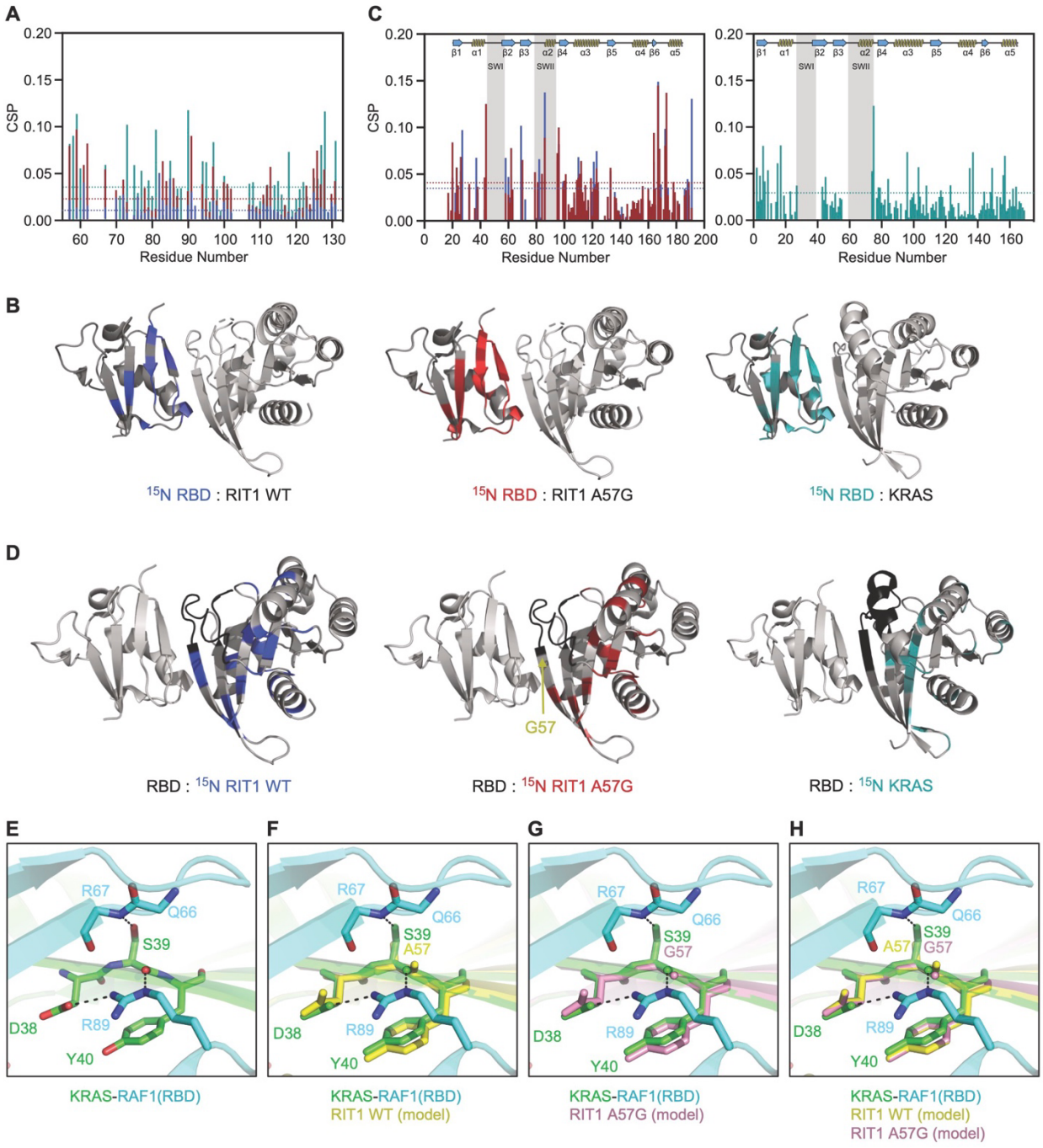

Figure 3.3: Characterization of RIT1-RAF RBD interface by NMR

(**A**) Chemical shift perturbations (CSP) plots for ^{15}N RAF1-RBD observable in complex with unlabeled WT RIT1 (blue), A57G RIT1 (red) & WT KRAS (cyan). Dashed lines represent 1.5σ.
(**B**) CSP shown in (A) and broadened residues were mapped to the 3D-modelled RBD-RIT1 complex and RBD-KRAS structure (PDB: 6VJJ).
(**C**) Left panel represents the CSP for ^{15}N WT RIT1 (blue) and ^{15}N A57G RIT1 (red) in complex with unlabeled RBD. The right panel represents CSP for ^{15}N WT KRAS in complex with unlabeled RAF1-RBD. Dashed lines represent 1.5σ.

(**D**) CSP shown in (C) and broadened residues were mapped to the 3D structures as in (B).
(**E-H**) Comparison of modeled structures of WT and A57G mutant of RIT1 with the crystal structure of KRAS-RAF1(RBD) complex (PDB: 6VJJ). (E) Interaction formed by KRAS S39 (equivalent to A57 in RIT1) and neighboring residues D38 and Y40 with RAF1-RBD. KRAS and RAF1-RBD are colored green and cyan, respectively. (F) Superposition of KRAS-RAF1(RBD) complex with the modeled structure of WT RIT1 (colored yellow) in the active state. (G) Superposition of KRAS-RAF1(RBD) complex with the modeled structure of A57G mutant of RIT1 (colored pink) in the active state. (H) Superposition of KRAS-RAF1(RBD) complex with the modeled structures of WT and A57G mutant of RIT1 in the active state.

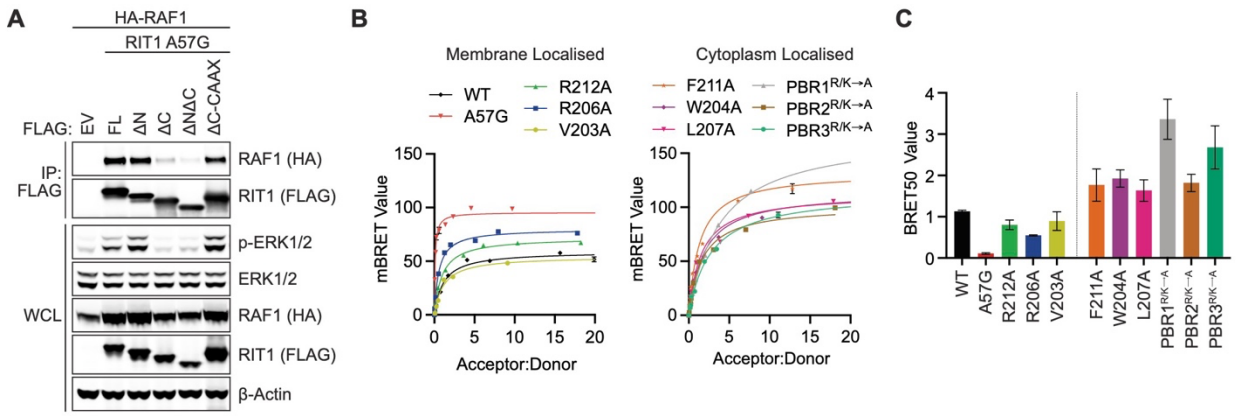

Figure 3.4: RIT1 HVR is required for RAF binding

(**A**) Immunoblot analysis of indicated proteins immunoprecipitated from HEK-293T cell lysates expressing indicated constructs. EV, empty vector; ΔN, a.a. 1-18 deletion; ΔC, a.a. 192-219 deletion; WCL, whole-cell lysate.
(**B**) BRET assays of indicated C-terminal HVR mutants associated with RAF1-nanLuc. One of three experiments is shown.
(**C**) Histogram of BRET50 values indicating the relative binding affinities of RIT1 C-terminal mutants for RAF1-nanoLuc. Mean BRET50 values ± SD of three independent experiments.

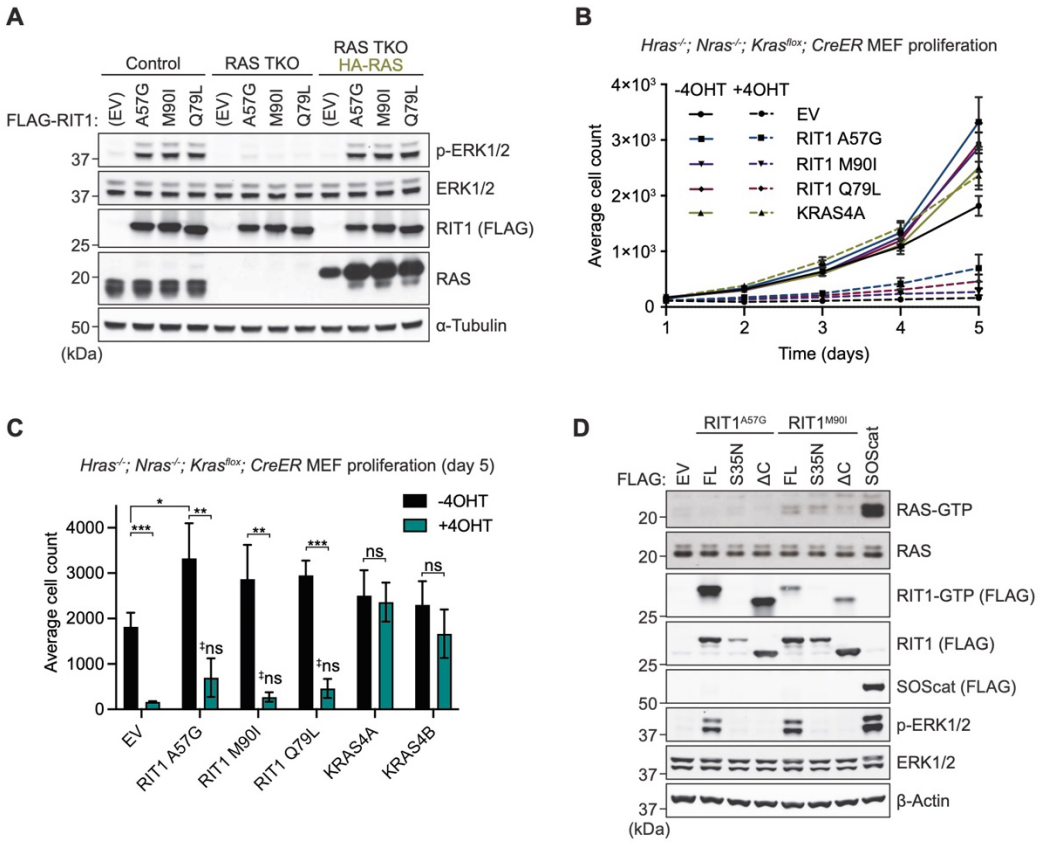

Figure 3.5: Pathogenic RIT1 relies on RAS to potentiate MAPK signaling

(**A**) Immunoblot analysis of indicated proteins from Rasless (HRAS/NRAS/KRAS TKO) or control HEK-293 cells transiently transfected with indicated FLAG-tagged RIT1 constructs or an empty vector (EV) control and serum-starved for 16 h. Rasless cells were rescued with ectopic expression of HA-tagged HRAS, NRAS, KRAS4A, and KRAS4B (1:1:1:1 DNA ratio). One of two independent experiments is shown.

(**B**) Proliferation curves of control (-4OHT) and Rasless (+4OHT) MEFs stably expressing indicated constructs. Data points indicate the mean ± SEM of three biological replicates.

(**C**) Relative cell growth of control (-4OHT) and Rasless (+4OHT) MEFs stably expressing indicated constructs at Day 5 of growth assay as in C. Data points indicate mean ± SD, n = 3, Two-sided Student's t-test, *p ≤ 0.05, **p ≤ 0.01, ***p ≤ 0.001; ‡ns (p>0.05, vs EV+4OHT).

(**D**) Immunoblot analysis of indicated proteins from HEK-293 cells transiently transfected with indicated FLAG-tagged constructs and serum-starved for 16 h. GTP-bound RAS and RIT1 were precipitated with immobilized RAF1-RBD. SOScat (SOS1 a.a. 564–1049). One of two independent experiments is shown.

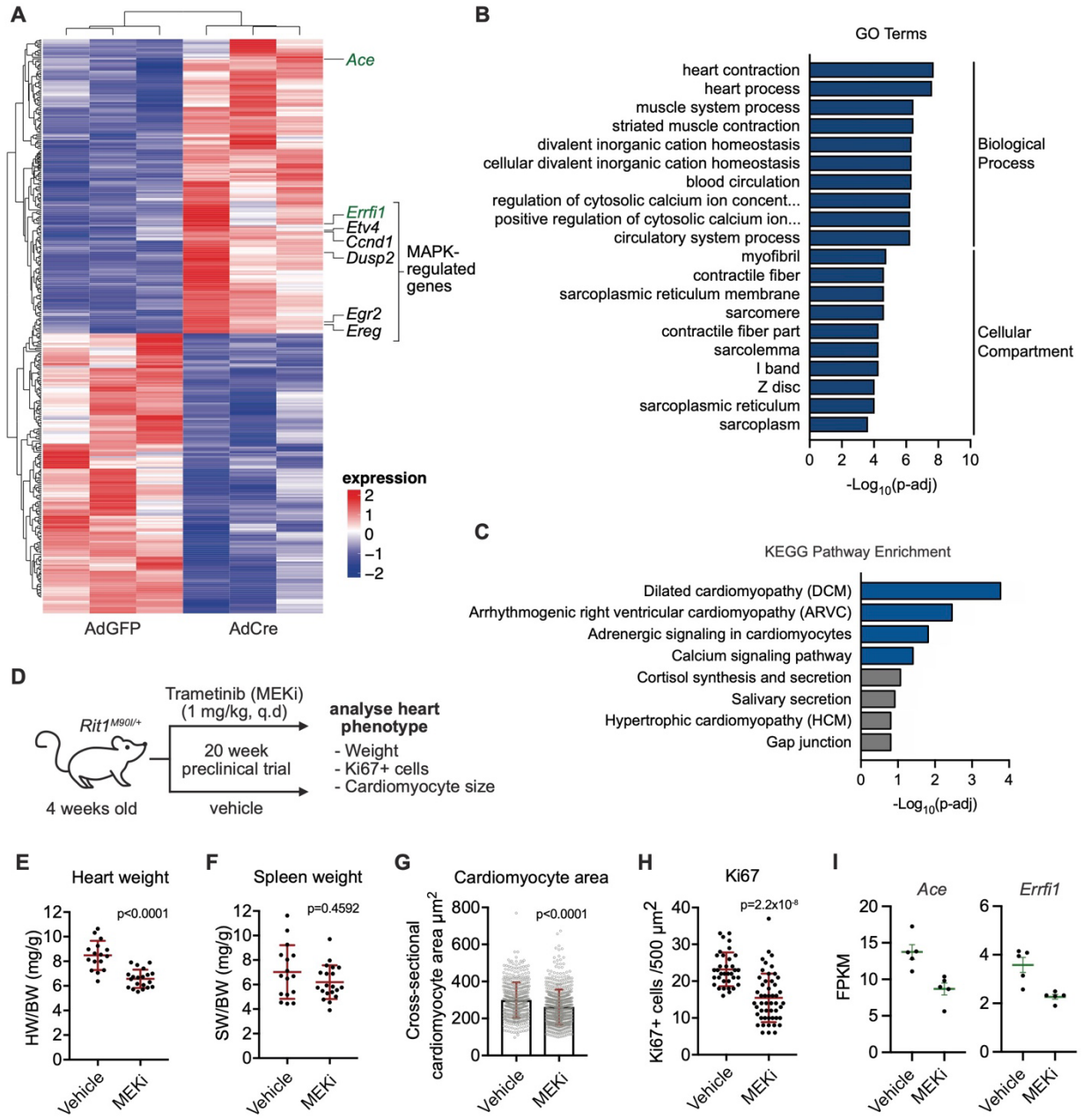

Figure 3.6: MAPK inhibition alleviates RIT1-dependent cardiac hypertrophy

(**A**) Heatmap of top differentially expressed genes in primary cardiomyocytes from *Rit1*$^{LoxP\text{-}M90I}$ neonates treated with adenovirus encoding Cre recombinase (AdCre) or GFP (AdGFP).
(**B, C**) Gene ontology (GO) and KEGG enrichment analysis of differential gene expression elicited by RIT1^{M90I} expression in primary cardiomyocytes (AdCre vs. AdGFP)
(**D**) Schema of 20-week Trametinib (MEKi) preclinical trial with *Rit1*$^{M90I/+}$ mice.
(**E, F**) Comparison of normalised heart (E) or spleen (F) weight between MEKi (n = 16) and vehicle control (n = 20) group. Statistical significance was assessed by a two-tailed Mann-Whitney test. Error bars indicate mean ± SD.

(**G, H**) Quantification of myocyte area (G) and Ki67+ cells (H) from heart cross sections by immunofluorescence and immunohistochemistry, respectively. Statistical significance was assessed by a two-tailed Mann-Whitney test. Error bars indicate mean ± SD.
(**I**) Normalised mRNA transcript levels (FPKM) of indicated genes in hearts (n = 5) isolated from vehicle control or MEKi-treated *Rit1*$^{M90I/+}$ mice at 20-week endpoint. Error bars indicate mean ± SEM.

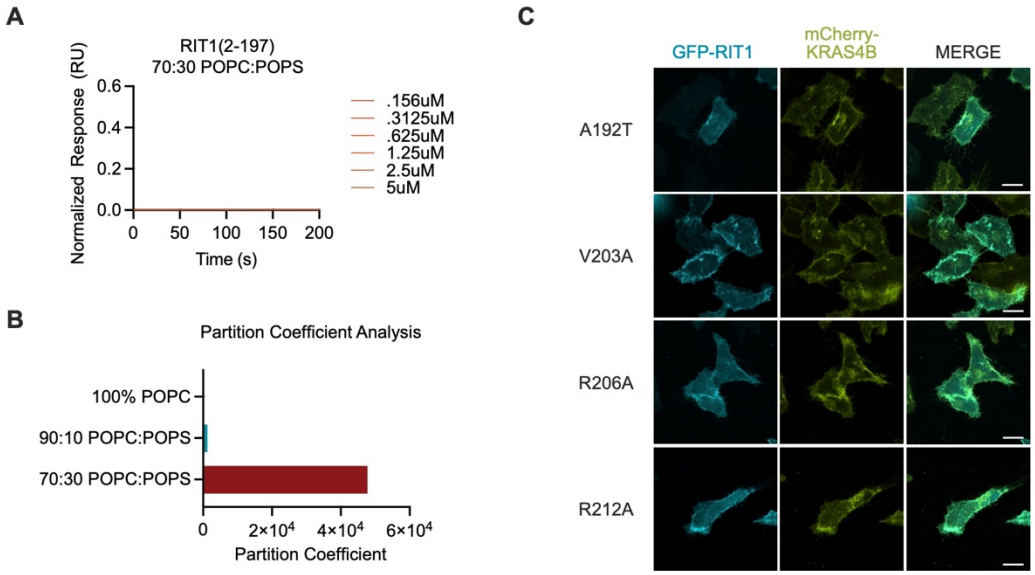

Figure 3.7: In vitro and in vivo analysis of RIT1-PM lipid associations

(**A**) SPR analysis shows no association between 30% POPS-containing liposomes and RIT1 protein (a.a. 2-197) with C-terminal deletion.
(**B**) Partition coefficients derived from SPR affinity curves from Figure 1B show the relative binding affinity of RIT1 to liposomes of indicated composition.
(**C**) Live-cell confocal images of HeLa cells transiently transfected with indicated GFP-RIT1 constructs. Stable expression of mCherry-KRAS4B was used as a plasma membrane marker.

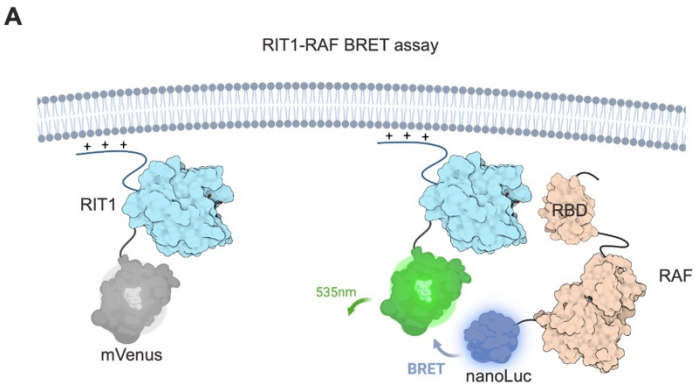

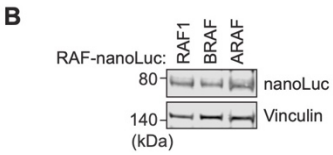

C

Interaction	$BRET_{50}$ Value
WT:RAF1	1.129 ±0.030
A57G:RAF1	0.110 ±0.019
WT: BRAF	1.510 ±0.108
A57G:BRAF	0.315 ±0.038
WT:ARAF	2.314 ±0.247
A57G:ARAF	0.968 ±0.066

Figure 3.8: RIT1 BRET assay reveals preferential binding to RAF1 isoform

(**A**) Schema of BRET assay designed to detect *in vivo* RIT1-RAF binding.
(**B**) RAF-nanoLuc construct transfection was optimized to achieve comparable RAF isoform expression levels.
(**C**) $BRET_{50}$ values calculated from saturation curves in Fig. 2B.

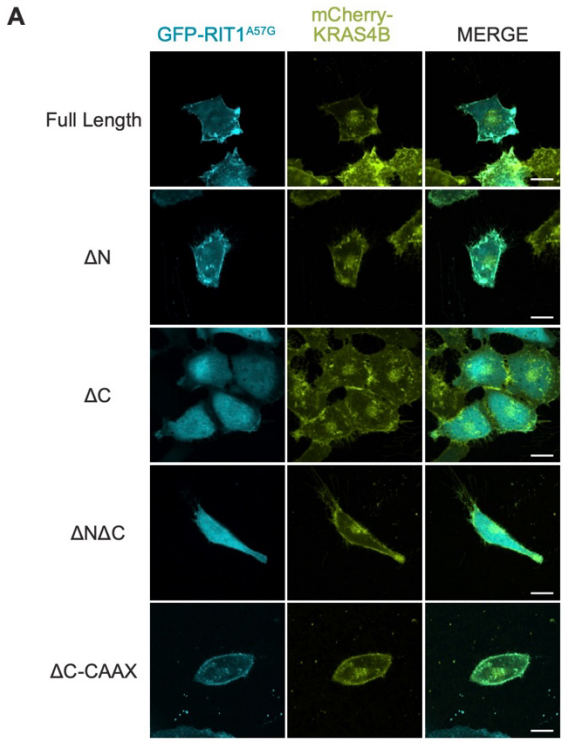

Figure 3.9: C-terminus, but not N-terminus, of RIT1 is essential for PM association

(**A**) Live-cell confocal images of HeLa cells transiently transfected with indicated GFP-RIT1 constructs. Stable expression of mCherry-KRAS4B was used as a plasma membrane marker.

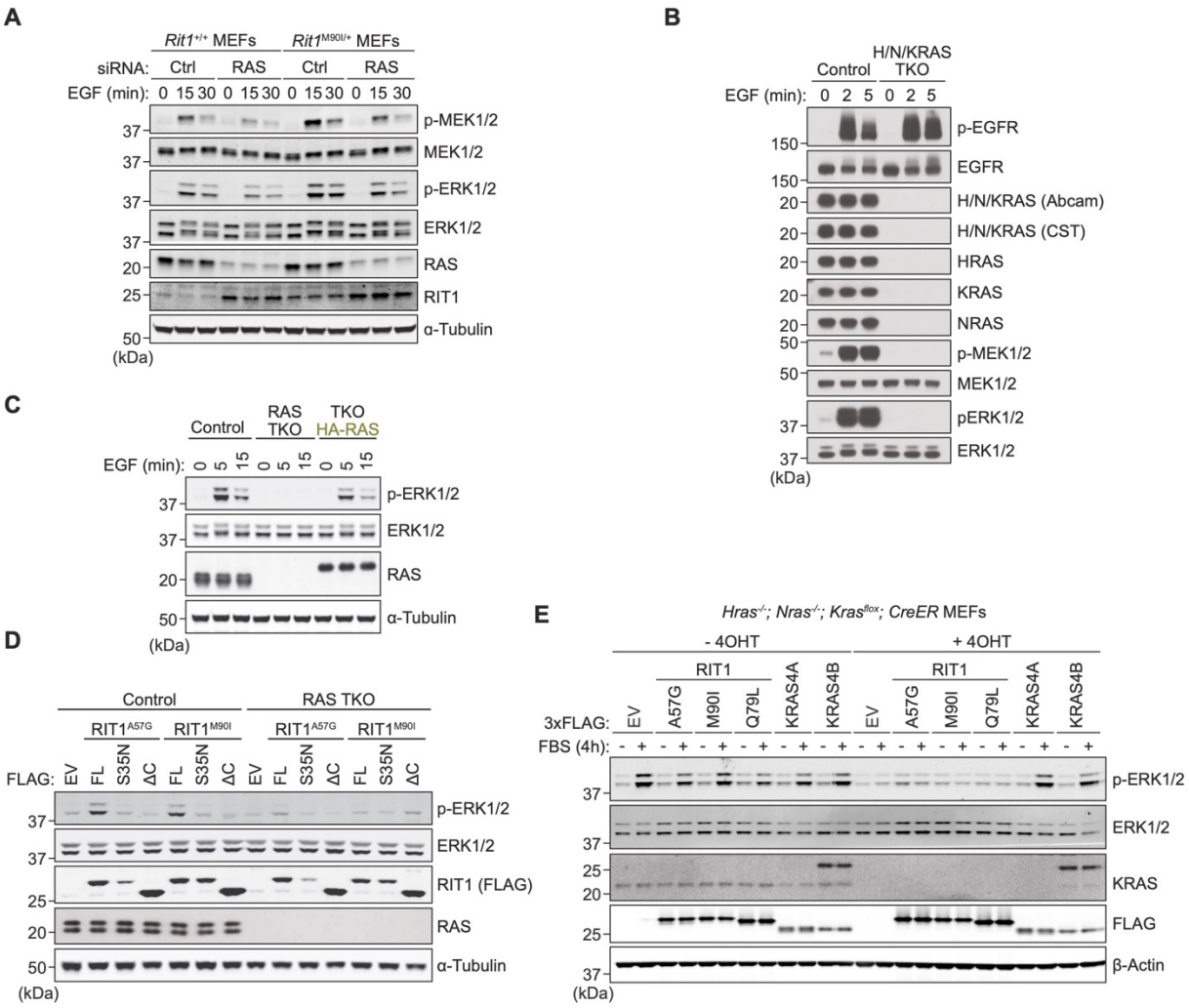

Figure 3.10: RIT1 protein stabilization fails to promote MAPK activation in the absence of RAS

(**A**) Immunoblot analysis of indicated proteins from primary MEFs that were serum-starved overnight and stimulated with 10 ng/ml EGF for indicated times, 72h post siRNA knockdown. One of three independent experiments is shown.
(B) Immunoblot analysis of indicated proteins from Rasless (HRAS/NRAS/KRAS TKO) or control HEK-293 FlpIn cells serum-starved for 16 h and treated with 25 ng/ml EGF for indicated times.
(**C**) Immunoblot analysis of indicated proteins from Rasless or control cells serum-starved for 16 h and treated with 10 ng/ml EGF for indicated times. Rasless cells were rescued with ectopic expression of HA-tagged HRAS, NRAS, KRAS4A, and KRAS4B (1:1:1:1 DNA ratio). One of two independent experiments is shown.
(**D**) Immunoblot analysis of indicated proteins from Rasless or control cells transiently transfected with indicated FLAG-tagged RIT1 constructs or an empty vector (EV) control and serum-starved for 16 h. FL, full length. One of three independent experiments is shown.

(**E**) Immunoblot analysis of indicated proteins from control (-4OHT) and Rasless (+4OHT) MEFs stably expressing indicated constructs, serum-starved overnight and stimulated with or without 10% FBS for 4 h. One of three independent experiments is shown.

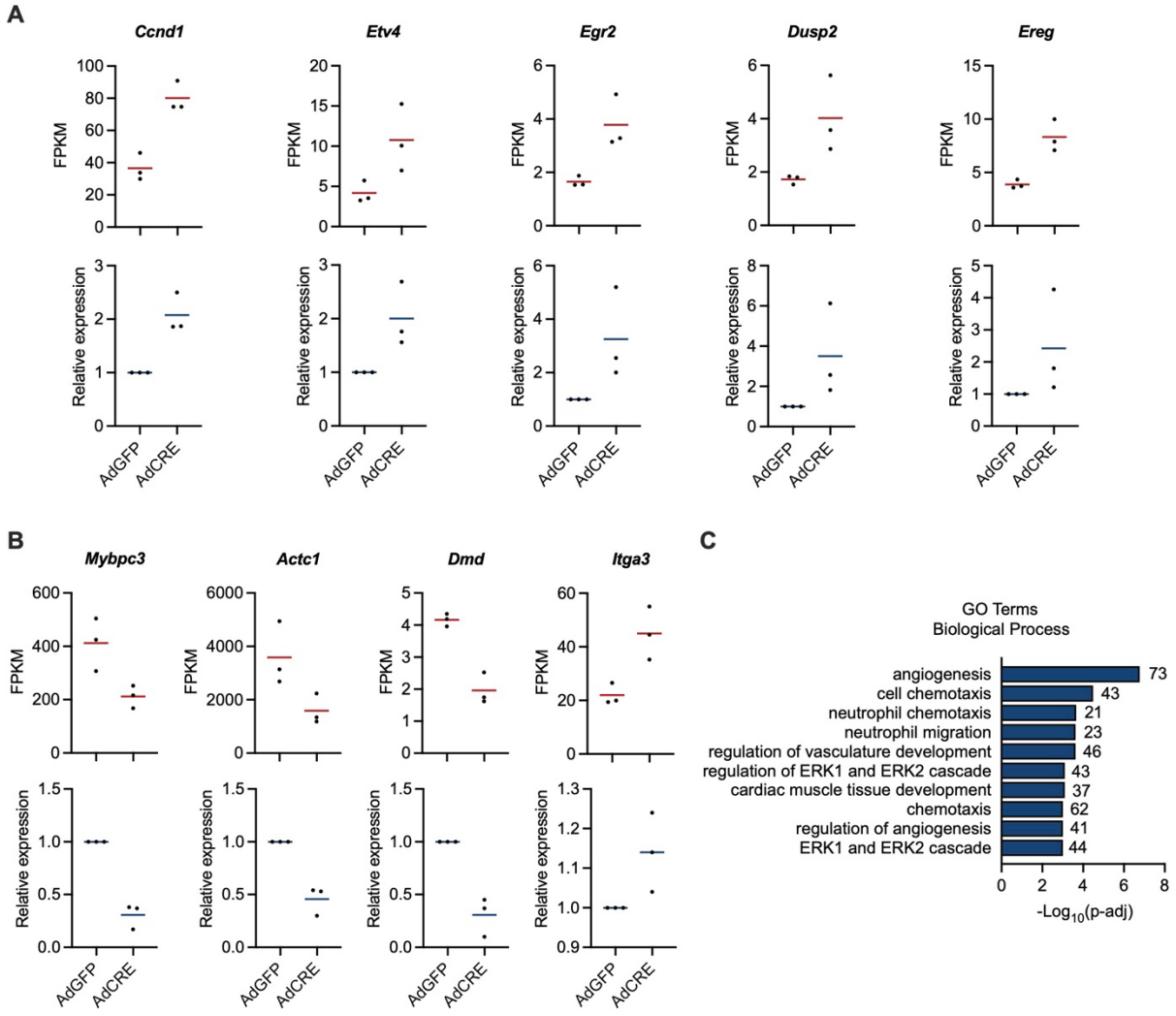

Figure 3.11: Analysis of gene expression elicited by RIT1^{M90I} expression or MEK inhibition

(**A, B**) Gene expression levels of indicated MAPK-regulated genes (**A**) or cardiomyopathy-associated genes (**B**) from primary *Rit1*$^{LoxP\text{-}M90I}$ neonatal cardiomyocytes treated with adenovirus encoding Cre recombinase (AdCre) or GFP (AdGFP). Top panels display normalized mRNA transcript levels (FPKM) from RNA-seq transcriptomic profiling. Bottom panels display relative mRNA expression from an independent set of biological replicates by RT-qPCR.
(**C**) Gene ontology (GO) enrichment analysis of genes downregulated in MEKi-treated hearts (MEKi vs. vehicle control) isolated from the murine preclinical trial described in Figure 6D.

Table 3.1: Broadened residues (blue) and residues above 1.5σ reported in CSP plots

^{15}N RBD + RIT1	^{15}N RBD + G57 RIT1	^{15}N RBD + KRAS	^{15}N RIT1 + RBD	^{15}N G57 RIT1 + RBD	^{15}N KRAS + RBD
T57	T57	T57	R20	R20	Y4
I58	I58	I58	E21	E21	L6
V60	R59	R59	M26	M26	V8
F61	V60	V60	L27	L27	V9
L62	F61	F61	A29	G30	G15
K65	L62	L62	H44	M37	S17
Q66	K65	K65	A57	S43	Q25
T68	Q66	Q66	Y58	H44	H27
V69	R67	R67	I62	K59	F28
N71	T68	T68	A69	I62	V45
V88	V69	V69	N70	A69	D47
R89	V70	V70	L71	L71	L56
Q92	N71	R73	Q79	Q79	T74
A97	L82	G75	M85	A84	G75
L126	M83	L78	R86	M85	I84
Q127	K84	H79	E94	R86	T87
	V88	C81	G95	E94	E91
	R89	A85	F96	G95	Y96
	G90	K87	S101	F96	V103
	L91	V88	E110	Y100	D108
	Q92	R89	R112	S101	R123
	E94	G90	V121	V111	Y137
	A97	L91	R123	R112	R149
	D113	Q92	G133	Y119	F156
	E125	E94	S164	R123	Y157
	L126	A97	A166	V132	
	Q127	A118	Y170	G133	
	V128	I122	D172	S164	
	D129	L126	F175	R168	
		Q127	R180	Y170	
		V128	L191	D172	
		L131		R180	

Table 3.2: gRNA targeting sequences

Target	Sequence
HRAS	TTGGACATCCTGGATACCGC
KRAS	TTGGATATTCTCGACACAGC
NRAS	TTGGACATACTGGATACAGC
AAVS1	GGGACCACCTTATATTCCCA
Chromosome 3	GTTTAAAACTACCACTCCAC
Chromosome 15	GCCTATGGTCTGATAACAAT

Table 3.3: qPCR primers

Target	Forward primer (5'-3')	Reverse primer (5'-3')
Tbp	CCTTGTACCCTTCACCAATGAC	ACAGCCAACATTCACGGTAGA
Etv4	AGACTTCGCCTACGACTCA	CATAACCCATCACTCCATCACC
Ccnd1	CAACAACTTCCTCTCCTGCTAC	GCTTCAATCTGTTCCTGGCA
Dusp2	CGAGGGTTCCGATCTATGAC	CATTGAGAACTGCTGTGATGC
Ereg	CTTCTACAGGCAGTTATCAGCA	GTAGCCGTCCATGTCAGAAC
Erg2	TTGACCAGATGAACGGAGTG	GTGAAGGTCTGGTTTCTAGGTG
Dmd	GCTTATGTTGCCACCTCTGA	CTTCCGTCTCCATCAATGAACT
Itga3	CAGCATCCCTACCATCAACA	CCACAAGCACCAACCACA
Mybpc3	CTGGCAGAAGACTGTAACACA	TCAGTCTCACACAACAGCTTC
Actc1	CCAACCGTGAGAAGATGACC	TCGCCAGAATCCAGAACAATG

MATERIALS AND METHODS

Protein production

Cloning. DNA constructs for the expression of KRAS4B (1-169) (Addgene #159539) and RAF1 (52-131) were previously described (*38*). Gateway Entry clones for BRAF (151-277), RIT1 (17-197), RIT1 (17-197) A57G, and RIT1 (17-219) were generated by standard cloning methods and incorporate an upstream tobacco etch virus (TEV) protease cleavage site (ENLYFQG) followed by the appropriate coding sequences. Sequence-validated Entry clones were sub-cloned into pDest-566, a Gateway Destination vector containing a His6 and maltose-binding protein (MBP) tag to produce the final *E. coli* expression clones (*39*). All expression constructs were in the form containing an N-terminal His6 and maltose-binding protein (MBP) tag (Addgene #11517).

Protein expression. RAF1-RBD (52-131) was expressed using the auto-induction media protocol and BRAF (151-277) and RIT1 proteins were expressed using the Dynamite media protocol (*39*). For ^{15}N isotopic incorporation into RAF1 (52-131), KRAS4B (1-169), RIT1 (17-197), and RIT1 (17-197) A57G, seed cultures were inoculated from glycerol stocks of the transformed strains into 300 mL of Studier's MDAG135 medium (*40*) (25 mM Na_2HPO_4, 25 mM KH_2PO_4, 50 mM NH_4Cl, 5 mM Na_2SO_4, 2 mM $MgSO_4$, 50 µM $FeCl_3$, 20 µM $CaCl_2$, 10 µM $MnCl_2$-$4H_2O$, 10 µM $ZnSO_4$-$7H_2O$, 2 µM $CoCl_2$-$6H_2O$, 2 µM $CuCl_2$-$2H_2O$, 2 µM $NiCl_2$-$6H_2O$, 2 µM Na_2MoO_4-$2H_2O$, 2 µM Na_2SeO_3-$5H_2O$, 2 µM H_3BO_3), 19.4 mM glucose, 7.5 mM aspartate, and 200 µg/ml each of 18 amino acids (E, D, K, R, H, A, P, G, T, S, Q, N, V, L, I, F, W, M) in a 2 L baffled shake flask for 16 hours at 37°C until late-log phase growth. In the interim, 15 L of T-20052 (*41*) medium was prepared in a 20-liter Bioflow IV bioreactor (Eppendorf/NBS). The seed culture was collected and centrifuged at 3,000 x *g* for 10 minutes at 25˚C. The pellet was re-suspended with 100 mL of the sterilized T-20052 medium from the bioreactor and then returned to the bioreactor as inoculum. The culture was grown at 37°C with an airflow of 15.0 LPM and agitation of 350 RPM. Approximately five hr (mid-log phase) after inoculation, the culture was shifted to 20°C

overnight. Cells were collected by centrifugation (5000 x *g* for 10 min at 4°C) and the cell pellet was stored at -80°C.

Protein purification. Proteins were essentially purified as previously described for proteins in the His6-MBP-tev-POI (protein of interest) expression format (*42*). Note that 5 mM $MgCl_2$ was used in buffers used to purify KRAS4B (1-169). Essentially, the His6-MBP-POI was purified by immobilized metal-ion affinity chromatography (IMAC) from the lysate, the His6-MBP tag was removed by His6-TEV protease digestion, the POI was isolated from the TEV digest by another round of IMAC (POI in flow-through, wash, or low imidazole elutions), the pooled protein was buffered exchanged via preparative SEC, concentrated and frozen in liquid nitrogen in aliquots, and stored at -80°C.

Purifications of RIT1 required some alterations to this basic protocol. Specifically, protein concentration was kept below 4 mg/ml throughout, all ^{15}N preparations of RIT1 (17-197) and preparations of RIT1 (17-219) were with 300 mM NaCl and 10% (w/v) glycerol in all buffers. Final buffers were 20 mM HEPES, pH 7.3, 150 mM NaCl, 1 mM TCEP for BRAF (151-277), 10 mM Tris-HCl, pH 7.5, 50 mM NaCl, 2 mM $MgCl_2$ for RAF1 (52-131), 20 mM HEPES, pH 7.3, 150 mM NaCl, 2 mM $MgCl_2$, 1 mM TCEP for RIT1 (17-197) and KRAS4B (1-169) with 5 $MgCl_2$ added for KRAS concentrations greater than 10 mg/ml, and 20 mM HEPES, pH 7.3, 300 mM NaCl, 2 mM $MgCl_2$, 1 mM TCEP, 10% glycerol for RIT1 (17-219) and ^{15}N preparations of RIT1 (17-197).

Liposome SPR

2.5 mM Liposomes were prepared from various amounts of 1-palmitoyl-2-oleoyl-glycero-3-phosphocholine (POPC) and 1-palmitoyl-2-oleoyl-sn-glycero-3-phospho-L-serine (POPS). Lipid mixtures were lyophilized at -80^{o}C for approximately three hours. Lipids were reconstituted in 1 ml 20 mM HEPES pH 7.4, 150 mM NaCl buffer and sonicated at 37^{o}C for 5 minutes. Mixtures underwent five freeze/thaw cycles, followed by another brief sonication until clear.

SPR binding experiments were run on a Biacore T200. Liposomes composed of POPC or POPS were captured on flow cells 2-4 of an L1 Chip, flow cell 1 was unmodified and served as a reference. RIT1 was diluted in SPR running buffer (20 mM HEPES pH 7.4, 150 mM NaCl), concentration range, 5 – 0.156 μM (1:2-fold dilutions) and injected on the chip surface at 30 μl/min. Sensorgrams were normalized by the capture level of liposomes. Partition coefficients were calculated as described previously (*43*).

GNP exchange

RIT1 (2 mg) was diluted in Alkaline Phosphatase buffer (40 mM Tris pH 7.4, 200mM Ammonium Sulphate, 1mM $ZnCl_2$, 10% glycerol). 10 mM GppNHp and 5 units of alkaline phosphatase beads were added to RIT1, and the mixture was incubated for one hour at 4^{o}C with constant rotation. Beads were pelleted out, and 30 mM $MgCl_2$ was added to the mixture, followed by another brief incubation at 4^{o}C. Protein was desalted on a HiPrep 26/10 desalting column into buffer (20 mM HEPES pH 7.4, 150 mM NaCl, 5 mM $MgCl_2$, 1 mM TCEP). The efficiency of exchange was measured by HPLC analysis, as previously published (*41*).

Isothermal titration calorimetry

ITC experiments were run on a MicroCal PEAQ-ITC instrument. The proteins were diluted to 100 μM (RIT1) and 300 μM (RAF) in 20 mM HEPES, 150 mM NaCl, pH 7.4, 5 mM $MgCl_2$, 1 mM TCEP buffer. Approximately 200 μl RIT1 was loaded into the cell of the instrument, and 80 μl RAF was loaded into the syringe. 4.4 μl of RAF1 was titrated onto RIT1 every 2 minutes, for a total of 19 injections. After all injections were complete, the data was analyzed using the MicroCal PEAQ-ITC analysis software to calculate the K_D.

NMR

RAF1-RBD (52-131), RIT1(17-197) WT/A57G, and WT KRAS4B (2-169) and their complexes were characterized by solution NMR spectroscopy. For all these proteins, published backbone

assignments were used initially with in-home NMR assignments whenever required (BMRB IDs: RAF1 (17382), RIT1 (26787), and KRAS (28021)). All ^{15}N labeled proteins used in this study had concentrations between 100 μM to 150 μM. Protein-protein complexes were pre-formed at a 1:3 ratio (3-fold excess of unlabelled partner) and the saturating complex was confirmed by observing the signal of the key reporting residues. 2D ^{1}H-^{15}N HSQC spectra were recorded at 25 ^{o}C on a Bruker 700MHz spectrometer equipped with proton-cooled cryogenic $^{1}H/^{13}C/^{15}N$ triple resonance probes. The sample temperature was calibrated with a 100% methanol sample before the experiments. All ^{1}H – ^{15}N HSQC spectra were collected with 1K and 128 complex points in F2 (^{1}H) and F1(^{15}N) respectively, with 16 scans. All experiments used a ^{1}H spectra width of 9090 Hz and a ^{15}N spectral width of 1987 Hz with the proton and ^{15}N carriers set to 4.7 ppm and 120 ppm. Data were processed by NMRPipe (*44*), analyzed by NMRFAM-SPARKY (*45*), GraphPad Prism was used to plot CSP plots and PyMOL was used to map CSP to X-ray structures. Chemical shift perturbations (CSP) were calculated by using the equations Sqrt{(dH^2+(dN/10)^2)/2}, where dH and dN are the proton and nitrogen chemical shift differences between the complexed and non-complexed proteins.

Cell lines and culture conditions

HeLa and HEK-293T cells were obtained from the American Type Culture Collection (ATCC). FlpIn HEK-293 cells were obtained from Thermo Fisher. *Hras$^{-/-}$; Nras$^{-/-}$; Kras^{flox}; CreER* mouse embryonic fibroblasts (MEFs) were a kind gift from Nikki Fer (Frederick National Laboratory). Cells were cultured in Dulbecco's modified Eagle's medium (DMEM) supplemented with 10% Fetal Bovine Serum (FBS). Cells were grown in a humidified incubator with 5% CO2 at 37°C. Validation procedures are as described by the manufacturer. Cell lines were regularly tested and verified to be mycoplasma negative using MycoAlert PLUS Mycoplasma Detection Kit (Lonza).

For the generation of Rasless 293 cells, crRNA targeting HRAS (Integrated DNA Technologies (IDT)) and ATTO 550 labeled tracrRNA (IDT) were combined to a final concentration of 1 μM and annealed by cooling from 95°C to room temperature. 12 pmol crRNA:tracrRNA duplex was combined with 12 pmol recombinant HiFi Cas9 (IDT) and reverse transfected into HEK293 Flp-In cells using Lipofectamine CRISPRMAX reagent (Thermo Fisher Scientific) following IDT protocols. 24 hours after transfection ATTO 550 positive cells were sorted using a Sony SH800 Cell Sorter and allowed to recover for four days. Following the same procedure, cells were then sequentially transfected with NRAS and KRAS crRNA:tracrRNA-Cas9 ribonucleoprotein complexes. For the final cell sorting step following KRAS crRNA:tracrRNA-Cas9 transfection, single ATTO 550 positive cells were sorted into 96-well plates. Clonal cell lines were then expanded and screened for HRAS, KRAS and NRAS knock-out by western blotting using antibodies specific for the individual RAS isoforms and two pan-H/K/NRAS antibodies. Five confirmed triple knock-out clones were then pooled to mitigate off-target guide RNA effects and clonal heterogeneity, and validated functionally through the absence of MAPK signaling. To generate HEK293 Flp-In control sgRNA cells, the same procedures were performed in parallel targeting safe loci in AAVS1, chromosome 3 and chromosome 15 (*46*). Single-cell clones were expanded, and normal activity and expression of RAS signaling pathway components were confirmed by western blotting. 12 clones were then pooled to give a polyclonal control sgRNA cell line. See Appendix Table 3.2 for sgRNA targeting sequences.

For the generation of Rasless MEFs with stable expression of ectopic RIT1 or Ras, lentivirus was produced by co-transfection of HEK293T cells with a lentiviral vector and the packaging plasmids psPAX2 (Addgene, plasmid #12260) and pMD.2G (Addgene, plasmid #12259) at a ratio of 1.25:1.0:0.25. The supernatant was collected 72 hours post-transfection and filtered through a 0.45 μm filter. *Hras*$^{-/-}$*; Nras*$^{-/-}$*; Kras*^{flox}*; CreER* MEFs were transduced with lentiviral-containing supernatant supplemented with 0.8 μg/ml polybrene (Sigma-Aldrich). Stably transduced cells

were selected with 1.5 μg/ml Puromycin (Sigma-Aldrich). To remove the floxed *Kras* allele, stable cells were treated with 1μM 4-hydroxytamoxifen (4OHT, Sigma-Aldrich). Assays with Rasless MEFs were conducted 10-11 days post 4OHT treatment and loss of KRAS was verified by immunoblot.

Mammalian expression constructs

All RIT1 cDNA mutants were generated using standard PCR-based site-directed mutagenesis in the pDONR223-RIT1 template and were previously described (*20*). KRAS4A and KRAS4B entry clones (Addgene plasmids 83166 and 83129) and ARAF, BRAF, and RAF1 (plasmids 70293, 70299, and 70497) were a gift from Dominic Esposito (Frederick National Lab). SOScat (SOS1 residues 564–1049) was previously described (*29*). For N-terminal GST-tagged proteins, entry clones were gateway cloned into pDEST27 destination vector (Invitrogen). For N-terminal mCherry-, EGFP- or FLAG-tagged constructs, entry clones were cloned by multisite gateway cloning into pDEST302 or pDEST663 (a gift from Dominic Esposito, Frederick National Lab) and with expression controlled by an EF1a promoter. HA-tagged constructs were gateway cloned into a pcDNA-HA destination vector. Empty vector (EV) plasmid controls were generated using a gateway recombination cassette containing a stop codon followed by an untranslated stuffer sequence.

RNA interference

To knockdown RAS, individual pools of short interfering RNAs (siRNAs) against mouse *Hras*, *Nras*, and *Kras* (SMARTpool: ON-TARGETplus, Horizon) were pooled in equal amounts and transfected into cells using Lipofectamine RNAiMax Transfection Reagent (Life Technologies) according to manufacturer's instructions. Non-targeting control siRNA was purchased from Horizon (D-001810-10-05).

Primary cardiomyocyte isolation

Preparation of mouse neonatal cardiac myocytes was conducted as previously described (*47*) with some modifications. Briefly, hearts were extracted from 1–3-day old neonates, placed in ice-cold HBSS, cleared of blood clots and aortic tissue, then placed in fresh ice-cold HBSS and cut into small pieces to be digested in prewarmed HBSS with 1 mg/ml Collagenase Type 2 (Life Technologies) at 37 ^{o}C for 5 min with gentle agitation. Heart pieces were then allowed to sediment for 1 minute, and the supernatant was removed and discarded. The following digestion process was repeated six times: heart pieces from before were resuspended in fresh HBSS with 1 mg/ml Collagenase and incubated at 37 ^{o}C for 5 min with gentle agitation. Heart pieces were then allowed to sediment for 1 min and the supernatant containing suspended cardiac myocytes was transferred to a new tube containing 1/10 volume of cardiomyocyte medium (DMEM supplemented with 10% FBS, 10% Nu serum (Corning), 1x Penicillin-Streptomycin (Gibco), 1x Glutamax (Gibco), 1x ITS liquid medium supplement (Sigma), and 10 mM HEPES (Gibco)) and centrifuged to pellet cells (500g for 5 min). Cell pellets were resuspended in 1 ml cardiomyocyte medium and pooled after the sixth collection, passed through a cell strainer multiple times and incubated at 37 ^{o}C for 2 hours in a plastic 10cm dish. Unadhered cells in cell suspension were then pelleted by centrifugation and resuspended in 1 ml cardiomyocyte medium per heart and seeded on a laminin-coated 12-well plate at a density of ~1 heart per well. Cells were exchanged into fresh media daily and infected with 2 x 10^8 adenoviral particles encoding GFP or GFP-Cre (ViraQuest), per well, on day 3.

RT-qPCR

Total RNA from cardiomyocytes was obtained on day 6 post adenovirus infection using the RNeasy kit (Qiagen) according to the manufacturer's instructions. cDNA was obtained by reverse transcription (RT) of 1 ug RNA using qScript XLT cDNA SuperMix (QuantaBio; 95161). 10 ng of

cDNA was diluted in nuclease-free water and ran in technical triplicates using PowerUp SYBR Green Master Mix (Applied Biosystems) on a QuantStudio 5 (Thermo Fisher Scientific). *Tbp* (TATA-box binding protein) was used as an endogenous control. See Appendix Table 3.3 for primer sequences.

Live-cell imaging

HeLa cells were seeded onto 12-well #1.5 glass bottom plates (Cellvis) and transiently transfected with Fugene 6 (Promega), following the manufacturer's instructions. Before imaging, cells were exchanged into imaging media: FluoroBrite DMEM (Thermo Fisher Scientific) supplemented with 10% FBS and 4 mM GlutaMAX (Thermo Fisher Scientific). Images were acquired as a series of 0.6 µm z-stacks with a Plan Apo 40x/0.95 Corr (DIC N2 / 40X I) 227.5 nm/pixel objective (Nikon) on a Nikon Ti-E inverted CSU-22 spinning disk confocal microscope equipped with an incubation chamber (Okolab), providing a humidified atmosphere at 37 °C with 5% CO2. Images were processed using Fiji (*48*).

NanoBRET RIT1/RAF Interaction Assay

HEK293T cells were seeded in a 12-well plate at a density of 1.25 x10^5 cells/well. After 24 hours, cells were transfected with mVenus-RIT1 and RAF-nanoLuc using Fugene 6. The concentration of donor (nanoLuc) was kept constant, and the concentration of acceptor (mVenus) was diluted 2-fold (concentrations range 0ng-1000 ng). An empty vector plasmid was transfected into cells to normalize the DNA amount in each well. 48 hours post-transfection, cells were trypsinized and recovered in DMEM cell media containing 10% fetal bovine serum. Tubes were spun down at 1500 rpm for 3 minutes and the pellet was resuspended in Dulbeccos's PBS (PBS) + 0.5% FBS. A cell suspension (20,000 cells) was added in triplicate to both a white 384 well PE Optiplate (for BRET reading), and a black 384well plate (for mVenus reading). 20 PBS + 0.5% FBS was added to each well of cells in the black plate to bring the final volume to 40 µl. 20 µl of 30 mM nanoBRET

nano-Glo substrate (Promega) was added to all required wells of the 384-well PE Optiplate. Plates were read on a PerkinElmer Envision plate reader. The white plate was monitored at 535 nm (BRET signal) and 470 nm (background nanoLuc). mVenus was monitored in the black plate at 530 nm emission with an excitation at 500 nm. The BRET value at each point was measured by dividing the BRET signal by the background nanoLuc signal. Acceptor/donor ratios were normalized against control with equal amounts of mVenus-RIT1(1-219) and RAF-nanoLuc transfected. Data were analyzed with GraphPad Prism software using a non-linear regression fit to obtain the $BRET_{50}$ values.

Pulldowns and Immunoblotting

For GST pulldown of proteins from cell lysates, 3 x 10^6 HEK293T cells were transfected with 4 µg total DNA of indicated plasmids. 24 hours after transfection, cells were rinsed with ice-cold PBS and lysed with 1 ml of lysis buffer (50 mM Tris-HCl (pH 8.0), 150 mM NaCl, 1% IGEPAL CA-630, 10% glycerol) supplemented with protease and phosphatase inhibitor cocktails (Sigma-Aldrich). Lysates were cleared by centrifugation and incubated with 20 µl of Glutathione Sepharose 4B beads for 4 h at 4°C with end-over-end rotation. Beads were rinsed three times with Lysis buffer and resuspended in LDS sample buffer.

Whole-cell lysates for immunoblot analysis were prepared using RIPA Buffer (50 mM Tris-HCl (pH 8.0), 150 mM NaCl, 0.5% sodium deoxycholate, 0.1% SDS, 1% IGEPAL CA-630) supplemented with protease and phosphatase inhibitor cocktails (Sigma-Aldrich). 15-30 µg of total protein was loaded per well of precast NuPAGE gels (Life Technologies).

For immunoblot detection, samples were separated by SDS-PAGE and transferred onto nitrocellulose membranes. Membranes were blocked using 5% skimmed milk in TBST buffer for 1 hour and incubated with appropriate primary antibodies overnight. Detection was performed using secondary antibodies conjugated to DyLight680 (611-144-002; 1:10,000) or DyLight800

(610-145-002; 1:10,000) (Rockland), and visualized with a LI-COR Odyssey infrared scanner or using HRP-linked secondary antibodies and developed with Amersham ECL (Cytiva Life Sciences) and X-ray films. Primary antibodies against p-ERK (4370; 1:1000-2000), ERK1/2 (4696 and 4695; 1:1000), p-MEK (9154; 1:1000), MEK1/2 (4694 and 8727; 1:1000), p-EGFR (3777; 1:1000), EGFR (4267; 1:1000), HA (3724, 1:1000), and FLAG (14793; 1:1000) were obtained from Cell Signal Technology. Antibodies against GST (sc-138; 1:1000) and HRAS (sc-520; 1:500) were obtained from Santa Cruz Biotechnology. RIT1 (ab53720; 1:1000), NRAS (ab167136; 1:2000), and pan-RAS (ab108602; 1:1000) antibodies were from Abcam. KRAS (WH0003845M1; 1:500), βActin (A2228; 1:10000), α-Tubulin (T6199; 1:5000), and FLAG (F1804; 1:2000) antibodies were purchased from Sigma-Aldrich.

Mice

Conditional Rit1^{M90I} mice were previously described (*5*). To generate the experimental cohorts, conditional homozygous male Rit1^{M90I} mice were crossed to homozygous female CMV-Cre deleter transgenic mice. Offspring were weaned at three weeks of age and treatment was started at four weeks of age for a period of 20 weeks. Both male and female littermates were included in this study. Trametinib was purchased from Selleckchem and was diluted in 0.5% carboxymethylcellulose and 0.2% Tween-80 (Sigma). Upon completion of the 20 weeks, mice were given the last dose in the morning and euthanized 2 hours later. Body, heart, and spleen weight was recorded. Both heart and spleen were fixed in phosphate-buffered formalin overnight. This study was performed in strict accordance with the recommendations in the Guide for the Care and Use of Laboratory Animals of the National Institutes of Health. All the animals were handled according to approved institutional animal care and use committee (IACUC) protocol #AN165444 of the University of California San Francisco.

For the quantification of cardiomyocyte size, transverse cardiac tissue sections were stained with Texas-Red-conjugated wheat germ agglutinin (W21405; 1:200) to label the cell boundaries and

counter-stained with DAPI. Five images of cardiac tissue adjacent to the left ventricle were captured at 20X magnification for at least three mice per treatment group. The cross-sectional area of 30 cardiomyocytes per image was measured using Fiji.

Acknowledgments

We thank Dom Esposito and Vanessa Wall (Frederick National Lab) for the multisite gateway plasmid toolkit and members of the McCormick lab for their input. We would like to acknowledge Julia Cregger, Matt Drew, Peter Frank, José Sánchez Hernández, Min Hong, Jennifer Mehalko, Zhaojing Meng, Nitya Ramakrishnan, Rosemilia Reyes, Troy Taylor, and Vanessa Wall from the Protein Expression Laboratory at the Frederick National Laboratory for cloning, expression, purification and quality control of all proteins used in this work. We would also like to thank Megan Rigby for assistance with establishing the BRET measurements. We thank Ting-Yu Lin (UCSF) for providing cardiomyocyte isolation technical advice and Emanuela Zacco (UCSF-Laboratory for Cell Analysis) for technical support. Data for this study were acquired at the Nikon Imaging Center at UCSF. This work was supported by the National Cancer Institute (F31CA265066 to A.C.-N.; R35CA197709 to F.M.; and R00CA245122 to P.C.), the DOD CDMRP Neurofibromatosis Research Program (W81XWH-20-1-0391 to P.C.) and the Thrasher Foundation Early Investigator Award (to P.C.). This project has been funded in whole or in part with Federal funds from the National Cancer Institute, National Institutes of Health, under Contract No. 75N91019D00024. The content of this publication does not necessarily reflect the views or policies of the Department of Health and Human Services, nor does mention of trade names, commercial products or organizations imply endorsement by the U.S. Government. Support was part of the Frederick National Laboratory's Laboratory Directed Exploratory Research (LDER) Program.

References

1. R. Van, A. Cuevas-Navarro, P. Castel, F. McCormick, The molecular functions of RIT1 and its contribution to human disease. *Biochem J*. **477**, 2755–2770 (2020).

2. M. Yaoita, T. Niihori, S. Mizuno, N. Okamoto, S. Hayashi, A. Watanabe, M. Yokozawa, H. Suzumura, A. Nakahara, Y. Nakano, T. Hokosaki, A. Ohmori, H. Sawada, O. Migita, A. Mima, P. Lapunzina, F. Santos-Simarro, S. García-Miñaúr, T. Ogata, H. Kawame, K. Kurosawa, H. Ohashi, S.-I. Inoue, Y. Matsubara, S. Kure, Y. Aoki, Spectrum of mutations and genotype-phenotype analysis in Noonan syndrome patients with RIT1 mutations. *Hum Genet*. **135**, 209–222 (2016).

3. Y. Aoki, T. Niihori, T. Banjo, N. Okamoto, S. Mizuno, K. Kurosawa, T. Ogata, F. Takada, M. Yano, T. Ando, T. Hoshika, C. Barnett, H. Ohashi, H. Kawame, T. Hasegawa, T. Okutani, T. Nagashima, S. Hasegawa, R. Funayama, T. Nagashima, K. Nakayama, S.-I. Inoue, Y. Watanabe, T. Ogura, Y. Matsubara, Gain-of-function mutations in RIT1 cause Noonan syndrome, a RAS/MAPK pathway syndrome. *Am J Hum Genet*. **93**, 173–180 (2013).

4. M. Koenighofer, C. Y. Hung, J. L. McCauley, J. Dallman, E. J. Back, I. Mihalek, K. W. Gripp, K. Sol-Church, P. Rusconi, Z. Zhang, G.-X. Shi, D. A. Andres, O. A. Bodamer, Mutations in RIT1 cause Noonan syndrome - additional functional evidence and expanding the clinical phenotype. *Clin Genet*. **89**, 359–366 (2016).

5. P. Castel, A. Cheng, A. Cuevas-Navarro, D. B. Everman, A. G. Papageorge, D. K. Simanshu, A. Tankka, J. Galeas, A. Urisman, F. McCormick, RIT1 oncoproteins escape LZTR1-mediated proteolysis. *Science*. **363**, 1226–1230 (2019).

6. T. N. Figueira, J. M. Freire, C. Cunha-Santos, M. Heras, J. Gonçalves, A. Moscona, M. Porotto, A. Salomé Veiga, M. A. R. B. Castanho, Quantitative analysis of molecular partition towards lipid membranes using surface plasmon resonance. *Sci Rep*. **7**, 45647 (2017).

7. A. D. Migliori, L. A. Patel, C. Neale, The RIT1 C-terminus associates with lipid bilayers via charge complementarity. *Comput Biol Chem*. **91**, 107437 (2021).

8. W. D. Heo, T. Inoue, W. S. Park, M. L. Kim, B. O. Park, T. J. Wandless, T. Meyer, PI(3,4,5)P3 and PI(4,5)P2 lipids target proteins with polybasic clusters to the plasma membrane. *Science*. **314**, 1458–1461 (2006).

9. E. M. Terrell, D. E. Durrant, D. A. Ritt, N. E. Sealover, E. Sheffels, R. Spencer-Smith, D. Esposito, Y. Zhou, J. F. Hancock, R. L. Kortum, D. K. Morrison, Distinct Binding Preferences between Ras and Raf Family Members and the Impact on Oncogenic Ras Signaling. *Mol Cell*. **76**, 872-884.e5 (2019).

10. G.-X. Shi, D. A. Andres, Rit contributes to nerve growth factor-induced neuronal differentiation via activation of B-Raf-extracellular signal-regulated kinase and p38 mitogen-activated protein kinase cascades. *Mol Cell Biol*. **25**, 830–846 (2005).

11. T. H. Tran, A. H. Chan, L. C. Young, L. Bindu, C. Neale, S. Messing, S. Dharmaiah, T. Taylor, J.-P. Denson, D. Esposito, D. V. Nissley, A. G. Stephen, F. McCormick, D. K. Simanshu, KRAS interaction with RAF1 RAS-binding domain and cysteine-rich domain provides insights into RAS-mediated RAF activation. *Nat Commun*. **12**, 1176 (2021).

12. P. Rodriguez-Viciana, P. H. Warne, A. Khwaja, B. M. Marte, D. Pappin, P. Das, M. D. Waterfield, A. Ridley, J. Downward, Role of phosphoinositide 3-OH kinase in cell transformation and control of the actin cytoskeleton by Ras. *Cell*. **89**, 457–467 (1997).

13. H. Nakhaeizadeh, E. Amin, S. Nakhaei-Rad, R. Dvorsky, M. R. Ahmadian, The RAS-Effector Interface: Isoform-Specific Differences in the Effector Binding Regions. *PLoS One*. **11**, e0167145 (2016).

14. G. N. Ramachandran, C. Ramakrishnan, V. Sasisekharan, Stereochemistry of polypeptide chain configurations. *J Mol Biol*. **7**, 95–99 (1963).

15. N. Bhattacharjee, P. Biswas, Position-specific propensities of amino acids in the β-strand. *BMC Struct Biol*. **10**, 29 (2010).

16. E. M. Terrell, D. K. Morrison, Ras-Mediated Activation of the Raf Family Kinases. *Cold Spring Harb Perspect Med*. **9**, a033746 (2019).

17. A. H. Berger, M. Imielinski, F. Duke, J. Wala, N. Kaplan, G.-X. Shi, D. A. Andres, M. Meyerson, Oncogenic RIT1 mutations in lung adenocarcinoma. *Oncogene*. **33**, 4418–4423 (2014).

18. P. Rodriguez-Viciana, C. Sabatier, F. McCormick, Signaling specificity by Ras family GTPases is determined by the full spectrum of effectors they regulate. *Mol Cell Biol*. **24**, 4943–4954 (2004).

19. M. Drosten, A. Dhawahir, E. Y. M. Sum, J. Urosevic, C. G. Lechuga, L. M. Esteban, E. Castellano, C. Guerra, E. Santos, M. Barbacid, Genetic analysis of Ras signalling pathways in cell proliferation, migration and survival. *EMBO J*. **29**, 1091–1104 (2010).

20. A. Cuevas-Navarro, R. Van, A. Cheng, A. Urisman, P. Castel, F. McCormick, The RAS GTPase RIT1 compromises mitotic fidelity through spindle assembly checkpoint suppression. *Curr Biol*. **31**, 3915-3924.e9 (2021).

21. L. Sun, S. Xi, Z. Zhou, F. Zhang, P. Hu, Y. Cui, S. Wu, Y. Wang, S. Wu, Y. Wang, Y. Du, J. Zheng, H. Yang, M. Chen, Q. Yan, D. Yu, C. Shi, Y. Zhang, D. Xie, X.-Y. Guan, Y. Li, Elevated expression of RIT1 hyperactivates RAS/MAPK signal and sensitizes hepatocellular carcinoma to combined treatment with sorafenib and AKT inhibitor. *Oncogene*. **41**, 732–744 (2022).

22. A. E. Roberts, J. E. Allanson, M. Tartaglia, B. D. Gelb, Noonan syndrome. *Lancet*. **381**, 333–342 (2013).

23. F. Uhlitz, A. Sieber, E. Wyler, R. Fritsche-Guenther, J. Meisig, M. Landthaler, B. Klinger, N. Blüthgen, An immediate-late gene expression module decodes ERK signal duration. *Mol Syst Biol*. **13**, 928 (2017).

24. S. Takahara, S.-I. Inoue, S. Miyagawa-Tomita, K. Matsuura, Y. Nakashima, T. Niihori, Y. Matsubara, Y. Saiki, Y. Aoki, New Noonan syndrome model mice with RIT1 mutation exhibit cardiac hypertrophy and susceptibility to β-adrenergic stimulation-induced cardiac fibrosis. *EBioMedicine*. **42**, 43–53 (2019).

25. F. Sedaghat-Hamedani, E. Kayvanpour, O. F. Tugrul, A. Lai, A. Amr, J. Haas, T. Proctor, P. Ehlermann, K. Jensen, H. A. Katus, B. Meder, Clinical outcomes associated with sarcomere mutations in hypertrophic cardiomyopathy: a meta-analysis on 7675 individuals. *Clin Res Cardiol*. **107**, 30–41 (2018).

26. A. J. Marian, E. Braunwald, Hypertrophic Cardiomyopathy: Genetics, Pathogenesis, Clinical Manifestations, Diagnosis, and Therapy. *Circ Res*. **121**, 749–770 (2017).

27. C. H. Lee, N. G. Della, C. E. Chew, D. J. Zack, Rin, a neuron-specific and calmodulin-binding small G-protein, and Rit define a novel subfamily of ras proteins. *J Neurosci*. **16**, 6784–6794 (1996).

28. Z. Fang, C. B. Marshall, J. C. Yin, M. T. Mazhab-Jafari, G. M. C. Gasmi-Seabrook, M. J. Smith, T. Nishikawa, Y. Xu, B. G. Neel, M. Ikura, Biochemical Classification of Disease-associated Mutants of RAS-like Protein Expressed in Many Tissues (RIT1). *J Biol Chem*. **291**, 15641–15652 (2016).

29. A. Cuevas-Navarro, L. Rodriguez-Muñoz, J. Grego-Bessa, A. Cheng, K. A. Rauen, A. Urisman, F. McCormick, G. Jimenez, P. Castel, Cross-species analysis of LZTR1 loss-of-function mutants demonstrates dependency to RIT1 orthologs. *Elife*. **11**, e76495 (2022).

30. Y. Aoki, T. Niihori, S. Inoue, Y. Matsubara, Recent advances in RASopathies. *J Hum Genet*. **61**, 33–39 (2016).

31. P. Castel, K. A. Rauen, F. McCormick, The duality of human oncoproteins: drivers of cancer and congenital disorders. *Nat Rev Cancer*. **20**, 383–397 (2020).

32. G. Andelfinger, C. Marquis, M.-J. Raboisson, Y. Théoret, S. Waldmüller, G. Wiegand, B. D. Gelb, M. Zenker, M.-A. Delrue, M. Hofbeck, Hypertrophic Cardiomyopathy in Noonan Syndrome Treated by MEK-Inhibition. *J Am Coll Cardiol*. **73**, 2237–2239 (2019).

33. J. R. Infante, L. A. Fecher, G. S. Falchook, S. Nallapareddy, M. S. Gordon, C. Becerra, D. J. DeMarini, D. S. Cox, Y. Xu, S. R. Morris, V. G. R. Peddareddigari, N. T. Le, L. Hart, J. C. Bendell, G. Eckhardt, R. Kurzrock, K. Flaherty, H. A. Burris, W. A. Messersmith, Safety, pharmacokinetic, pharmacodynamic, and efficacy data for the oral MEK inhibitor trametinib: a phase 1 dose-escalation trial. *Lancet Oncol*. **13**, 773–781 (2012).

34. K. T. Flaherty, C. Robert, P. Hersey, P. Nathan, C. Garbe, M. Milhem, L. V. Demidov, J. C. Hassel, P. Rutkowski, P. Mohr, R. Dummer, U. Trefzer, J. M. G. Larkin, J. Utikal, B. Dreno, M. Nyakas, M. R. Middleton, J. C. Becker, M. Casey, L. J. Sherman, F. S. Wu, D. Ouellet,

A.-M. Martin, K. Patel, D. Schadendorf, METRIC Study Group, Improved survival with MEK inhibition in BRAF-mutated melanoma. *N Engl J Med*. **367**, 107–114 (2012).

35. A. Vichas, A. K. Riley, N. T. Nkinsi, S. Kamlapurkar, P. C. R. Parrish, A. Lo, F. Duke, J. Chen, I. Fung, J. Watson, M. Rees, A. M. Gabel, J. D. Thomas, R. K. Bradley, J. K. Lee, E. M. Hatch, M. K. Baine, N. Rekhtman, M. Ladanyi, F. Piccioni, A. H. Berger, Integrative oncogene-dependency mapping identifies RIT1 vulnerabilities and synergies in lung cancer. *Nat Commun*. **12**, 4789 (2021).

36. L. C. Young, N. Hartig, I. Boned Del Río, S. Sari, B. Ringham-Terry, J. R. Wainwright, G. G. Jones, F. McCormick, P. Rodriguez-Viciana, SHOC2-MRAS-PP1 complex positively regulates RAF activity and contributes to Noonan syndrome pathogenesis. *Proc Natl Acad Sci U S A*. **115**, E10576–E10585 (2018).

37. U. Meyer Zum Büschenfelde, L. I. Brandenstein, L. von Elsner, K. Flato, T. Holling, M. Zenker, G. Rosenberger, K. Kutsche, RIT1 controls actin dynamics via complex formation with RAC1/CDC42 and PAK1. *PLoS Genet*. **14**, e1007370 (2018).

38. S. Dharmaiah, T. H. Tran, S. Messing, C. Agamasu, W. K. Gillette, W. Yan, T. Waybright, P. Alexander, D. Esposito, D. V. Nissley, F. McCormick, A. G. Stephen, D. K. Simanshu, Structures of N-terminally processed KRAS provide insight into the role of N-acetylation. *Sci Rep*. **9**, 10512 (2019).

39. T. Taylor, J.-P. Denson, D. Esposito, Optimizing Expression and Solubility of Proteins in E. coli Using Modified Media and Induction Parameters. *Methods Mol Biol*. **1586**, 65–82 (2017).

40. F. W. Studier, Protein production by auto-induction in high density shaking cultures. *Protein Expr Purif*. **41**, 207–234 (2005).

41. C. Agamasu, R. Ghirlando, T. Taylor, S. Messing, T. H. Tran, L. Bindu, M. Tonelli, D. V. Nissley, F. McCormick, A. G. Stephen, KRAS Prenylation Is Required for Bivalent Binding with Calmodulin in a Nucleotide-Independent Manner. *Biophys J*. **116**, 1049–1063 (2019).

42. K. Kopra, E. Vuorinen, M. Abreu-Blanco, Q. Wang, V. Eskonen, W. Gillette, A. T. Pulliainen, M. Holderfield, H. Härmä, Homogeneous Dual-Parametric-Coupled Assay for Simultaneous Nucleotide Exchange and KRAS/RAF-RBD Interaction Monitoring. *Anal Chem*. **92**, 4971–4979 (2020).

43. T. Travers, C. A. López, C. Agamasu, J. J. Hettige, S. Messing, A. E. García, A. G. Stephen, S. Gnanakaran, Anionic Lipids Impact RAS-Binding Site Accessibility and Membrane Binding Affinity of CRAF RBD-CRD. *Biophys J*. **119**, 525–538 (2020).

44. F. Delaglio, S. Grzesiek, G. W. Vuister, G. Zhu, J. Pfeifer, A. Bax, NMRPipe: a multidimensional spectral processing system based on UNIX pipes. *J Biomol NMR*. **6**, 277–293 (1995).

45. W. Lee, M. Tonelli, J. L. Markley, NMRFAM-SPARKY: enhanced software for biomolecular NMR spectroscopy. *Bioinformatics*. **31**, 1325–1327 (2015).

46. D. W. Morgens, M. Wainberg, E. A. Boyle, O. Ursu, C. L. Araya, C. K. Tsui, M. S. Haney, G. T. Hess, K. Han, E. E. Jeng, A. Li, M. P. Snyder, W. J. Greenleaf, A. Kundaje, M. C. Bassik, Genome-scale measurement of off-target activity using Cas9 toxicity in high-throughput screens. *Nat Commun*. **8**, 15178 (2017).

47. K. L. Schreiber, L. Paquet, B. G. Allen, H. Rindt, Protein kinase C isoform expression and activity in the mouse heart. *Am J Physiol Heart Circ Physiol*. **281**, H2062-2071 (2001).

48. J. Schindelin, I. Arganda-Carreras, E. Frise, V. Kaynig, M. Longair, T. Pietzsch, S. Preibisch, C. Rueden, S. Saalfeld, B. Schmid, J.-Y. Tinevez, D. J. White, V. Hartenstein, K. Eliceiri, P. Tomancak, A. Cardona, Fiji: an open-source platform for biological-image analysis. *Nat Methods*. **9**, 676–682 (2012).

Publishing Agreement

It is the policy of the University to encourage open access and broad distribution of all theses, dissertations, and manuscripts. The Graduate Division will facilitate the distribution of UCSF theses, dissertations, and manuscripts to the UCSF Library for open access and distribution. UCSF will make such theses, dissertations, and manuscripts accessible to the public and will take reasonable steps to preserve these works in perpetuity.

I hereby grant the non-exclusive, perpetual right to The Regents of the University of California to reproduce, publicly display, distribute, preserve, and publish copies of my thesis, dissertation, or manuscript in any form or media, now existing or later derived, including access online for teaching, research, and public service purposes.

DocuSigned by:
Antonio Cuevas Navarro
1E254CAB859F4CA...
Author Signature

8/16/2022
Date